

ทอพอโลยีขนาดเล็กของการปั่นป่วนในลมสุริยะและการขนส่งอนุภาคพลังงานสูง



นายไพศาล ตู่ประกาย

สถาบันวิทยบริการ

วิทยานิพนธ์นี้เป็นส่วนหนึ่งของการศึกษาตามหลักสูตรปริญญาวิทยาศาสตรดุษฎีบัณฑิต

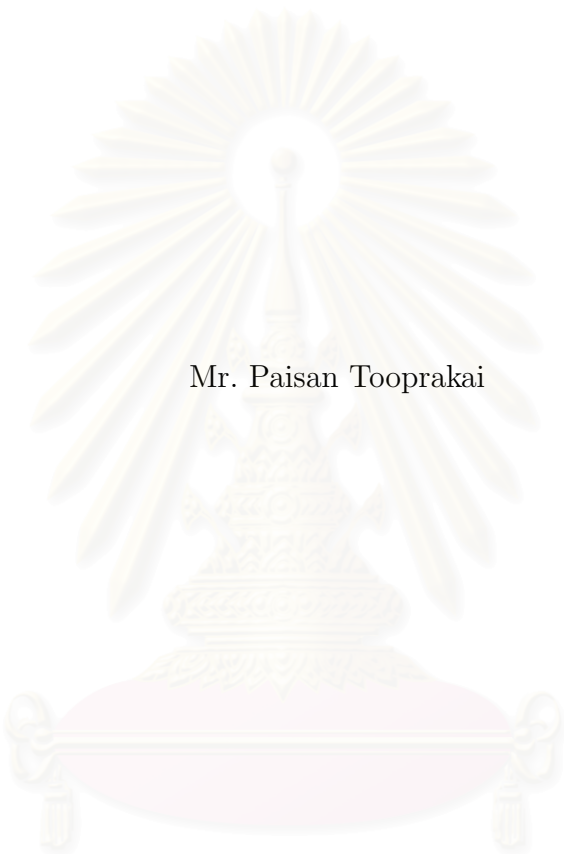
สาขาวิชาฟิสิกส์ ภาควิชาฟิสิกส์

คณะวิทยาศาสตร์ จุฬาลงกรณ์มหาวิทยาลัย

ปีการศึกษา 2550

ลิขสิทธิ์ของจุฬาลงกรณ์มหาวิทยาลัย

SMALL SCALE TOPOLOGY OF SOLAR WIND TURBULENCE
AND ENERGETIC PARTICLE TRANSPORT



Mr. Paisan Tooprakai

A Dissertation Submitted in Partial Fulfillment of the Requirements
for the Degree of Doctor of Philosophy Program in Physics

Department of Physics

Faculty of Science

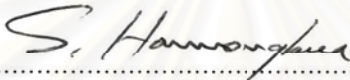
Chulalongkorn University

Academic Year 2007

Copyright of Chulalongkorn University

Thesis Title SMALL SCALE TOPOLOGY OF SOLAR WIND
TURBULENCE AND ENERGETIC PARTICLE
TRANSPORT
By Mr. Paisan Tooprakai
Field of Study Physics
Thesis Advisor Associate Professor Udomsilp Pinsook, Ph. D.
Thesis Co-advisor Professor David Ruffolo, Ph. D.
Professor William H. Matthaeus, Ph. D.


Accepted by the Faculty of Science, Chulalongkorn University in Partial
Fulfillment of the Requirements for the Doctoral Degree



.....Dean of the Faculty of Science
(Professor Supot Hannongbua, Ph.D.)

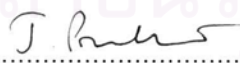
THESIS COMMITTEE

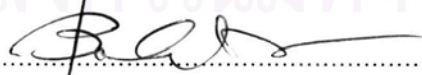

.....Chairman
(Ahpisit Ungkitchanukit, Ph.D.)


.....Thesis Advisor
(Associate Professor Udomsilp Pinsook, Ph.D.)


.....Thesis Co-advisor
(Professor David Ruffolo, Ph.D.)


.....Thesis Co-advisor
(Professor William H. Matthaeus, Ph.D.)


.....Member
(Professor Julian Poulter, Ph.D.)


.....Member
(Assistant Professor Boonchoat Paosawatyanong , Ph.D.)


.....Member
(Assistant Professor Sojiphong Chatraphorn, Ph.D.)

นายไพศาล ตู้ประกาย : ทอพอโลยีขนาดเล็กของการปั่นป่วนในลมสุริยะและการขนส่งอนุภาคพลังงานสูง. (SMALL SCALE TOPOLOGY OF SOLAR WIND TURBULENCE AND ENERGETIC PARTICLE TRANSPORT) **อ. ที่ปรึกษา :** รศ. ดร. อุดมศิลป์ ปิ่นสุข, **อ. ที่ปรึกษาร่วม :** ศ. ดร. เดวิด รูฟโฟโล, Prof. William H. Matthaeus, 105 หน้า.

การสังเกตของอนุภาคพลังงานสูงจากดวงอาทิตย์จากเหตุการณ์การปะทุอย่างรวดเร็ว โดยพบ dropouts (นั่นคือความไม่สม่ำเสมอ และความคมชัดของเกรเดียนต์ของความหนาแน่นของอนุภาค) แสดงถึงการเชื่อมต่อของเส้นสนามบางส่วนจากบริเวณเล็กๆ ของโคโรนาของดวงอาทิตย์ถึงวงโคจรของโลก ทำให้สามารถเข้าใจการกักตัวของเส้นสนาม เนื่องจากโครงสร้างทอพอโลยีขนาดเล็กในลมสุริยะ เราได้ศึกษาต่อมาว่าการสังเกตอนุภาค จะบ่งบอกโครงสร้างของการปั่นป่วนได้อย่างไร โดยวิธีทดลองเชิงตัวเลขใช้กับสนามแม่เหล็กปั่นป่วนที่มี 2 องค์ประกอบ (2D+slab) เราหาเส้นทางของอนุภาคโดยใช้สมการนิวตัน-ลอเรนซ์ และเราดัดแปลงแบบจำลอง 2 องค์ประกอบเป็นสนามเกาส์เซียนแบบ 2 มิติ ในเรขาคณิตพิกัดฉาก และสนามปั่นป่วนแบบ 2 มิติ ในเรขาคณิตทรงกลม ซึ่งรวมถึงกระบวนการโพกัสของอนุภาค สนามปั่นป่วนแบบ 2 มิติถูกสร้างขึ้นโดยผลการแปลงฟูเรียร์แบบเร็ว ซึ่งเป็นการประมาณค่าที่เหมาะสมในช่วงมุมเล็กๆ อนุภาคที่มีประจุสามารถถูกกักในท่อฟลักซ์ชั่วขณะหนึ่ง แล้วหนีออกมาได้ด้วยการรบกวนของการปั่นป่วนแบบสุ่มในสนามแม่เหล็ก ผลลัพธ์โดยรวมทำให้อนุภาคเริ่มการขนส่งแบบ asymptotic ได้ช้า สำหรับสนามปั่นป่วนแบบ 2 มิติ ที่ระยะ 1 AU ผลการจำลองของเราสำหรับการอินทิเกรตต่อเวลาของความหนาแน่นของอนุภาค สำหรับพลังงานต่างๆ มีลักษณะใกล้เคียงกับความหนาแน่นของเส้นสนามแม่เหล็ก นั่นหมายความว่า อนุภาคที่มีพลังงาน < 1 GeV จะเคลื่อนที่ตามเส้นสนามอย่างใกล้ชิด ดังนั้นรูปแบบ dropouts สามารถจำลองโดยการตามเส้นสนาม (ในพิกัดทรงกลม) ซึ่งให้ผลดีเหมือนการตามเส้นทางของอนุภาค

ภาควิชา ฟิสิกส์
สาขาวิชา ฟิสิกส์
ปีการศึกษา 2550

ลายมือชื่อนิสิต..... *Amh Pk*
ลายมือชื่ออาจารย์ที่ปรึกษา..... *U. Pinosok*
ลายมือชื่ออาจารย์ที่ปรึกษาร่วม..... *David P. Pinto*
ลายมือชื่ออาจารย์ที่ปรึกษาร่วม..... *W. H. Matthaeus*

4673821623 : MAJOR PHYSICS

KEY WORD: TURBULENCE / MAGNETIC FIELD

PAISAN TOOPRAKAI: SMALL SCALE TOPOLOGY OF SOLAR WIND
TURBULENCE AND ENERGETIC PARTICLE TRANSPORT. THE-
SIS ADVISOR: ASSOC. PROF. UDOMSILP PINSOOK, Ph.D., THESIS
COADVISOR: PROF. DAVID RUFFOLO, Ph.D., PROF. WILLIAM H.
MATTHAEUS, Ph.D., 105 pp.

The observed dropouts of solar energetic particles from impulsive solar events (i.e., the inhomogeneity and sharp gradients in particle density) indicate the partial filamentation of magnetic connection from small regions of the solar corona to Earth orbit. This can be understood in terms of trapping of field lines due to small-scale topological structures in the solar wind. We further explore how this turbulence structure should be manifest in particle observations. Using a set of numerical experiments using the two-component (2D+slab) description of magnetic turbulence, we evaluate particle trajectories using the fundamental Newton-Lorentz equations. We adapt the two-component model to a 2D Gaussian field in Cartesian geometry, and a 2D turbulent field in spherical geometry, which includes the focusing of particles. The 2D turbulent field is generated by a 2D fast Fourier transform, a valid approximation over a small angular region. The charged particles can be temporarily trapped in flux tubes and then escape due to random turbulent perturbations in the magnetic field. The overall effect is a delay in the onset of time-asymptotic transport. For the 2D turbulent field, at 1 AU our simulations of particle density integrated over time for various energies match quite closely with the magnetic field line density. That means the particles of energy < 1 GeV follow the field lines very closely, so “dropout” patterns can be modeled by field line tracing (in spherical geometry) as well as particle tracing.

Department: Physics

Field of study: Physics

Academic year: 2007

Student's signature: *Paisan Tooprakai*

Advisor's signature: *U. Pinsook*

Co-advisor's signature: *David Ruffolo*

Co-advisor's signature: *William H. Matthaeus*

Acknowledgements

I would like to express my deeply felt gratitude to numerous people who have, directly and indirectly, contributed to this work. I am thankful to all of them for their encouragement and support, especially my co-advisors, Professor Dr. David Ruffolo and Professor Dr. William H. Matthaeus, for supervision and encouragement during my thesis and my programming work for my graduate study. Without their guidance, I could not finish this work. I am also grateful to Associate Professor Dr. Udomsilp Pinsook, my advisor, for kind suggestions.

I would like to thank the Thailand Research Fund very much for providing financial support through the Royal Golden Jubilee Fellowship for the Ph.D. program.

Another person whom I would like to thank is Miss Piyanate Chuychai, for helpful suggestions about programming in Fortran 77 and teaching me to run MPI codes for parallel programming on clusters of computers. I would also like to thank Miss Achara Seripienlert for helping to run programs and Dr. Pablo Dmitruk for teaching me to run parallel programs on a grid of computers.

Finally, I would like to thank my family that always supports and takes care of me.

สถาบันวิทยบริการ
จุฬาลงกรณ์มหาวิทยาลัย

Contents

	page
Abstract (Thai)	iv
Abstract (English)	v
Acknowledgements	vi
Contents	vii
List of Figures	ix
List of Tables	xv
Chapter I Introduction	1
1.1 Motivation	1
1.2 Objectives	4
Chapter II Background and Literature Review	5
2.1 Introduction to Turbulence	5
2.2 Kolmogorov Theory	6
2.3 Power Spectrum	8
2.4 Solar Wind and Interplanetary Magnetic Field	11
2.5 2D + Slab Model of Magnetic Turbulence	12
2.6 Dropout Phenomena from Observations	16
2.7 Suppression of Diffusive Escape by a Strong 2D Field	22
Chapter III Numerical Methods in Cartesian Geometry	26
3.1 Tracing Magnetic Field Lines in Cartesian Geometry	26
3.2 Tracing Particle Motion in Cartesian Coordinates	31
Chapter IV Results of Simulations of Particle Transport in Cartesian Geometry	33

Chapter V	Numerical Methods in Spherical Geometry	46
5.1	Equations of Motion in Spherical Coordinates	47
5.2	Generating 2D + Slab Magnetic Fields in Spherical Geometry	54
5.3	Tracing Magnetic Field Lines in Spherical Geometry	56
5.4	Summary of Our Simulations	59
Chapter VI	Results of Simulations of Turbulent Magnetic Fields and Particle Transport in Spherical Geometry	61
Chapter VII	Discussion and Conclusions	83
References		86
Appendices		89
Appendix A	Normalization of the Equation of Motion	90
A.1	Normalization by the Alfvén Speed	91
A.2	Normalization by the Speed of Light	92
Appendix B	Solving Equations of Motion in Spherical Coordinates	94
Appendix C	Gaussian Magnetic Flux Tube in Cartesian Geometry	99
Appendix D	Pathlength of a Helical Trajectory	102
Vitae		105

List of Figures

Figure		Page
Figure 2.1	Conservation of volume of an eddy with random motions.	7
Figure 2.2	Kolmogorov theory.	8
Figure 2.3	Schematic spectrum of turbulence from Kolmogorov theory. ..	10
Figure 2.4	Solar wind and interplanetary magnetic field lines from the Sun. (Image credit: Chuychai (2004))	11
Figure 2.5	Magnetic field lines for slab fluctuations, which depend only on z	14
Figure 2.6	The contour plot of a potential function $a(x, y)$ for two-dimensional turbulence.	15
Figure 2.7	Dropouts in impulsive flare events of 1999 January 9-10 observed by Mazur et al. (2000). (a) Kinetic energy per mass of H-Fe ions in units of MeV nucleon ⁻¹ vs. arrival time at 1 AU. (b) H-Fe counts vs. time in ≈ 14 minute bins. The vertical lines show event subin- tervals. (c) Interplanetary magnetic field angle in the geocentric solar ecliptic (GSE) x - y plane. (d) Interplanetary magnetic field angle from the GSE x - y plane. (Image credit: Mazur et al. (2000))	17
Figure 2.8	Data from a gradual event, with no apparent dropout features. (a) Energy of oxygen ions (in units of MeV nucleon ⁻¹) vs. arrival time at 1 AU for the solar particle event of 1999 June 4. (b) Oxygen counts vs. time in 5 minute bins. (c) Interplanetary magnetic angle in the GSE x - y plane. (d) Interplanetary magnetic field angle from the GSE x - y plane. (Image credit: Mazur et al. (2000))	18

Figure 2.9	Scatter plot of the locations of magnetic field lines that are initially (at $z = 0$) located within a circle (simulating the region where particles are injected as a result of an impulsive solar flare). Parameter values are chosen to be appropriate for the solar wind. (Image credit: Ruffolo et al. (2003))	20
Figure 2.10	Illustration of interplanetary magnetic field lines populated with SEPs from a localized source region near the Sun, as expected for an impulsive solar flare. In the two-dimensional + slab model of solar wind turbulence, some field lines are trapped in filaments corresponding to the small-scale topology, i.e. islands of the two-dimensional turbulence, out to Earth orbit. (Image credit: Ruffolo et al. (2003))	21
Figure 2.11	Magnetic field line trajectories in a representation of 2D + slab turbulence starting near an O-point (red) and X-point (blue). The surface plot at the bottom shows the potential function $a(x, y)$ corresponding to the 2D turbulence. (Image credit: Chuychai et al. (2007))	25
Figure 3.1	Example of the trajectory of two magnetic field lines in the pure slab magnetic fluctuation plus mean field.	28
Figure 3.2	Example of the trajectory of a field line in a pure 2D magnetic fluctuation plus mean field.	29
Figure 3.3	Example of two trajectories in slab plus 2D fluctuations plus the mean magnetic field.	30
Figure 4.1	Illustration of 50 magnetic field lines (red) and the trajectories of 50 particles (blue) with the same initial positions that start at $z = 0, r = 0.1l_{\parallel}$ in a mean field + Gaussian 2D field + slab turbulence. Here the parameters of the 2D field are the same as in the	

- high B case and all particles have low E . In the main plot, while trapped, the field lines map out regular flux surfaces of the Gaussian flux tube until their escape. Note that some particles undergo resonant pitch angle scattering and move downward to $z < 0$. In the lower inset, individual guiding center motion is evident. In the inset showing the most magnified view, the gyration of individual particles is seen. 35
- Figure 4.2 Illustration of low energy particle transport with varying magnetic fields. Upper panel: Mean squared perpendicular displacement $\langle \Delta r^2 \rangle$ vs. time t for various cases. Lower panel: Running perpendicular diffusion coefficient $\kappa = \langle \Delta r^2 \rangle / (4t)$ vs. time t for various cases. 36
- Figure 4.3 Like Figure 4.2, for medium energy particles. 37
- Figure 4.4 Like Figure 4.2, for high energy particles 38
- Figure 4.5 Upper panel: Mean squared perpendicular displacement $\langle \Delta r^2 \rangle$ vs. time t for medium energy particles for a strong 2D flux tube or pure slab turbulence. Lower panel: Running perpendicular diffusion coefficient $\kappa = \langle \Delta r^2 \rangle / (4t)$ vs. time t for various cases. There is more trapping for lower energy particles and for stronger 2D flux tubes. 40
- Figure 4.6 Example of high energy particle transport with slab and high magnetic fields to show $f_g(t + t_{trap})$ and $f_s(t)$ 43
- Figure 4.7 Example of how a 2D flux tube (the high B case) confines particles and leads to steep spatial gradients for an extended time (black histogram), in comparison with a case with no flux tube (pure slab; gray histogram). Distances are in units of $l_{||}$, and r is the distance

	from the axis of the flux tube, which has a Gaussian potential function with $\sigma = 0.5l_{\parallel}$. Histograms show counts per $0.05l_{\parallel}$ bin. The 5000 particles were started at $t = 0$ from random locations within $r = 0.1l_{\parallel}$ from the flux tube axis, and the histograms and scatter plots (insets) indicate their locations at $t = 1000l_{\parallel}/c$. The sharp gradients for the high B case correspond to dropout features in energetic ions and electrons from impulsive solar flares as observed near Earth.	45
Figure 5.1	Upper panel: φ vs. time. Lower panel: λ vs. time. The magnetic field is a radial field. The simulations successfully follow the correct gyro-frequency for a 1 MeV particle.	50
Figure 5.2	Like Figure 5.1, for a 10 MeV particle.	51
Figure 5.3	Like Figure 5.1, for a 100 MeV particle.	52
Figure 5.4	Like Figure 5.1, for a 1 GeV particle.	53
Figure 5.5	Example of the trajectory of a magnetic field line in spherical coordinates.	57
Figure 5.6	Example of the trajectory of the same magnetic field line as in Figure 5.5, transformed to Cartesian coordinates in units of AU.	58
Figure 5.7	Diagram of steps in the field line or particle simulations.	60
Figure 6.1	Contour plot of potential function $a(\varphi, \lambda)$. The dark color represents of the minimum a and light color represents the maximum a	66
Figure 6.2	Scatter plots of magnetic field lines at $r = 0.1, 0.15, 0.25, 0.5, 1,$ and 2 AU. Lines are contours of constant $a(\varphi, \lambda)$	67

Figure 6.3	Scatter plots for a particle energy of 1 MeV at $r = 0.1, 0.15, 0.25, 0.5, 1,$ and 2 AU.	68
Figure 6.4	Scatter plots for a particle energy of 10 MeV at $r = 0.1, 0.15, 0.25, 0.5, 1,$ and 2 AU.	69
Figure 6.5	Scatter plots for a particle energy of 100 MeV at $r = 0.1, 0.15, 0.25, 0.5, 1,$ and 2 AU.	70
Figure 6.6	Scatter plots for a particle energy of 1 GeV at $r = 0.1, 0.15, 0.25, 0.5, 1,$ and 2 AU.	71
Figure 6.7	Scatter plots for a particle energy of 10 GeV at $r = 0.1, 0.15, 0.25, 0.5, 1,$ and 2 AU.	72
Figure 6.8	Scatter plots of φ vs. r for a particle energy of 1 MeV at $s = 0.0, 0.15, 0.25, 0.5, 1,$ and 2 AU.	73
Figure 6.9	Scatter plots of φ vs. r for a particle energy of 10 MeV at $s = 0.0, 0.15, 0.25, 0.5, 1,$ and 2 AU.	74
Figure 6.10	Scatter plots of φ vs. r for a particle energy of 100 MeV at $s = 0.0, 0.15, 0.25, 0.5, 1,$ and 2 AU.	75
Figure 6.11	Scatter plots of φ vs. r for a particle energy of 1 GeV at $s = 0.0, 0.15, 0.25, 0.5, 1,$ and 2 AU.	76
Figure 6.12	Scatter plots of φ vs. r for a particle energy of 10 GeV at $s = 0.0, 0.15, 0.25, 0.5, 1,$ and 2 AU.	77
Figure 6.13	Scatter plots of λ vs. r for a particle energy of 1 MeV at $s = 0.0, 0.15, 0.25, 0.5, 1,$ and 2 AU.	78
Figure 6.14	Scatter plots of λ vs. r for a particle energy of 10 MeV at $s = 0.0, 0.15, 0.25, 0.5, 1,$ and 2 AU.	79
Figure 6.15	Scatter plots of λ vs. r for a particle energy of 100 MeV at $s = 0.0, 0.15, 0.25, 0.5, 1,$ and 2 AU.	80

Figure 6.16	Scatter plots of λ vs. r for a particle energy of 1 GeV at $s = 0.0, 0.15, 0.25, 0.5, 1,$ and 2 AU.	81
Figure 6.17	Scatter plots of λ vs. r for a particle energy of 10 GeV at $s = 0.0, 0.15, 0.25, 0.5, 1,$ and 2 AU.	82
Figure D.1	Cylindrical magnetic field. LB = low B , HB = high B	102



สถาบันวิทยบริการ
จุฬาลงกรณ์มหาวิทยาลัย

List of Tables

Table		Page
Table 4.1	Particle parameters for $B_0 = 5$ nT and $l_{\parallel} = 0.02$ AU, and simulated/calculated arrival time of the particles at the first peak (in units of l_{\parallel}/c).	42
Table 4.2	Trapping times.	44
Table 6.1	Particle parameters for $B_1 = 5$ nT and $l_{\parallel} = 0.02$ AU (in units of l_{\parallel}/c) at 1 AU.	66



สถาบันวิทยบริการ
จุฬาลงกรณ์มหาวิทยาลัย

Chapter I

Introduction

1.1 Motivation

Populations of energetic particles observed in the heliosphere are described frequently using transport equations that incorporate diffusion in an essential way. The standard view is that spatial transport of an ensemble of charged particles involves two types of diffusion: parallel diffusion along and perpendicular diffusion across the mean local magnetic field (Jokipii, 1966). To these additional effects such as convection, adiabatic expansion and local acceleration may be added to formulate a complete transport theory (Parker, 1965). This type of transport theory has been successful to the degree that it is tempting to regard the approach as fundamental. There are however problems, especially for perpendicular transport, the most serious of which are observational. As an example, heliospheric energetic particle observations seem to require rapid cross field transport over large expanses of latitude in Ulysses observations (McKibben et al., 2001). On the other hand the persistence of sharp gradients in the observed flux of solar energetic particles, known as dropouts (see Section 2.7), seems to set an upper limit on cross field diffusion that is much lower than what is needed to account for latitudinal transport (Mazur et al., 2000). Evidently, to account for these observed features, one must take in to account factors not ordinarily included in standard diffusive transport theory. These include time dependence of the heliospheric field lines at their base (Fisk, 1996; Giacalone et al., 2000) and topological trapping associated with the turbulent flux tube structure transverse

to the large scale heliospheric magnetic field (Ruffolo et al., 2003; Chuychai et al., 2005, 2007). Here we further explore the second of these ideas, examining whether charged particles as well as magnetic field lines might experience effects associated with the magnetic field topology of the homogeneous turbulence in which their transport is initiated.

The usual sequence of events in transport is that particles (or field lines) initially stream freely, and then begin to be affected by a random force. Once the random force is sampled over its correlation length (or time) the process of random walk, or diffusion, becomes evident. A well known difficulty arises when the magnetic irregularities responsible for diffusion have reduced dimensionality (Jokipii et al., 1993; Jones et al., 1998), so that diffusion might not occur at all, or perhaps it can only be recovered by defining a suitably designed ensemble. A further difficulty in arriving at a time-asymptotic transport limit (diffusive or not) is that certain subsets of particles with special initial or boundary conditions might require different times to relax to the statistical state, meanwhile retaining memory of the initial state. In this way the pre-diffusive epoch of single particle transport (ordinarily associated with free streaming) might persist for widely varying times, for specially prepared subensembles of particles. Therefore, for example, diffusion might be a good approximation when averaged over all energetic particles in the heliosphere, but might not apply to particles from a particular solar flare as observed at Earth orbit.

The basic idea explored here originates in a careful examination of magnetic flux surfaces in so-called two-component turbulence models (see Section 2.5). These are a composite of two ingredients slab: (1D) fluctuations that vary only along the (uniform) mean magnetic field direction, and two-dimensional (2D) fluctuations that vary only in the two perpendicular directions (e.g., Bieber et

al., 1994). The superposition of the two types of fluctuations is fully three dimensional (3D) even though the separate components are of reduced dimensionality. Field line trajectories in large amplitude fluctuations of this type (Matthaeus et al., 1995) are well described by diffusion theory, for displacements greater than a few correlation lengths along the mean field, provided that averages are taken over an unbiased random sampling of field lines. However a closer inspection (Ruffolo et al., 2003) reveals that diffusive transport can be greatly delayed for a subset of field lines that begins in the vicinity of O-type neutral points of the 2D fluctuations. This delay is due to the confining topology of the flux tube along with suppressed diffusive escape where the 2D field is strong (Chuychai et al., 2005). A single 2D flux tube provides a useful model of both contributions to the field line trapping near O-type structures that naturally occur at random locations in 2D turbulence (Chuychai et al., 2007). If particles injected near O-points experience delays similar to those of the field lines, that may explain the dropouts in solar energetic particles.

In this work, we are interested to simulate charged particle motion in 2D + slab magnetic turbulence in both Cartesian and spherical geometries by a Kolmogorov power spectrum to study the dropout phenomenon (Mazur et al., 2000). The key difference is that we use a mean field $\mathbf{B}_0 = B_0 \hat{z}$ in Cartesian geometry and $\mathbf{B}_0 = B_0 \hat{r}$ in spherical geometry. In each case, the turbulent fluctuations are perpendicular to the mean field. The spherical geometry is more realistic than Cartesian geometry since spherical geometry has the focusing effect which makes the particles change their pitch angle with time (see Chapters V and VI). Then, in this thesis, we first explain the basic theory to understand about turbulence, the dropout phenomenon, and a literature review of this work in Chapter II. Then in Chapter III we show our new methods to generate the magnetic field turbulence and trace the magnetic field lines and charged test

particles by solving the relevant differential equations in Cartesian coordinates. Chapter IV presents the results from a Gaussian 2D field in Cartesian geometry to analyze the behavior and characteristics of the charged particles. Then we trace magnetic field lines and particles in spherical geometry and test our code for accuracy by using the gyro-frequency of particles in a radial field as shown in Chapter V. Chapter VI presents results for the particle and magnetic field line trajectories using a Fourier transform random-phase 2D field + slab field. Finally, we summarize our results in Chapter VII and discuss the charged particle motion in comparison with dropout phenomena.

1.2 Objectives

The objectives of this work are:

1. To model the motion of energetic charged particles motion as a function of energy in turbulent magnetic fields.
2. To study the characteristics of the particle motion in the magnetic field turbulence to explain the observed phenomenon of dropouts.

สถาบันวิทยบริการ
จุฬาลงกรณ์มหาวิทยาลัย

Chapter II

Background and Literature Review

2.1 Introduction to Turbulence

Turbulence is a type of flow that can occur in any fluid, involving swirling motions over a wide range of length scales. In general it involves irregular and instantaneous motions of fluids with many scales of eddies in the fluid flow. We can see turbulence everywhere, such as in smoke from cigarettes, a bullet moving through air, feeding fish in a pond, water falling in a basin, etc. The conditions for the occurrence of turbulence are (H. Tennekes and J. L. Lumley, 1994):

2.1.1 Irregularity. Turbulence is initiated by random perturbations and instabilities. It is difficult to describe the instantaneous turbulent motion by mathematical functions. Instead, the motion can be described statistically.

2.1.2 Three-dimensional vorticity fluctuations. Turbulence is rotational in three dimensions.

2.1.3 Diffusivity. The diffusivity of turbulence, which causes rapid mixing and increased rates of momentum, heat, and mass transfer, is another important feature of all turbulent flows.

2.1.4 High Reynolds number. In fluid mechanics, the Reynolds number is the ratio of inertial forces to viscous forces and these two types of forces determine the flow conditions. The Reynolds number can be used to identify and predict different flow regimes, such as laminar or turbulent flow. Laminar flow occurs at low Reynolds numbers, where viscous forces are dominant, and its flow

is smooth and nearly constant, while turbulent flow occurs at high Reynolds numbers and is dominated by inertial forces, which produce random eddies, vortices and fluctuations. The Reynolds number is defined by

$$\text{Re} = \frac{LU}{\nu} \quad (2.1)$$

where L is the characteristic scale length of the flow, U is the mean velocity of the fluid's flow, and ν is the (kinematic) viscosity. If $\text{Re} \gtrsim 10^3$, there is turbulent flow. If $\text{Re} \lesssim 1$, there is laminar flow. The solar wind has $\text{Re} \approx 10^{12}$ and is therefore highly turbulent.

2.1.5 Energy input and energy dissipation. Turbulence is essentially dissipative, whereas waves are essentially nondissipative. The turbulence has a continuous loss of energy due to viscous losses. If no energy is supplied, the turbulence will decay quickly. With a continuous supply of energy, turbulence can persist.

2.1.6 Continuum. Turbulence is a continuum phenomenon. The scales that we observe should be large enough to see the fluid as continuum.

In our work, we simulated and studied the interplanetary magnetic field turbulence due to the solar wind or solar active events.

2.2 Kolmogorov Theory

Kolmogorov's turbulence model (Kolmogorov, 1941) states that energy flows across scales in what is called a "turbulent cascade." Energy due to large-scale motions can cause instabilities (fluctuations) in the flow at low wavenumber, say, at scale length L_0 , due to the nonlinearity of the Navier-Stokes equation governing the fluid motion. The size of large-scale fluctuations, referred to as the large eddies, can be characterized by their outer scale length L_0 . Here $\text{Re} \gg 1$

and the wavenumber $k_L = 2\pi/L_0$. Energy is transported from large eddies to smaller and smaller eddies due to the conservation of 3D vorticity. Figure 2.1 shows the eddies (vortices) of the fluid in three dimensions, which are roughly cylindrical, called vortex tubes or vortex lines. Each end of the vortex tube can randomly move, which will pull to extend the tube, and then the length of the vortex tube will increase. The volume of the vortex tube is conserved, so the size of the eddies will decrease. That means the size of the eddies transfers from large-scale to small-scale vortex tubes.

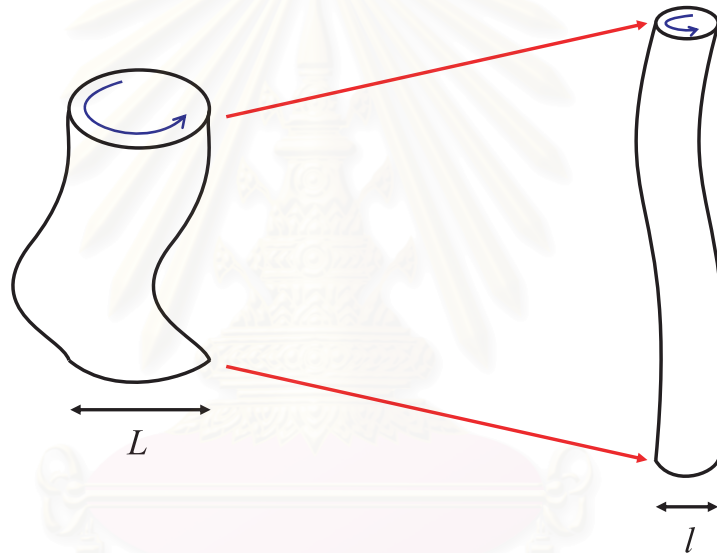


Figure 2.1: Conservation of volume of an eddy with random motions.

This continues until $Re \sim 1$, where the viscosity effect is of the same order as the inertial effect. Near and below this “inner scale,” viscosity is important and the flow kinetic energy is dissipated to heat. The size of these small-scale fluctuations, referred to as small eddies, can be characterized by their inner scale length l_0 and wavenumber $k_l = 2\pi/l_0$ (see Figure 2.2). The fluctuations with sizes between l_0 and L_0 are in the so-called inertial subrange, which has scale-invariant behavior that is independent of the flow geometry. The energy transport rate

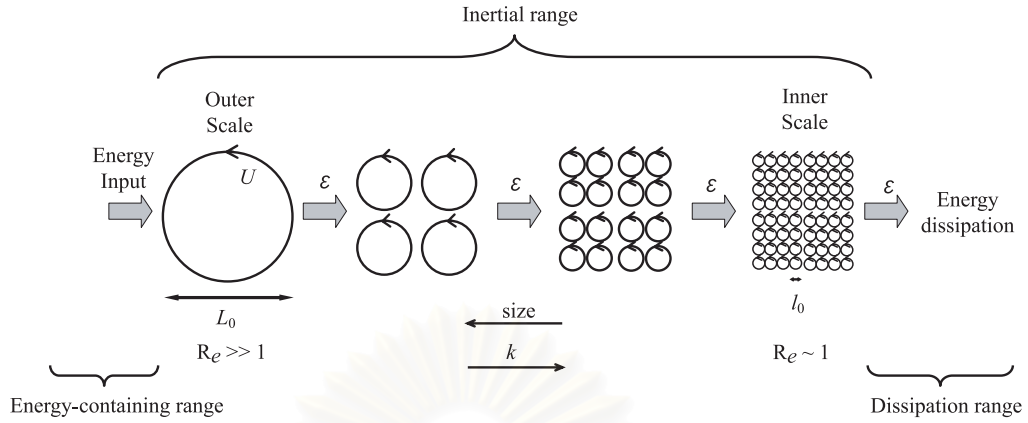


Figure 2.2: Kolmogorov theory.

(or dissipation rate) per unit mass ϵ for eddies of size l (see Figure 2.2) can be defined by

$$\left. \begin{aligned} \frac{\text{energy}}{\text{mass}} &\sim U^2, \\ \text{eddy turnover time} &\sim \frac{l}{U}, \\ \epsilon = \frac{\text{energy}}{\text{mass} \cdot \text{time}} &\sim \frac{U^3}{l}. \end{aligned} \right\} \quad (2.2)$$

The steady state ϵ is independent of l , which implies that

$$\begin{aligned} \frac{U^3}{l} &= \text{constant} \\ \therefore U &\propto l^{1/3}. \end{aligned} \quad (2.3)$$

As l decreases then U decreases also to maintain a constant ϵ in a steady state.

2.3 Power Spectrum

For stochastic processes, the “correlation function” or “two-point correlation” is the correlation between random variables at two different points in space or time. We consider how the fluctuating magnetic fields \mathbf{b} at two different positions are correlated. Then the correlation function is defined by

$$R_{ij}(\mathbf{x}) = \langle b_i(\mathbf{x}_0) b_j(\mathbf{x}_0 + \mathbf{x}) \rangle, \quad (2.4)$$

where $i, j = x, y$, or z and $\langle \rangle$ implies an ensemble average. For homogeneous turbulence, $R_{ij}(\mathbf{x})$ is independent of \mathbf{x}_0 and we can write

$$R_{ij}(\mathbf{x}) = \langle b_i(0)b_j(\mathbf{x}) \rangle. \quad (2.5)$$

The power spectrum is the Fourier transform of the correlation function, defined by

$$P_{ij}(\mathbf{k}) = \frac{1}{(2\pi)^3} \int R_{ij}(\mathbf{r}) e^{-i\mathbf{k}\cdot\mathbf{r}} d\mathbf{r}, \quad (2.6)$$

where \mathbf{k} is the wavevector. The trace $\sum_i P_{ii}$ can be interpreted as the magnetic energy per wavenumber \mathbf{k} .

From the previous section the energy per mass depends on U^2 or $l^{2/3}$ or $k^{-2/3}$, where U and l are the velocity and length scales of eddies and k is the wavenumber. Now consider the spectrum in the inertial range. We can write

$$\frac{dE}{dk} \propto \frac{\Delta E}{\Delta k} \propto \frac{k^{-2/3}}{k} = k^{-5/3} \quad (2.7)$$

where k is magnitude of the wave vector and E is the kinetic energy of the fluid. This is called ‘‘Kolmogorov’s $k^{-5/3}$ law’’ or ‘‘the Kolmogorov spectrum’’ of U . We want to specify the power spectrum of a turbulent field \mathbf{b} in a similar way. The statistical description of the fluctuation \mathbf{b} gives $\langle \mathbf{b} \rangle = 0$, and $\mathbf{B} = \mathbf{B}_0 + \mathbf{b}(x, y, z)$ by definition. The energy density of the magnetic field is

$$\frac{E}{\text{volume}} = \frac{b^2}{8\pi}. \quad (2.8)$$

If the flow field and magnetic field achieve statistical equilibrium (equipartition), then

$$\frac{E}{\text{volume}} \propto b^2 \propto \rho U^2 \propto k^{-2/3}. \quad (2.9)$$

where ρ is the density of the fluid, taken to be approximately constant. Then eq. (2.7) can apply to the magnetic power spectrum as well. For fluctuations in one

dimension, say, z , the power spectrum of the magnetic field goes as

$$P_{xx}(k_z) \propto k_z^{-5/3},$$

for scales between the inner and outer scales shown in Figure 2.2.

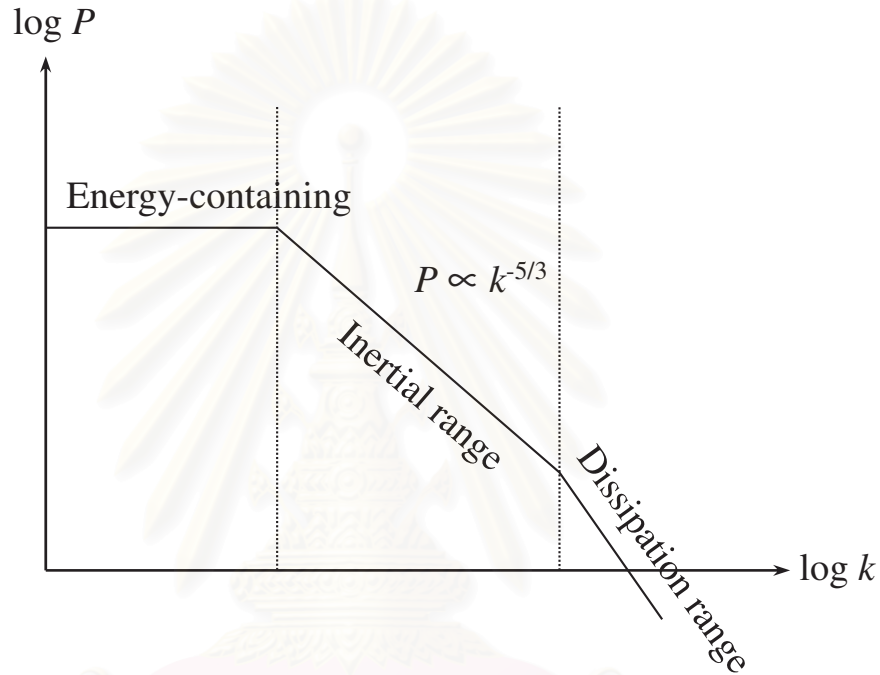


Figure 2.3: Schematic spectrum of turbulence from Kolmogorov theory.

The graph between $\log P$ and $\log k$, shown schematically in Figure 2.3, has three regions. The first is the energy-containing range for low k , and scales larger than the outer scale of turbulence. The second is the inertial range, for scales shown in Figure 2.2, between the inner and outer scales of turbulence. This is where Kolmogorov theory for the turbulent cascade is applicable, and $P \propto k^{-5/3}$. The final region is the dissipation range. Here the power spectrum falls more steeply because the viscosity dominates, making the energy decay rapidly with increasing k .

In this work, for one-dimensional turbulence we use

$$P_{xx}(k_z) = \frac{C}{(1 + k_z^2 l_{\parallel}^2)^{5/6}}, \quad (2.10)$$

where l_{\parallel} is the bendover scale, on the order of the outer scale, and C is the normalization value. Eq.(2.10) models the energy-containing range and the inertial range. Here we use eq.(2.10) since the power spectrum will be a constant value for small k and proportional to $k^{-5/3}$ for large k which is the Kolmogorov spectrum in inertial range.

2.4 Solar Wind and Interplanetary Magnetic Field

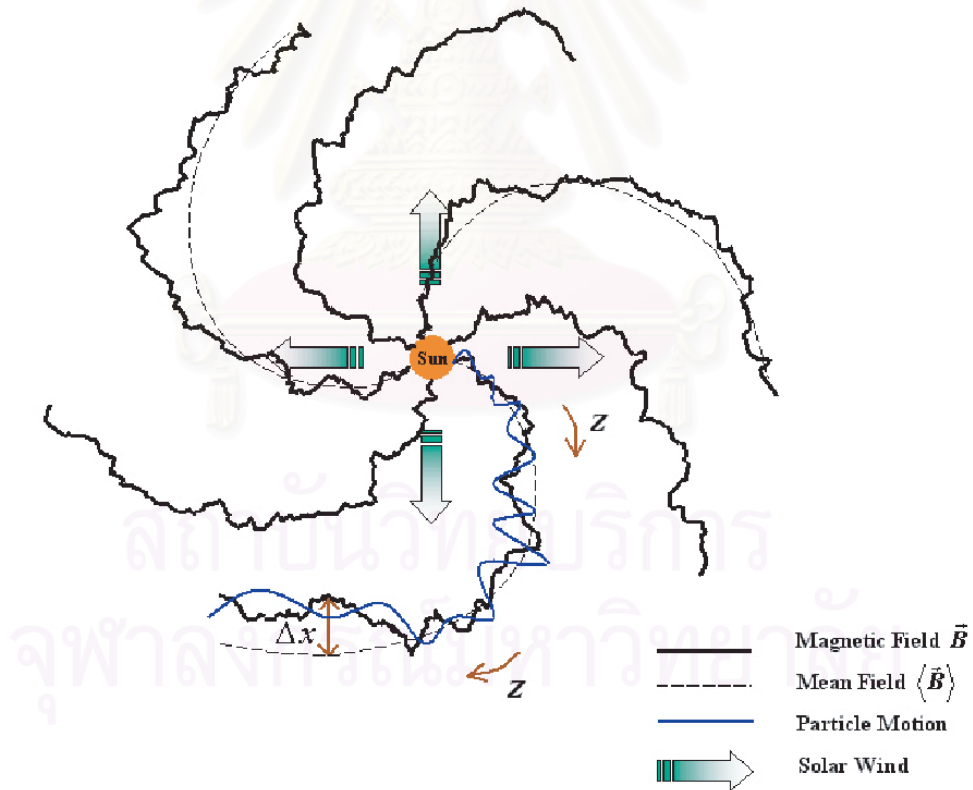


Figure 2.4: Solar wind and interplanetary magnetic field lines from the Sun. (Image credit: Chuychai (2004))

The solar wind comprises plasmas (ionized gases) that continuously flow out from the Sun into interplanetary space in all directions. Figure 2.4 shows the solar wind and interplanetary magnetic field. The interplanetary magnetic field is the solar field that is dragged outward from the Sun with the turbulent solar wind. In Figure 2.4, the dashed lines are the mean magnetic field, which has an Archimedean spiral shape due to the Sun’s rotation, and the solid lines are the turbulent interplanetary magnetic field lines. In addition, the solar wind’s flow is not smooth because the Sun has both slow solar wind and fast wind. There is also solar activity such as solar flare events and ejections of a huge mass from the corona, which we call “coronal mass ejections” or CMEs. Both types of occasional solar activity release solar energetic particles (SEPs). In the figure, the blue line indicates a helical orbit of a particle along the magnetic field.

2.5 2D + Slab Model of Magnetic Turbulence

Matthaeus et al. (1990) review two sets of observations, from the Zeta plasma device and tokamak and the observed anisotropy of an interplanetary fluctuation data set from the ISEE-3 spacecraft. They suggest that the traditional slab model should be modified. They argue that the dynamical evolution of MHD turbulence in the presence of a strong dc magnetic field leads to an anisotropic, quasi-two-dimensional state rather than an isotropic state. Thus this model of the solar wind views it as a fluid that contains both transverse slab-like or Alfvénic fluctuations together with a population of quasi-transverse fluctuations. In their later work (Bieber et al. 1994, Matthaeus et al. 1995), they developed this as a two-component model of magnetic turbulence.

In this model, which we use in the present work, the magnetic field is

$$\mathbf{B}(x, y, z) = \mathbf{B}_0 + \mathbf{b}(x, y, z), \quad (2.11)$$

where \mathbf{B} is the total magnetic field, $\mathbf{B}_0 = B_0 \hat{z}$ is the constant mean magnetic field in the z -direction, and \mathbf{b} is a transverse fluctuation. Then $\mathbf{b}(x, y, z)$ can be separated into two components of transverse fluctuations, slab and two-dimensional magnetic fields:

$$\mathbf{b}(x, y, z) = \mathbf{b}^{\text{slab}}(z) + \mathbf{b}^{2\text{D}}(x, y). \quad (2.12)$$

For the slab magnetic turbulence,

$$\mathbf{b}^{\text{slab}}(z) = b_x^{\text{slab}}(z) \hat{x} + b_y^{\text{slab}}(z) \hat{y}, \quad (2.13)$$

where b_x^{slab} and b_y^{slab} are fluctuating magnetic fields that depend only on z , the coordinate along the mean field (see Figure 2.5). Note that \mathbf{b}^{slab} is perpendicular to \hat{z} .

For the 2D magnetic turbulence,

$$\mathbf{b}^{2\text{D}} = b_x^{2\text{D}}(x, y) \hat{x} + b_y^{2\text{D}}(x, y) \hat{y}, \quad (2.14)$$

where $b_x^{2\text{D}}$ and $b_y^{2\text{D}}$ depend on x and y and we can write

$$\mathbf{b}^{2\text{D}}(x, y) = \nabla \times [a(x, y) \hat{z}], \quad (2.15)$$

where $a\hat{z}$ is the vector potential for the two-dimensional component of turbulence and $a(x, y)$ can be called the “potential function” as shown in Figure 2.6.

Figure 2.6 shows the contour plot of a potential function, $a(x, y)$. The circles in the figure indicate O-points, which are local maxima or minima in $a(x, y)$, where the field lines (or the particles) can be trapped within small-scale topological islands of the 2D turbulence. X-points are outside islands. X-points are defined as saddle points of $a(x, y)$ (there is no 2D field here), and this area is dominated by the slab field.

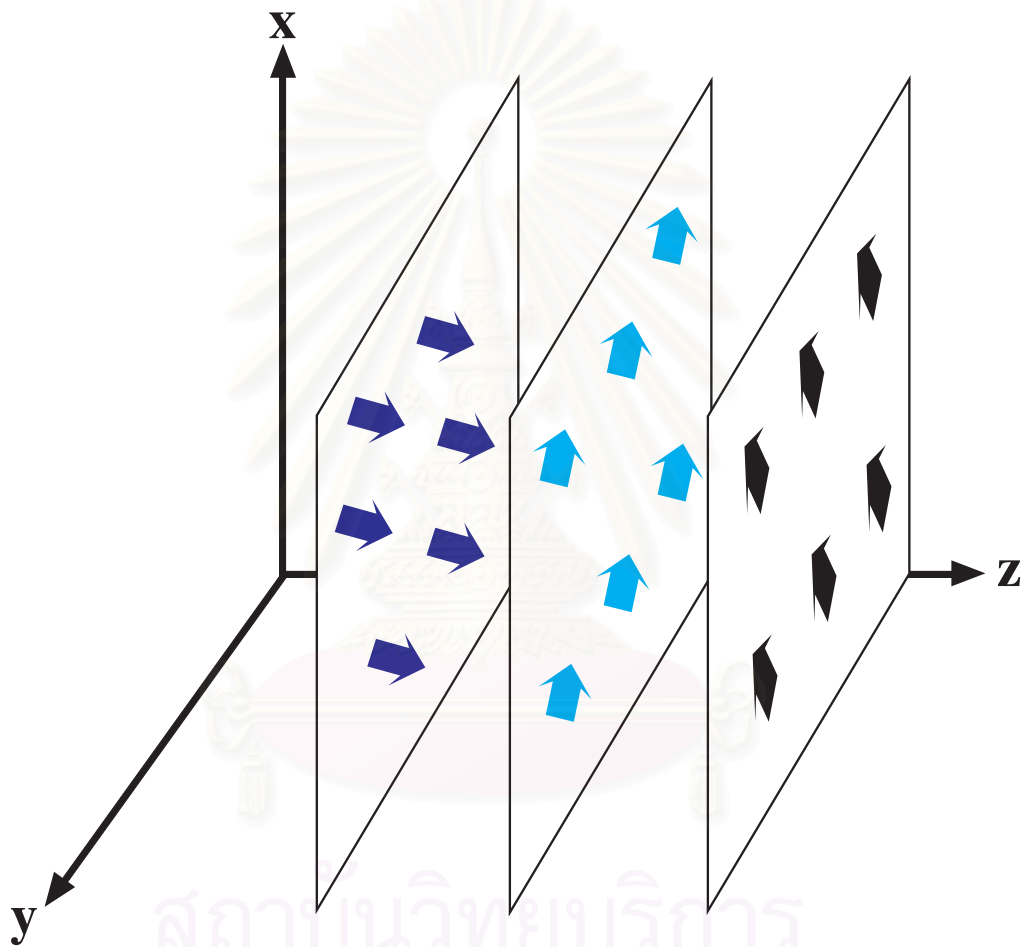


Figure 2.5: Magnetic field lines for slab fluctuations, which depend only on z .

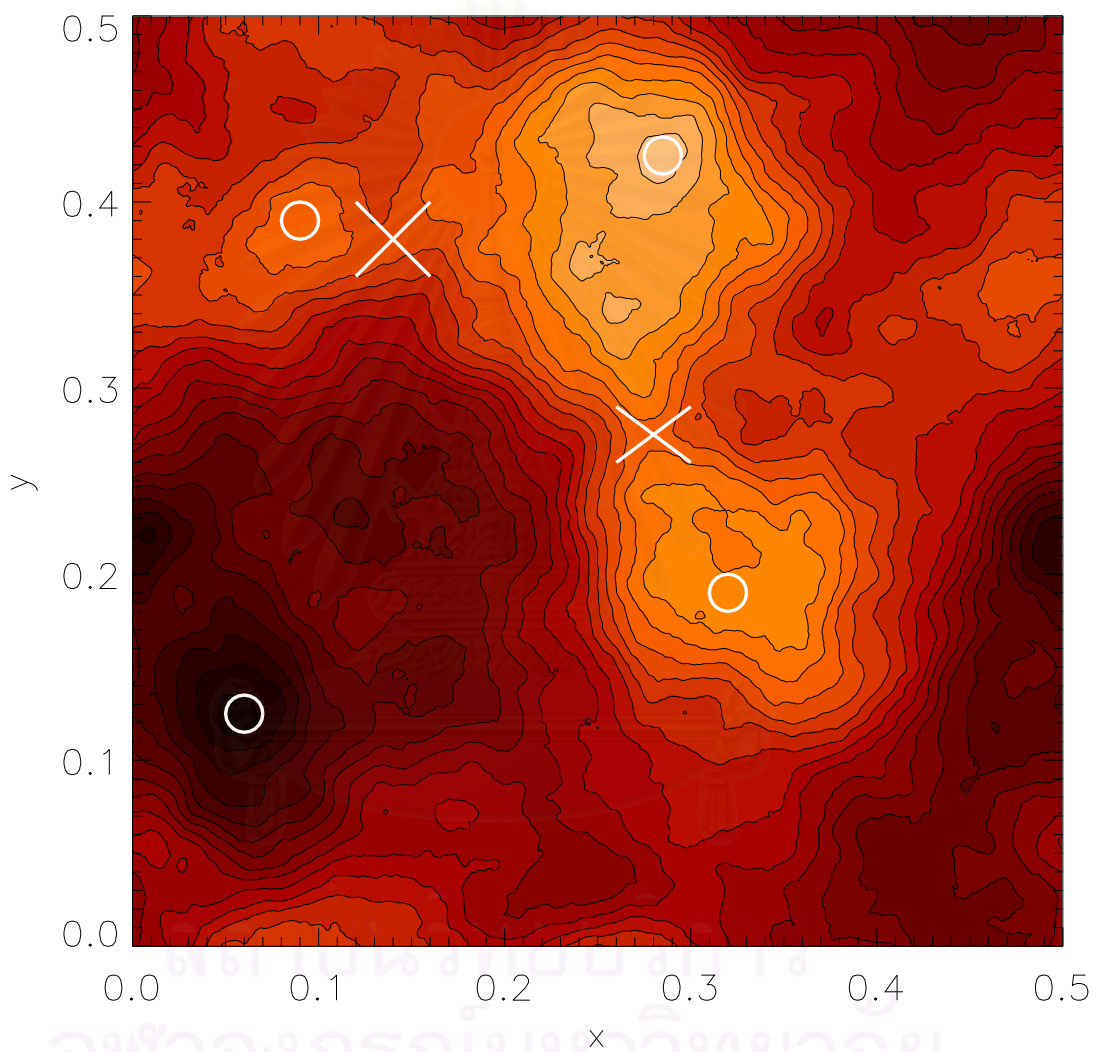


Figure 2.6: The contour plot of a potential function $a(x, y)$ for two-dimensional turbulence.

2.6 Dropout Phenomena from Observations

There were observations of solar energetic particles (SEPs) from many impulsive solar flare events by the Advanced Composition Explorer (ACE) spacecraft between 1997 November and 1999 July. Figure 2.7 shows an interesting time period with impulsive flare events during 1999 January 9 - 10, and data from the ACE spacecraft near 1 AU (Mazur et al. 2000). This figure shows the data of energy and density of H-Fe ions as a function of their arrival time and the rapid changes in the density of SEPs near Earth (appearing and disappearing repeatedly), which are called “dropouts.”

Mazur et al. (2000) and Giacalone et al. (2000) suggest that the fluid motions at the solar surface lead to a random walk of magnetic field lines and convection past the spacecraft of flux tubes that are sometimes filled and sometimes empty, giving rise to dropouts in the intensity. The timescale of the dropouts was about 2.5 minutes, which corresponds to a length scale of 7.5×10^7 m for a solar wind speed of 500 km hr^{-1} . Mazur et al. (2000) deduced an average timescale for the events of 3.8 hr, corresponding to a length scale of ~ 0.03 AU.

Another solar event on 1999 June 4 (Figure 2.8) was associated with a coronal mass ejection and an interplanetary shock. Figure 2.8 does not exhibit the dropout features that were seen for the impulsive flare of 1999 January 9. The difference is due to the relative sizes of the acceleration sites. In shock-related events, the temporal structure observed at 1 AU reflects the ever-changing magnetic connection of an observer to the expanding shock that covers a wide extent in heliolongitude. Any flux tube that ACE intersects will be populated with energetic ions as the shock propagates outward.

Ruffolo et al. (2003) explain an apparent conflict between two sets of recent observations of SEPs. The first is that impulsive solar flares can exhibit

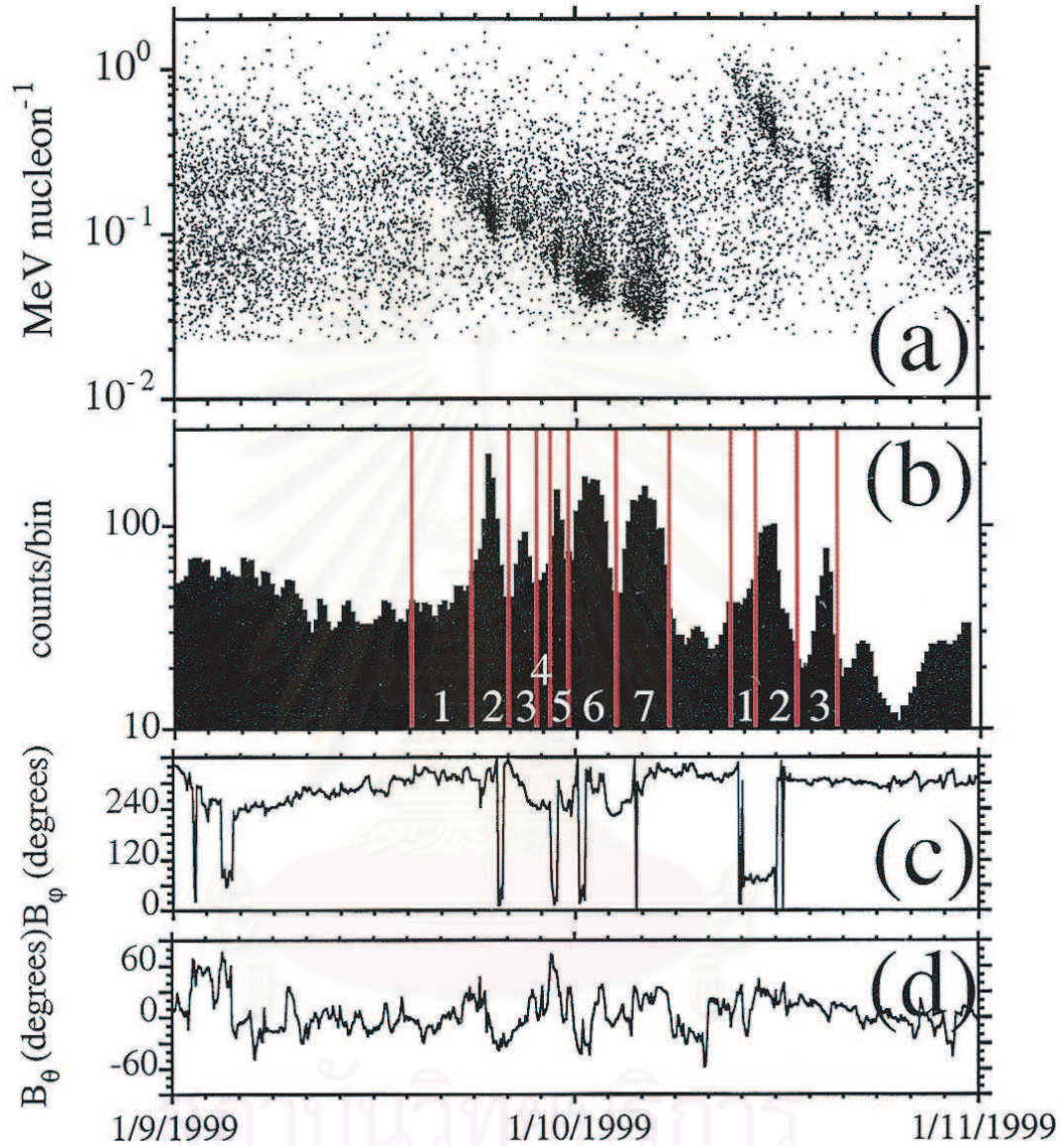


Figure 2.7: Dropouts in impulsive flare events of 1999 January 9-10 observed by Mazur et al. (2000). (a) Kinetic energy per mass of H-Fe ions in units of MeV nucleon^{-1} vs. arrival time at 1 AU. (b) H-Fe counts vs. time in ≈ 14 minute bins. The vertical lines show event subintervals. (c) Interplanetary magnetic field angle in the geocentric solar ecliptic (GSE) x - y plane. (d) Interplanetary magnetic field angle from the GSE x - y plane. (Image credit: Mazur et al. (2000))

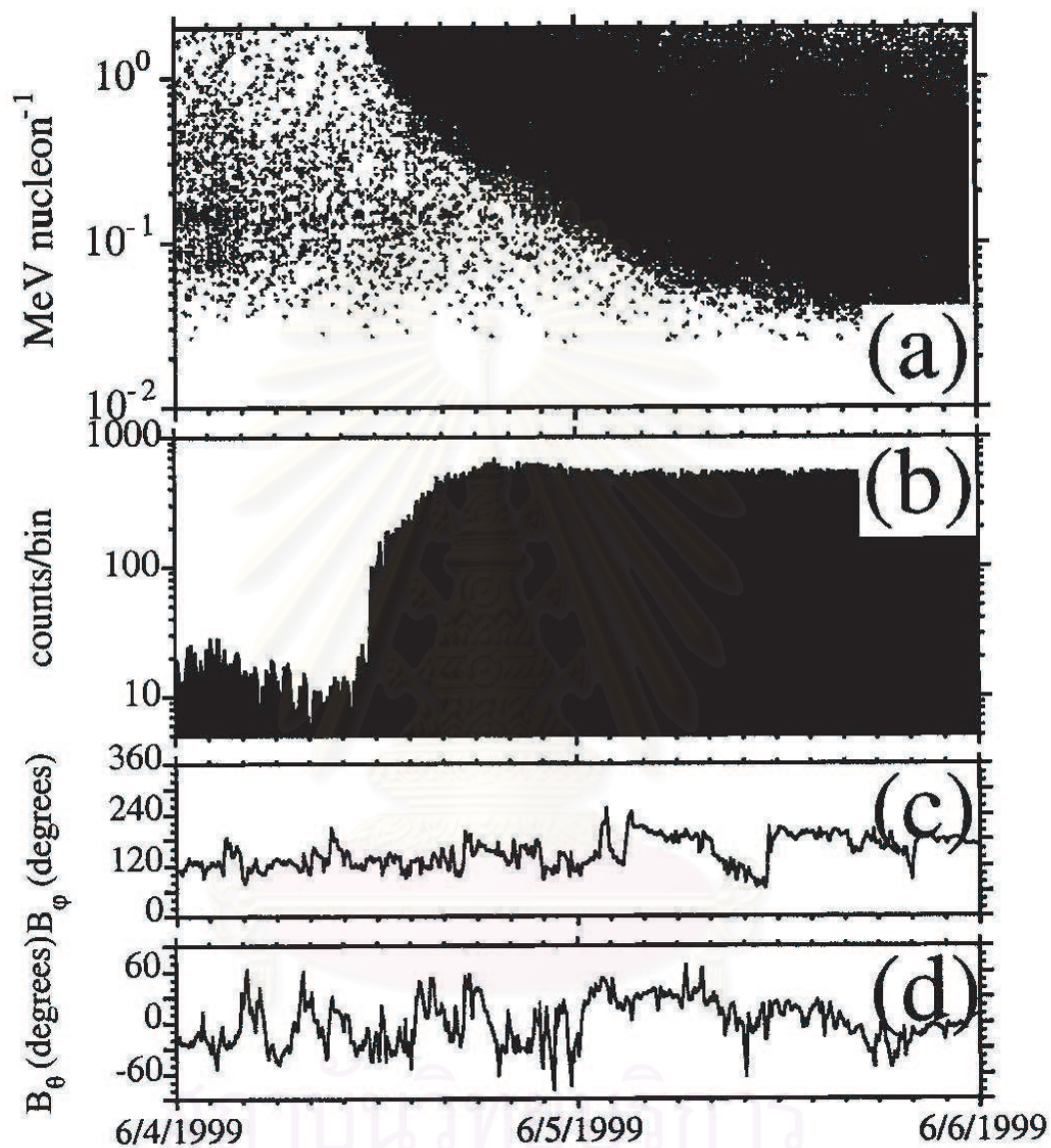


Figure 2.8: Data from a gradual event, with no apparent dropout features. (a) Energy of oxygen ions (in units of MeV nucleon^{-1}) vs. arrival time at 1 AU for the solar particle event of 1999 June 4. (b) Oxygen counts vs. time in 5 minute bins. (c) Interplanetary magnetic angle in the GSE x - y plane. (d) Interplanetary magnetic field angle from the GSE x - y plane. (Image credit: Mazur et al. (2000))

“dropouts” as observed by the ACE spacecraft (Mazur et al. 2000) in which the SEP density near Earth repeatedly disappears and reappears, indicating a filamentary distribution of SEPs and little diffusion across these boundaries. The second is the observation by the IMP-8 and Ulysses spacecraft, while they were on opposite sides of the Sun, showing similar time-intensity profiles for many SEP events, indicating a rapid lateral diffusion of particles throughout the inner solar system within a few days (McKibben et al. 2001, McKibben, 2005). They proposed to reconcile these observations in terms of a two-component model of the solar wind turbulent magnetic field, with slab and two-dimensional turbulence (see the next section). Their simulations were in a Cartesian geometry for simplicity. Their simulations show that the magnetic fields were trapped in topological structures of the 2D turbulence.

They supposed that the particles are injected in a spatially localized region, a circle of radius ρ . Then, they defined $z_1 = \rho^2/(4D)$ as a characteristic distance over which the field lines outside islands diffuse out of the circle. If an island has diameter d , then $z_2 = d^2/(16D_{slab})$ is the typical distance along the mean field over which field lines escape from the island due to the slab component of turbulence. If slab diffusion is weak (see Figure 2.9), dropouts are observed for $z_1 < z_{obs} < z_2$ conditions, where z_{obs} is the distance of the observer. That means the magnetic field lines and the low-energy particles orbiting them that start deep within islands mostly remain trapped while those outside the islands rapidly escape from the injection region, leaving gaps with a low density of particles. After a long distance, $z_{obs} > z_2$, all field lines have escaped their temporary topological traps, corresponding to a rapid lateral diffusion of field lines and of particles. For $z_1 > z_{obs}$, which occurs for a wide injection region, dropouts should not be seen. This can explain another class of solar events, gradual flare or coronal mass ejection (CME) events, such as the solar event on 1999 June 4

(see Figure 2.8), where particles are injected over a much wider region and do not exhibit dropouts. Figure 2.10 shows that at intermediate- z values, field lines within islands of the two-dimensional turbulence (around the O-points, see Figure 2.6) remain trapped, while field lines in other regions spread rapidly. This explains the filamentary distribution of particles as indicated by dropout features. At large z values, all field lines diffuse rapidly, which explains the Ulysses and IMP-8 observations of SEP diffusion throughout the inner solar system.

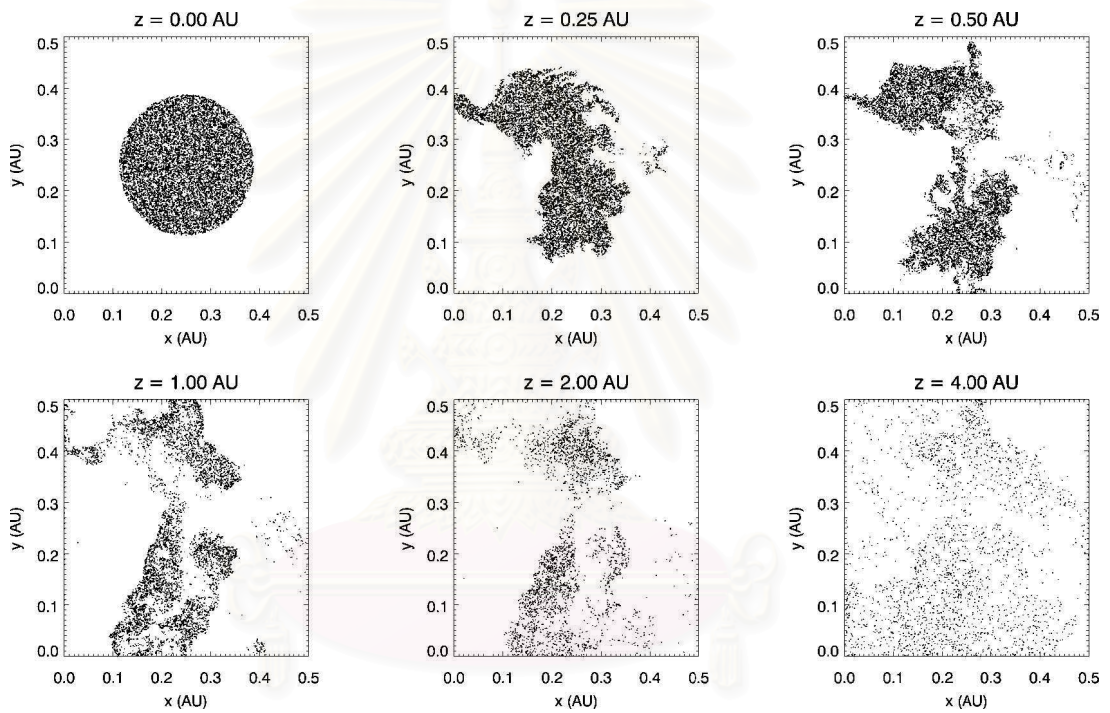


Figure 2.9: Scatter plot of the locations of magnetic field lines that are initially (at $z = 0$) located within a circle (simulating the region where particles are injected as a result of an impulsive solar flare). Parameter values are chosen to be appropriate for the solar wind. (Image credit: Ruffolo et al. (2003))

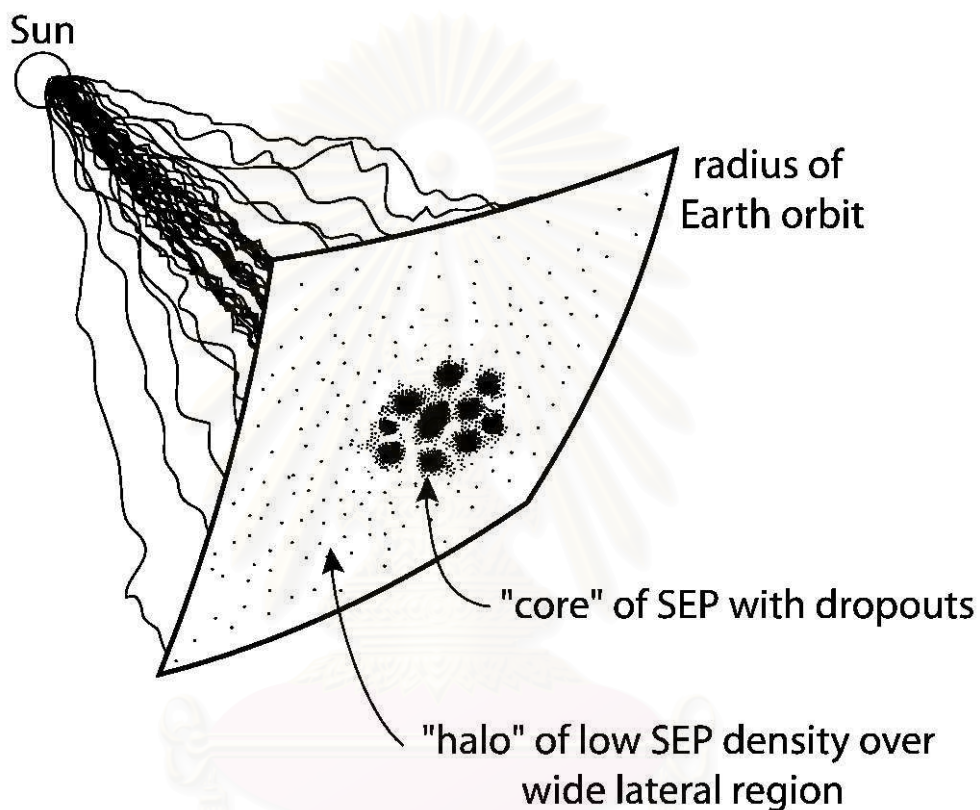


Figure 2.10: Illustration of interplanetary magnetic field lines populated with SEPs from a localized source region near the Sun, as expected for an impulsive solar flare. In the two-dimensional + slab model of solar wind turbulence, some field lines are trapped in filaments corresponding to the small-scale topology, i.e. islands of the two-dimensional turbulence, out to Earth orbit. (Image credit: Ruffolo et al. (2003))

2.7 Suppression of Diffusive Escape by a Strong 2D Field

Chuychai et al. (2005, 2007) simulated a slab turbulent field + 2D Gaussian field for a simple model and tested starting the field lines inside the 2D island. They found that the diffusion of field lines was initially much slower than the slab rate. There was a delay in attaining faster diffusion rates, indicating that field lines were trapped temporarily due to the strong 2D field. The 2D field can temporarily trap field lines and suppress the field line random walk at short to intermediate distances. For large distances, all field lines escape the 2D topology and diffuse asymptotically at the slab rate. For the field lines starting deeply inside the 2D island, the suppressed diffusion increases because the rapid motion around the trapping island decorrelates the radial component of the perturbation.

Chuychai et al. (2005) consider a region where the 2D field is much stronger than the slab component (which is believed to be common in the solar wind; Bieber et al. 1994, 1996). They treat the slab fluctuation as a perturbation and apply a quasi-linear approach. From section 3.1, the magnetic field line equation (3.3) is

$$\frac{dx}{B_x} = \frac{dy}{B_y} = \frac{dz}{B_z}.$$

In our model, we have $\mathbf{B} = B_0\hat{z} + b_x\hat{x} + b_y\hat{y}$, so we get

$$\frac{dx}{b_x} = \frac{dy}{b_y} = \frac{dz}{B_0}. \quad (2.16)$$

From eq.(2.16), the perpendicular displacements Δx and Δy are

$$\Delta x(\Delta z) = x(\Delta z) - x(0) = \int_0^{\Delta z} \frac{b_x(x'(z'), y'(z'), z')}{B_0} dz', \quad (2.17)$$

$$\Delta y(\Delta z) = y(\Delta z) - y(0) = \int_0^{\Delta z} \frac{b_y(x'(z'), y'(z'), z')}{B_0} dz'. \quad (2.18)$$

Chuychai et al. (2005) take the orbits of field lines to be approximately circular with angular velocity K . Then considering the radial coordinate, $r = \sqrt{x^2 + y^2}$, we obtain

$$\hat{x} = \hat{r} \cos \theta - \hat{\theta} \sin \theta, \quad (2.19)$$

$$\hat{y} = \hat{r} \sin \theta + \hat{\theta} \cos \theta, \quad (2.20)$$

$$\hat{z} = \hat{z}, \quad (2.21)$$

so the slab fluctuation can be written as

$$\mathbf{b}^{\text{slab}}(z) = (b_x^{\text{slab}}(z) \cos \theta + b_y^{\text{slab}}(z) \sin \theta) \hat{r} \quad (2.22)$$

$$+ (-b_x^{\text{slab}}(z) \sin \theta + b_y^{\text{slab}}(z) \cos \theta) \hat{\theta}. \quad (2.23)$$

The 2D part in polar coordinates can be written as

$$\mathbf{b}^{2\text{D}}(r) = -\frac{a(r)}{dr} \hat{\theta}. \quad (2.24)$$

Then the field line equation (2.16) gives

$$\frac{dr}{dz} = \frac{b_r}{B_z} = \frac{b_x^{\text{slab}} \cos \theta + b_y^{\text{slab}} \sin \theta}{B_0} = \frac{b_r^{\text{slab}}}{B_0} \quad (2.25)$$

$$\frac{d\theta}{dz} = \frac{1}{r} \frac{b_\theta}{B_z} = -\frac{1}{r B_0} \frac{da(r)}{dr} + \frac{b_y^{\text{slab}} \cos \theta - b_x^{\text{slab}} \sin \theta}{r B_0} \quad (2.26)$$

$$= K + \frac{b_\theta^{\text{slab}}}{r B_0}. \quad (2.27)$$

As in eq. (2.17) and eq. (2.18), the radial displacement, Δr can be written as

$$\Delta r(\Delta z) = r(\Delta z) - r(0) = \int_0^{\Delta z} \frac{b_r^{\text{slab}}(z')}{B_0} dz'. \quad (2.28)$$

Then, the mean squared displacement in the radial direction is

$$\langle \Delta r^2 \rangle = \frac{1}{B_0^2} \int_0^{\Delta z} \int_0^{\Delta z} \langle b_r^{\text{slab}}(z') b_r^{\text{slab}}(z'') \rangle dz' dz'', \quad (2.29)$$

where $b_r^{\text{slab}}(z)$ is the projection of the slab field in the radial direction, which changes during the circular motion. In terms of the slab correlation function $R_{xx}^{\text{slab}}(\Delta z')$, with $\Delta z' \equiv z'' - z'$ and assuming axisymmetry so that $R_{xx}^{\text{slab}} = R_{yy}^{\text{slab}}$, then

$$\langle \Delta r^2 \rangle = \frac{1}{B_0^2} \int_0^{\Delta z} \int_{-\infty}^{\infty} R_{xx}^{\text{slab}}(\Delta z') \cos(K \Delta z') d\Delta z' dz', \quad (2.30)$$

where the integration over all $\Delta z'$ is a valid approximation when $\Delta z \gg l_c$ where l_c is the a slab correlation length. Eq.(2.30) can be rewritten in terms of the slab power spectrum $P_{xx}^{\text{slab}}(k_z)$,

$$\langle \Delta r^2 \rangle = \frac{1}{\sqrt{2\pi} B_0^2} \int_0^{\Delta z} \int_{-\infty}^{\infty} \int_{-\infty}^{\infty} P_{xx}^{\text{slab}}(k_z) e^{-ik_z \Delta z'} \times \cos(K \Delta z') dk_z d\Delta z' dz'. \quad (2.31)$$

Then the diffusion coefficient of the field line in radial direction is

$$D_{rr} = \frac{\langle (\Delta r)^2 \rangle}{2 \Delta z} = \sqrt{\frac{\pi}{2}} \frac{P_{xx}(K)}{B_0^2} = D_{\text{slab}} \frac{P_{xx}(K)}{P_{xx}(0)}, \quad (2.32)$$

where D_{slab} is the standard quasi-linear slab. The theoretical result in Eq.(2.32) tells us that radial motion of the field lines deep inside the 2D island is diffusive and is associated with the slab power spectrum at the wavenumber that is resonant with the 2D angular velocity at the original radius.

The suppressed diffusion is an important process to explain dropout features of field lines over a distance of 1 AU. Field lines that start near O- or X-points have different rates of lateral diffusion. The field lines starting near O-points experience suppressed diffusion and diffuse in the direction perpendicular to the mean magnetic field more slowly than the field lines near X-points (see Figure 2.11). These different rates of spreading lead to inhomogeneous features and sharp gradients in the field line density.

The dropout-like distribution of field lines might represent the distribution of SEPs injected from a localized source near the Sun, though this needs to be proven by particle simulation. Before my thesis work, these ideas were explored only in terms of field line trajectories, not particle motion.

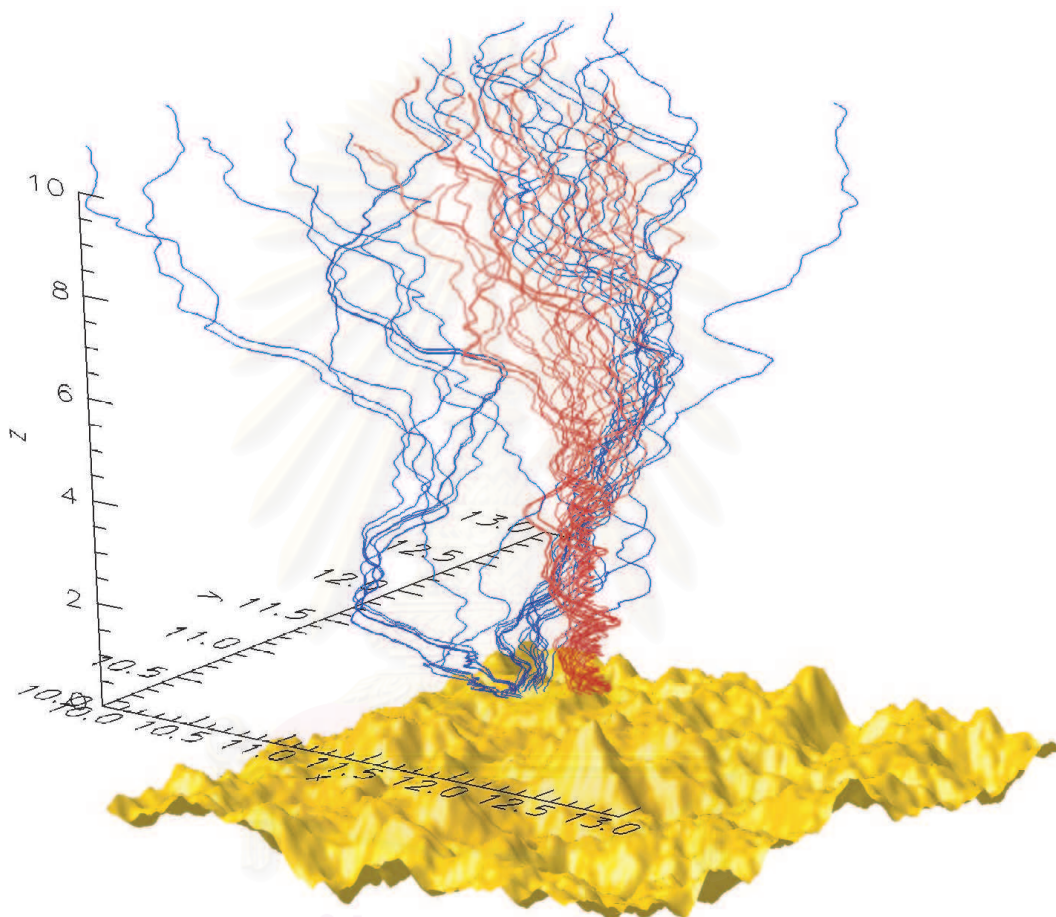


Figure 2.11: Magnetic field line trajectories in a representation of 2D + slab turbulence starting near an O-point (red) and X-point (blue). The surface plot at the bottom shows the potential function $a(x, y)$ corresponding to the 2D turbulence. (Image credit: Chuychai et al. (2007))

Chapter III

Numerical Methods in Cartesian Geometry

3.1 Tracing Magnetic Field Lines in Cartesian Geometry

After we obtain the magnetic field in three-dimensional space from 2D + slab magnetic turbulence, next we can trace the magnetic field lines in Cartesian geometry by using the differential equation determining these lines:

$$d\mathbf{l} \times \mathbf{B} = 0, \quad (3.1)$$

where $d\mathbf{l}$ is a small displacement vector along the magnetic field with component $(dx, dy, \text{ and } dz)$ and \mathbf{B} is the magnetic field vector. Then we obtain

$$(dx \hat{x} + dy \hat{y} + dz \hat{z}) \times (B_x \hat{x} + B_y \hat{y} + B_z \hat{z}) = 0, \quad (3.2)$$

$$\begin{vmatrix} \hat{x} & \hat{y} & \hat{z} \\ dx & dy & dz \\ B_x & B_y & B_z \end{vmatrix} = 0,$$

$$(B_z dy - B_y dz) \hat{x} + (B_x dz - B_z dx) \hat{y} + (B_y dx - B_x dy) \hat{z} = 0.$$

The solution of this equation is

$$\frac{dx}{B_x} = \frac{dy}{B_y} = \frac{dz}{B_z}, \quad (3.3)$$

where B_x , B_y , and B_z are the x , y , and z components of the magnetic field. For this work, we also set

$$\frac{ds}{|\mathbf{B}|} = \frac{dx}{B_x} = \frac{dy}{B_y} = \frac{dz}{B_z}, \quad (3.4)$$

where $ds = \sqrt{dx^2 + dy^2 + dz^2}$ and $|\mathbf{B}| = \sqrt{B_x^2 + B_y^2 + B_z^2}$.

Figures 3.1 - 3.3 show examples of trajectories of 3 types of magnetic field lines from eq. (3.4). The first is pure slab, for which the field lines depend only on z , so each field line in Figure 3.1 looks the same. The second is pure 2D, for which the field lines move along contours of constant $a(x, y)$, because $\mathbf{b} = \nabla \times a\hat{z}$ is perpendicular to the gradient of $a(x, y)$ (see Figure 3.2). Finally the slab + 2D magnetic field lines (see Figure 3.3) have structure in three dimensions, which provides a more realistic magnetic field for our simulations.

For the 2D + slab model, $B_x = b_x^{\text{slab}} + b_x^{2\text{D}}$, $B_y = b_y^{\text{slab}} + b_y^{2\text{D}}$, and $B_z = B_0$. Here $b_z = 0$ and z can be used as an independent variable to describe the field line trajectory. Then

$$\frac{dx}{dz} = \frac{b_x(x, y, z)}{B_0} = \frac{b_x^{\text{slab}}(z) + b_x^{2\text{D}}(x, y)}{B_0}, \quad (3.5)$$

$$\frac{dy}{dz} = \frac{b_y(x, y, z)}{B_0} = \frac{b_y^{\text{slab}}(z) + b_y^{2\text{D}}(x, y)}{B_0}. \quad (3.6)$$

The field line displacement in the perpendicular direction from the mean magnetic field along the z directions can be a process of field line diffusion. A particle diffusion coefficient is defined by

$$\kappa = \frac{\langle(\Delta x)^2\rangle}{2\Delta t}, \quad (3.7)$$

where $\langle\Delta x^2\rangle$ is the mean square displacement of the particle, Δt is the time difference, and κ is the diffusion coefficient of the particles. For field lines, we can similarly define a perpendicular diffusion coefficient as

$$D_{\perp} = \frac{\langle\Delta \mathbf{x}_{\perp}^2\rangle}{4\Delta z}, \quad (3.8)$$

where $\langle\Delta \mathbf{x}_{\perp}^2\rangle = \langle(\Delta x)^2\rangle + \langle(\Delta y)^2\rangle$ is the mean square perpendicular displacement of magnetic field lines, D_{\perp} is the perpendicular diffusion coefficient of the

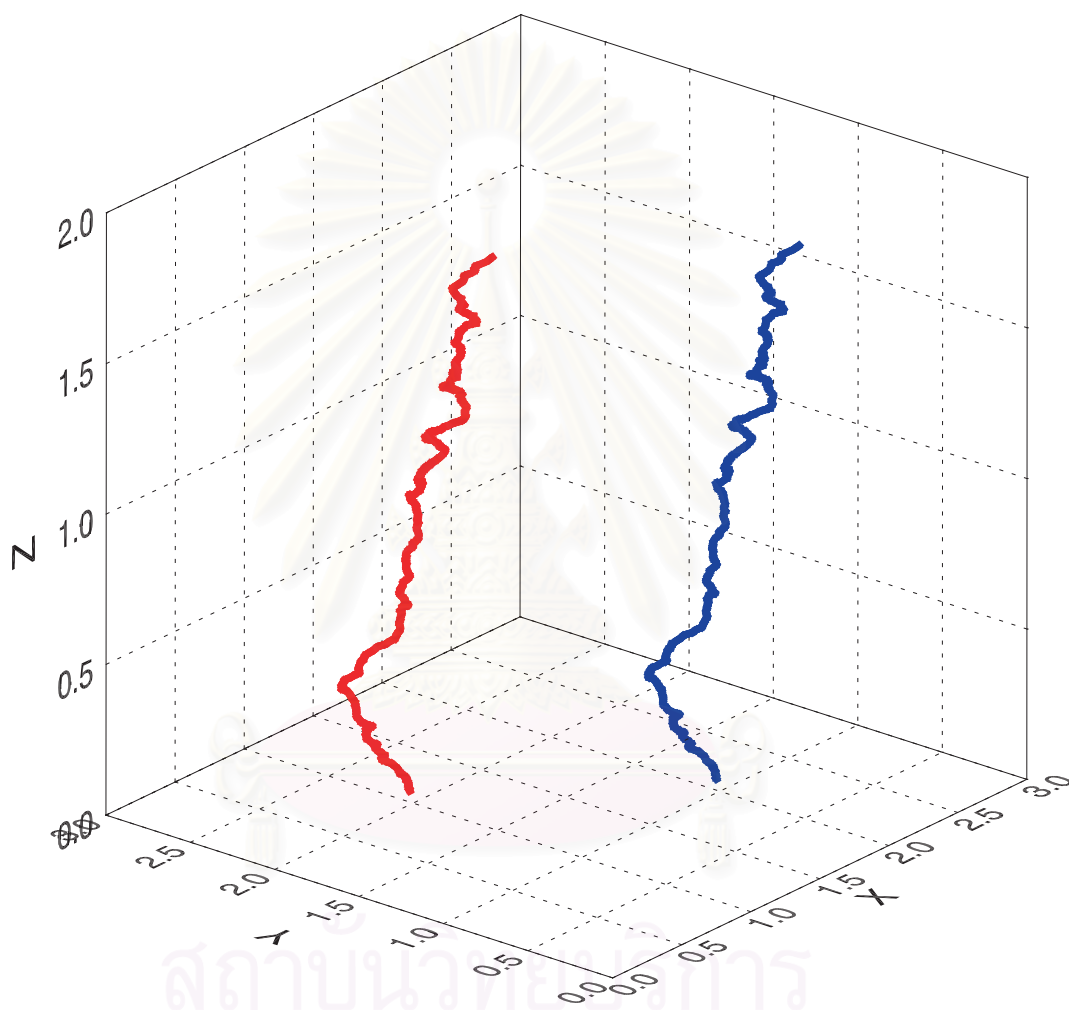


Figure 3.1: Example of the trajectory of two magnetic field lines in the pure slab magnetic fluctuation plus mean field.

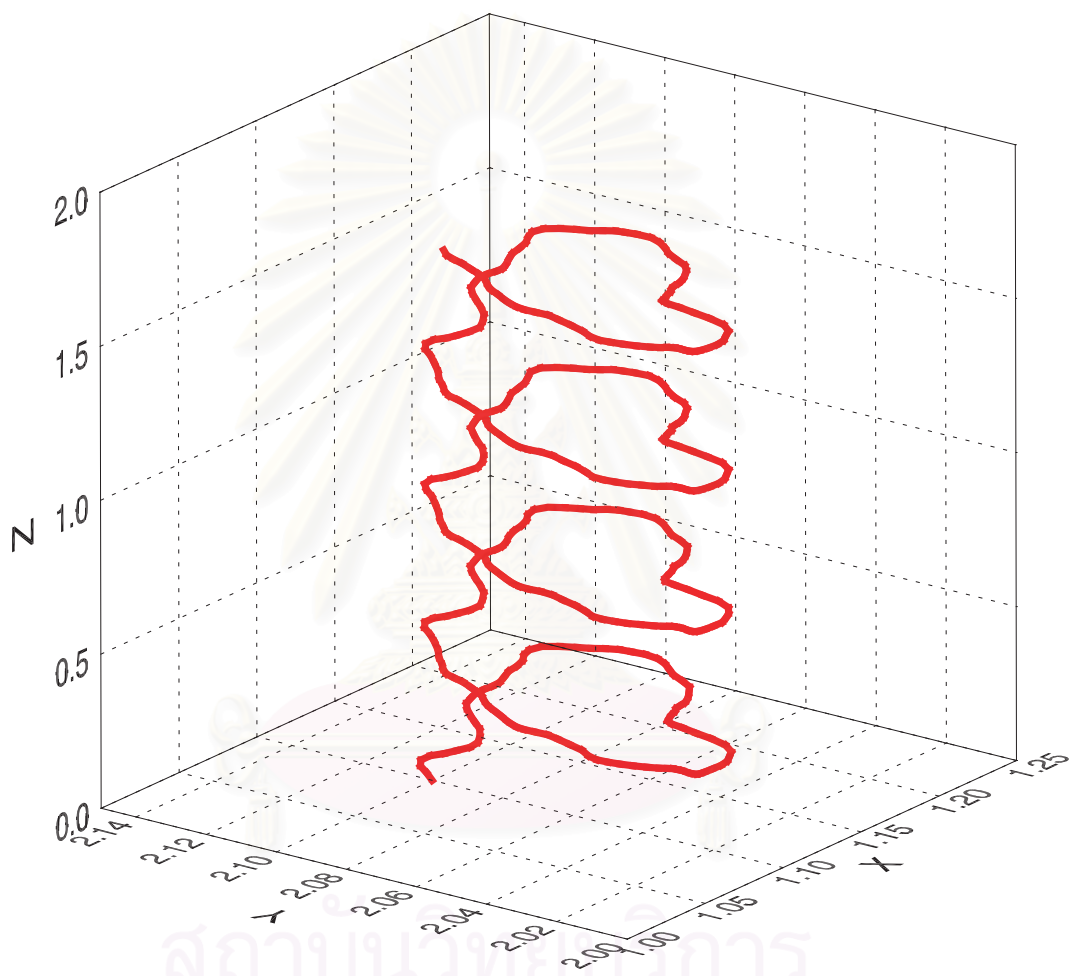


Figure 3.2: Example of the trajectory of a field line in a pure 2D magnetic fluctuation plus mean field.

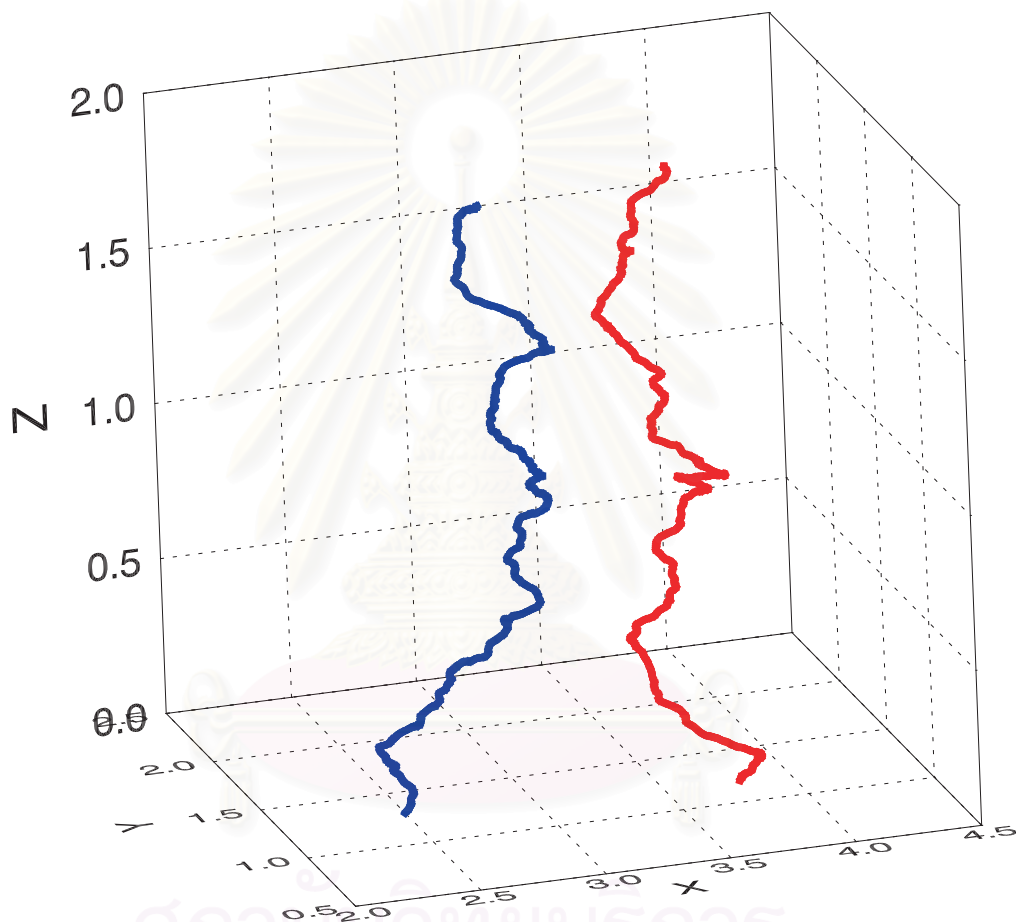


Figure 3.3: Example of two trajectories in slab plus 2D fluctuations plus the mean magnetic field.

field lines, and Δz is the displacement of the magnetic field lines along the z direction. If the turbulence is axisymmetric, then $\langle(\Delta x)^2\rangle = \langle(\Delta y)^2\rangle$. Then the perpendicular diffusion coefficient of the field lines is also given by

$$D_{\perp} = \frac{\langle(\Delta x)^2\rangle}{2\Delta z} = \frac{\langle(\Delta y)^2\rangle}{2\Delta z}. \quad (3.9)$$

3.2 Tracing Particle Motion in Cartesian Coordinates

When charged particles move in a constant magnetic field, they follow helical orbits along magnetic field lines. For a random magnetic field, we can trace the particle motion by using a numerical method. We can trace the charged particle motion by using the Newton-Lorentz force equation given as

$$\mathbf{F} = \gamma m \mathbf{a} = \gamma m \frac{d\mathbf{v}}{dt}, \quad (3.10)$$

where m is the mass of the charged particle, \mathbf{v} is the vector velocity of the particle, γ is the Lorentz factor $\gamma = \sqrt{1 - v^2/c^2}$, and

$$\mathbf{F} = q\mathbf{v} \times \mathbf{B}, \quad (3.11)$$

where q is the charge and \mathbf{B} is the magnetic field vector. Then we have

$$(F_x \hat{i} + F_y \hat{j} + F_z \hat{k}) = q(v_x \hat{i} + v_y \hat{j} + v_z \hat{k}) \times (B_x \hat{i} + B_y \hat{j} + B_z \hat{k}) \quad (3.12)$$

$$\begin{aligned} \gamma m(a_x \hat{i} + a_y \hat{j} + a_z \hat{k}) &= q \begin{vmatrix} \hat{i} & \hat{j} & \hat{k} \\ v_x & v_y & v_z \\ B_x & B_y & B_z \end{vmatrix} \\ &= q[(v_y B_z - v_z B_y) \hat{i} + (v_z B_x - v_x B_z) \hat{j} \\ &\quad + (v_x B_y - v_y B_x) \hat{k}] \end{aligned}$$

These equations are coupled:

$$\left. \begin{aligned} \frac{dv_x}{dt} &= \frac{q}{\gamma m} (v_y B_z - v_z B_y), \\ \frac{dv_y}{dt} &= \frac{q}{\gamma m} (v_z B_x - v_x B_z), \\ \frac{dv_z}{dt} &= \frac{q}{\gamma m} (v_x B_y - v_y B_x). \end{aligned} \right\} \quad (3.13)$$

Note also that B_x and B_y are random functions of position (x, y, z) .

In this work, we normalize to a set of units for all quantities scaled to the mean magnetic field (B_0), the speed of light, the slab turbulence coherence length (l_{\parallel}), and the time scale $\tau_0 = l_{\parallel}/c$. Then the equations of motion become (see Appendix A)

$$\frac{d\mathbf{v}^*}{dt^*} = \alpha (\mathbf{v}^* \times \mathbf{B}^*), \quad (3.14)$$

where $\alpha = (qB_0\tau_0)/(\gamma m_0)$, and $\mathbf{v}^* = \mathbf{v}/c$, $\mathbf{B}^* = \mathbf{B}/B_0$, and $t^* = l_{\parallel}/c$ are normalized quantities (Tooprakai et al. 2007). Then eq.(3.13) becomes

$$\left. \begin{aligned} \frac{dv_x^*}{dt^*} &= \alpha (v_y^* B_z^* - v_z^* B_y^*), \\ \frac{dv_y^*}{dt^*} &= \alpha (v_z^* B_x^* - v_x^* B_z^*), \\ \frac{dv_z^*}{dt^*} &= \alpha (v_x^* B_y^* - v_y^* B_x^*). \end{aligned} \right\} \quad (3.15)$$

สถาบันวิทยบริการ
จุฬาลงกรณ์มหาวิทยาลัย

Chapter IV

Results of Simulations of Particle Transport in Cartesian Geometry

Here we will show our results on particle motion in the magnetic field consisting of a Gaussian 2D flux tube, slab turbulence, and a uniform field $B_0\hat{z}$. For the 2D flux tube, the potential function $a(x, y)$ is chosen as a Gaussian function (see Appendix C):

$$a(r) = A_0 \exp\left[-\frac{r^2}{2\sigma^2}\right], \quad (4.1)$$

where A_0 is the central maximum value, σ determines the thickness of the Gaussian, and distance $r = \sqrt{x^2 + y^2}$ is measured from the axis of the flux tube. Therefore, from $\mathbf{B} = \nabla \times \mathbf{A}$, we can write

$$\mathbf{b}^{2D}(r) = \frac{ra(r)}{\sigma^2} \hat{\theta}, \quad (4.2)$$

where $\hat{\theta}$ is the unit vector associated with the angular coordinate in a cylindrical coordinate system defined by the flux tube axis. Without the slab field, the field line trajectory in this model, $B_0\hat{z} + \mathbf{b}^{2D}(x, y)$, has a helical orbit along a cylinder surface of constant $a(x, y)$ with a constant angular frequency $K = a(r_0)/(B_0\sigma^2) = (b^{2D}(r_0)/B_0)/r_0$, where r_0 is the starting radius. For the slab turbulence we choose the spectrum

$$P_{xx}^{\text{slab}}(k_z) = P_{yy}^{\text{slab}}(k_z) = \frac{C}{[1 + (k_z l_{\parallel})^2]^{5/6}}, \quad (4.3)$$

where l_{\parallel} is a coherence length and C is constant. Then the magnetic field turbulence in k -space is set to be

$$b_i^{\text{slab}}(k_z) = \sqrt{P_{ii}^{\text{slab}}(k_z)} \exp[i\phi(k_z)] \quad (4.4)$$

where $i = x, y$, and ϕ is a random phase. After that we use an inverse fast Fourier transform to get the magnetic field $b_i(z)$ in real space (Chuychai, 2004).

For the numerical simulations, we set the box length in the z direction as $10,000l_{\parallel}$ and the number of grid points is $N_z = 4,194,304$. We are particularly interested in small flux ropes surrounding O-points in 2D turbulence, which are permeated by homogeneous mean and slab fields, so we keep constant the mean field (B_0), all parameters of the slab turbulence, and the width of the 2D island ($\delta b_{slab}/B_0 = 0.5$ and $\sigma = 0.5l_{\parallel}$, where $B_0 = 5$ nT and $l_{\parallel} = 0.02$ AU). These parameters roughly represent conditions in interplanetary space near Earth. In different numerical experiments we vary the strength of the 2D field - which indeed does vary in interplanetary space - by changing b_{2D}^{max} . For these simulations, we define $b_{2D}^{max}/B_0 = 0.0, 0.5, 1.0, \text{ and } 1.58$ for pure slab, low B , medium B , and high B ; which is equivalent to $(b_{2D}^{max}/\delta b_{slab})^2 = 0.0, 1.0, 4.0, \text{ and } 10.0$, respectively.

For the particles, we use the particles at three different energies as presented in Table 4.1. The energies are referred to as high energy (1 MeV), medium energy (0.1 MeV) and low energy (20 keV). All parameters we use here, such as the Larmor radius $r_L = \gamma m_0 v / (|q| B_0)$, and the test particles are designed to represent protons. Given our choice of B_0 , these values of the Larmor radius r_L roughly match the maximum gyroradius of such particles in interplanetary space near Earth.

Figure 4.1 shows sample particle trajectories for low energy and high flux tube field strength (low E and high B , showing particles and field lines starting at $z = 0$ for clarity of presentation). At the coarsest spatial resolution one sees a collection of guiding centers that are initially confined to the flux surfaces of the 2D flux tube, but gradually escape (towards the top of the Figure.) At finer spatial scales (lower inset) the individual particle trajectories become apparent, and one sees that they follow slightly different field lines. At the finest resolution

(upper inset) the gyro-orbits become apparent and are the dominant feature. It is apparent that the magnetic field, and therefore the particle orbits, exhibit a multi-scale structure.

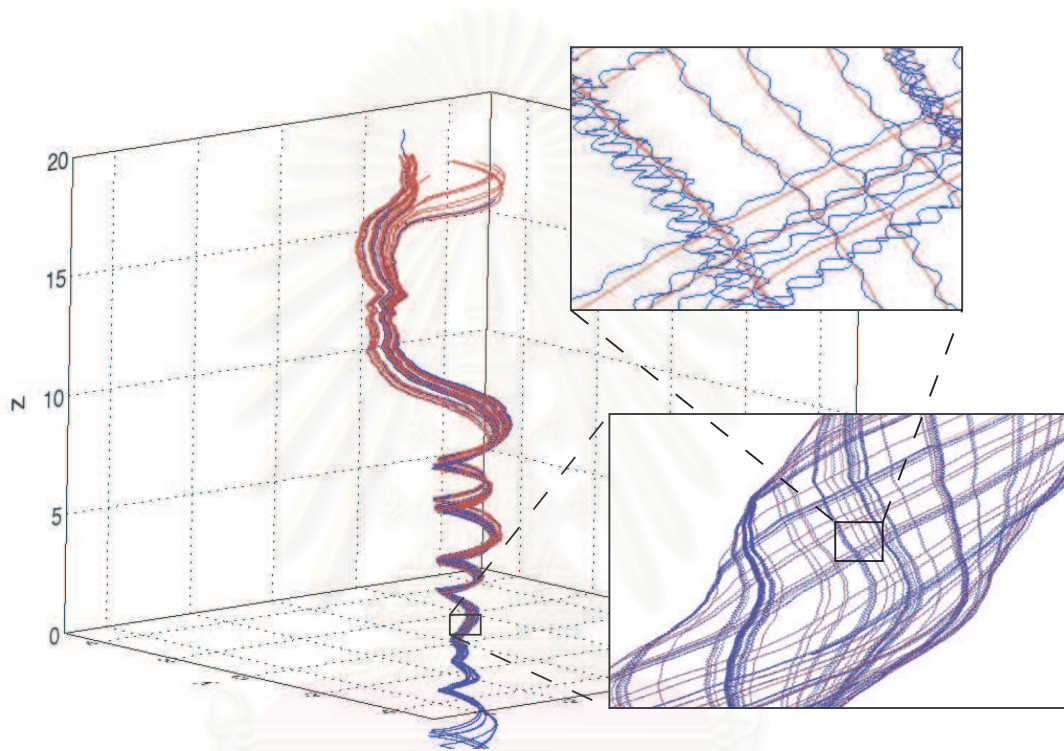


Figure 4.1: Illustration of 50 magnetic field lines (red) and the trajectories of 50 particles (blue) with the same initial positions that start at $z = 0, r = 0.1l_{\parallel}$ in a mean field + Gaussian 2D field + slab turbulence. Here the parameters of the 2D field are the same as in the high B case and all particles have low E . In the main plot, while trapped, the field lines map out regular flux surfaces of the Gaussian flux tube until their escape. Note that some particles undergo resonant pitch angle scattering and move downward to $z < 0$. In the lower inset, individual guiding center motion is evident. In the inset showing the most magnified view, the gyration of individual particles is seen.

Figures 4.2 - 4.4 show the mean square displacements vs. time (upper panels) and running diffusion coefficients (lower panels) for various 2D magnetic fields. These three figures show how low, medium, and high energy particles,

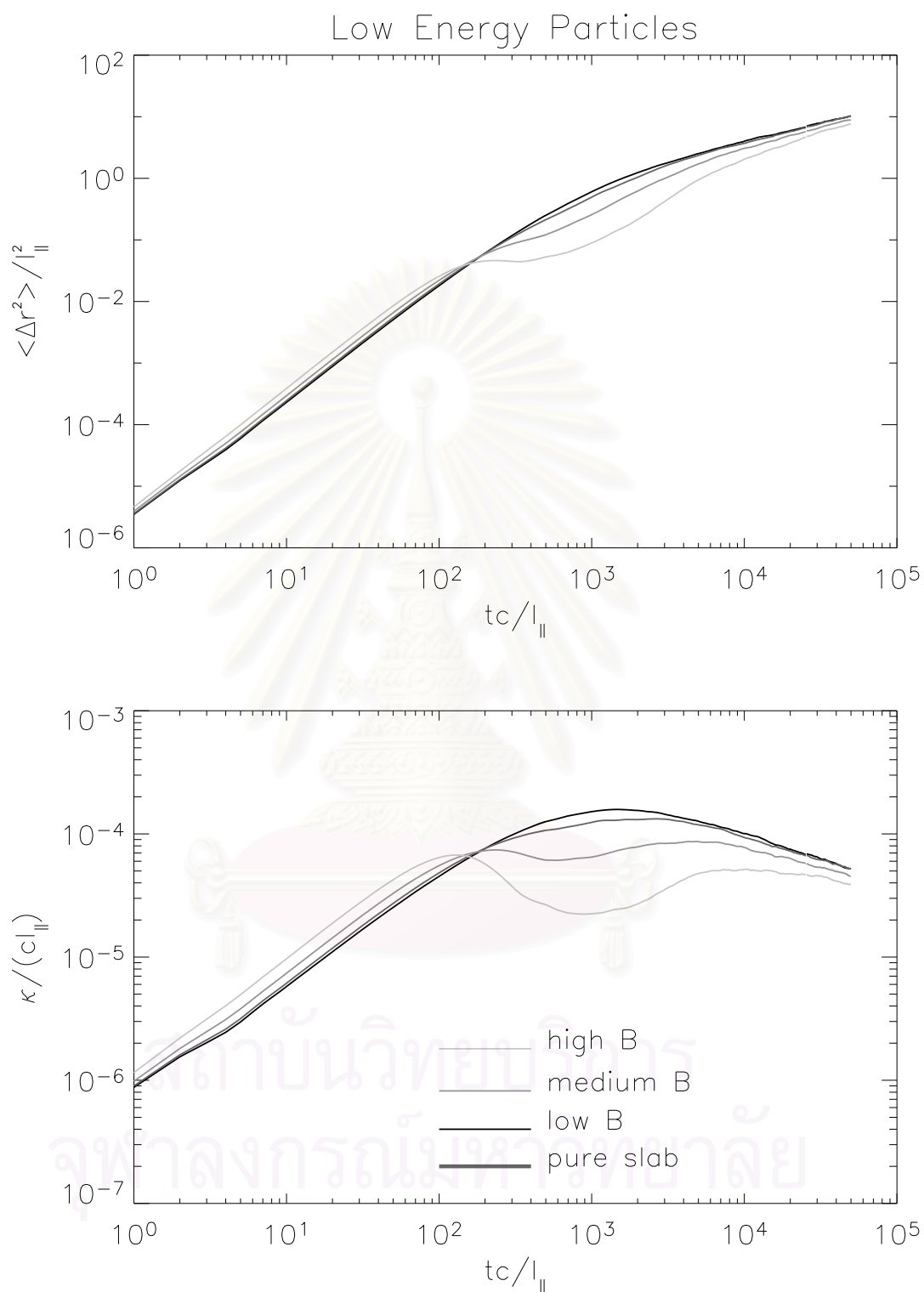


Figure 4.2: Illustration of low energy particle transport with varying magnetic fields. Upper panel: Mean squared perpendicular displacement $\langle \Delta r^2 \rangle$ vs. time t for various cases. Lower panel: Running perpendicular diffusion coefficient $\kappa = \langle \Delta r^2 \rangle / (4t)$ vs. time t for various cases.

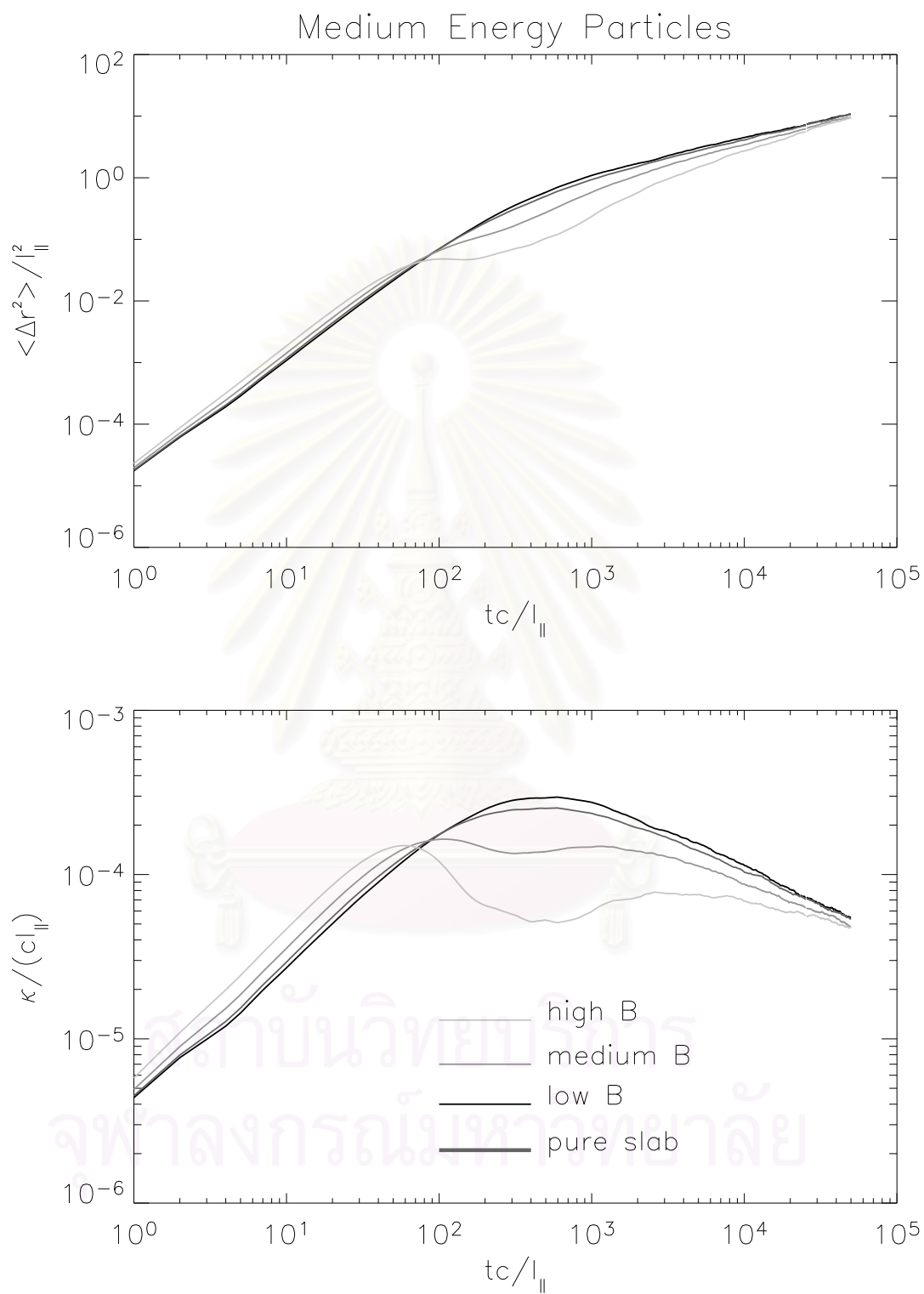


Figure 4.3: Like Figure 4.2, for medium energy particles.

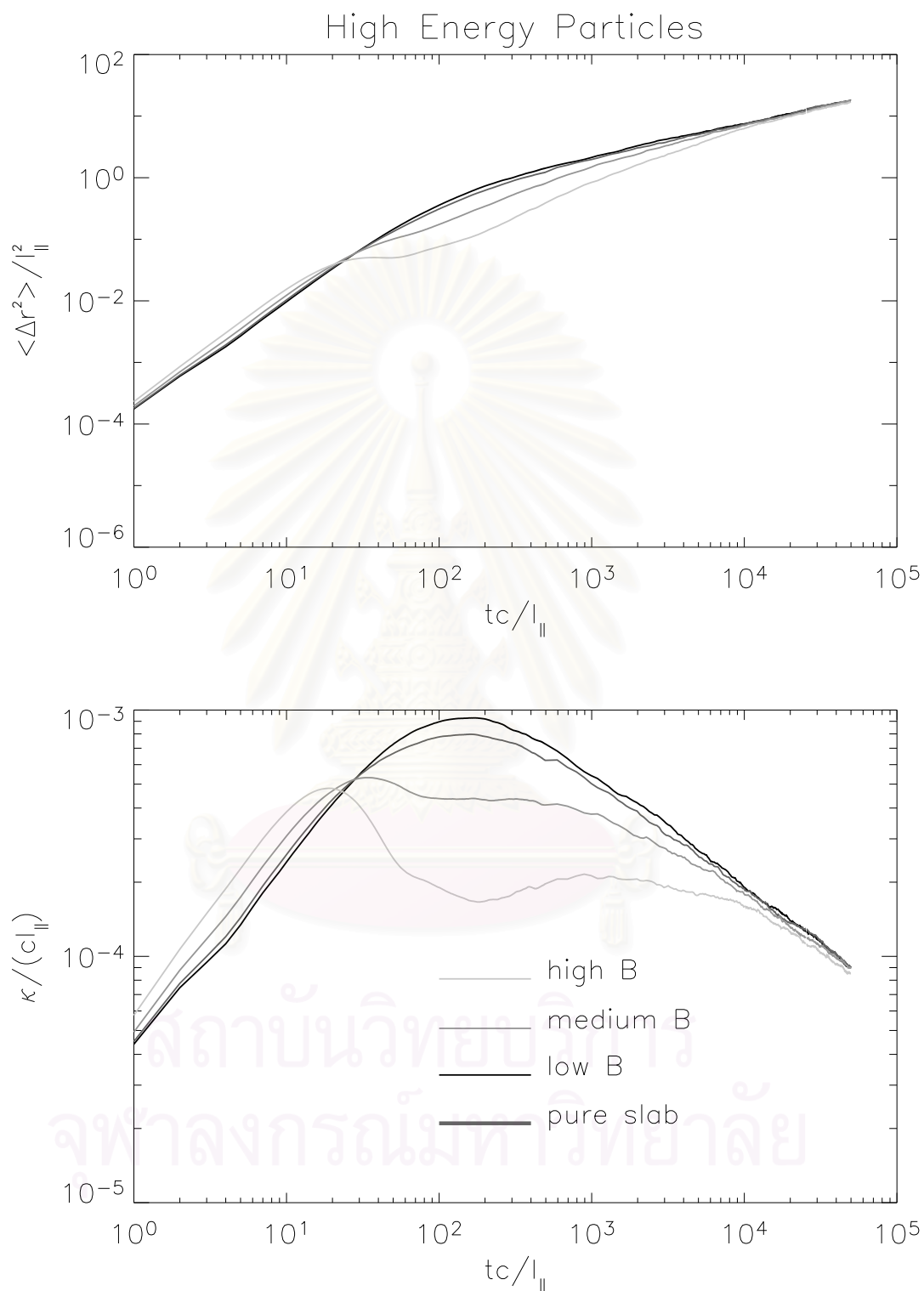


Figure 4.4: Like Figure 4.2, for high energy particles.

respectively, behave in flux tubes of varying strength, with other parameters fixed. The pure slab case is considered as well, and is the limit of a zero strength 2D flux tube. The time-varying features introduced by the 2D flux tubes are more prominent as the flux tube field strength increases.

Figure 4.5 shows the mean square displacements vs. time for medium energy particles and the high B and pure slab fields (upper panel). These displacements, measured perpendicular to $B_0\hat{z}$, have a more complex behavior with the flux tube present. In the lower panel, particle transport with a varying 2D field and particle energy is illustrated in terms of the time-dependent running diffusion coefficient, κ . It is clear that κ does not monotonically approach a time asymptotic form of the transport. For all cases that include a 2D flux tube, there is a period of time in which the rate of transport is suppressed. Based on analyses such as these, we identify four regimes of particle transport in these numerical experiments (Figure 4.5, upper panel), seen most clearly in the cases of lower energy and higher flux tube magnetic field:

I. Streaming regime ($\langle\Delta r^2\rangle \propto t^2$): the particles orbit around the field lines which are mainly confined to the 2D flux tube surface. The effects of the slab turbulence on these trajectories is small at this stage. This persists until the first peak in the diffusion coefficient plot (Figure 4.5, lower panel), estimated by $t = s/v$, where

$$s = \pi r_0 \sqrt{1 + \left[\frac{B_0}{b_{2D}(r_0)} \right]^2} \quad (4.5)$$

corresponds to a half cycle of the helical field line trajectory (see Appendix D) and v is the rms isotropic speed ($|\mathbf{v}|/\sqrt{3}$) of the particles, as shown in Table 4.1. This calculated time of the first peak agrees reasonably well with the simulation results.

II. Temporary trapping regime and suppressed diffusion ($\langle\Delta r^2\rangle \propto$ from

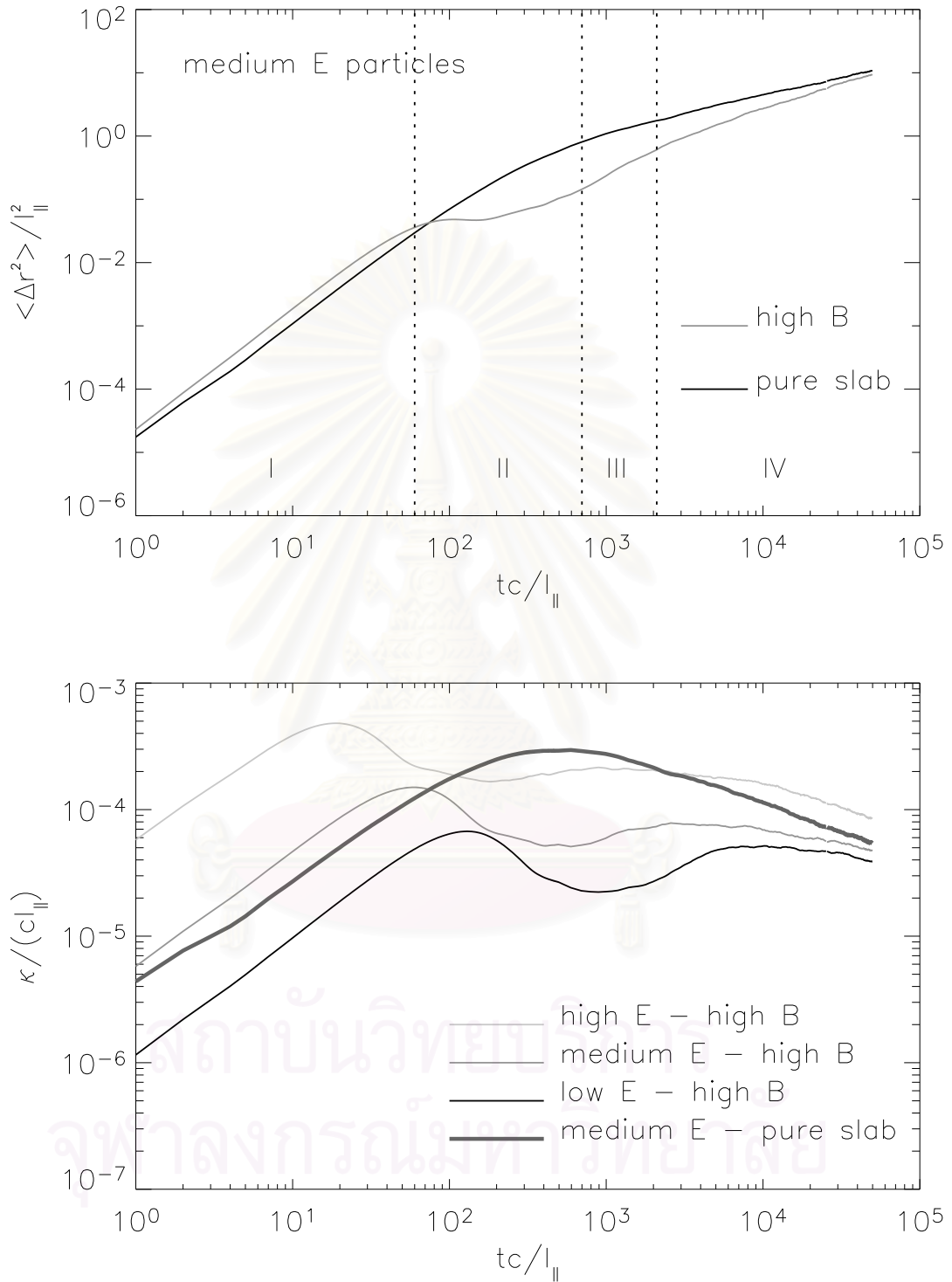


Figure 4.5: Upper panel: Mean squared perpendicular displacement $\langle \Delta r^2 \rangle$ vs. time t for medium energy particles for a strong 2D flux tube or pure slab turbulence. Lower panel: Running perpendicular diffusion coefficient $\kappa = \langle \Delta r^2 \rangle / (4t)$ vs. time t for various cases. There is more trapping for lower energy particles and for stronger 2D flux tubes.

t^0 to t^1): The particles have filled the flux tube surface and are temporarily trapped on it. The gyrocenters follow an approximately helical path, and the radial coordinates of the particles begin to increase slowly. This broadening briefly reaches a slow diffusive rate of transport as the gyrocenters follow field lines which themselves are experiencing a suppressed diffusive escape from the flux tube (Chuychai et al., 2005).

III. Escape region ($\langle \Delta r^2 \rangle$ from t^1 to t^2): As the particle population escapes the 2D flux tube, the transport is increasingly dominated by the stronger (unsuppressed) effects of the slab turbulence. This corresponds to a superdiffusive regime (equivalent to a second free streaming regime) in which the transition to this higher rate of transport is accomplished for the entire population.

IV. Asymptotic transport: Subdiffusion regime ($\langle \Delta r^2 \rangle \propto t^{1/2}$): After escape, the particles experience the full effect of the exterior turbulence. In many cases this would be an asymptotic diffusive regime. However for the present simplified model, the displacements become subdiffusive in the exterior pure slab turbulence because of the parallel scattering (see Qin et al., 2002a, 2002b; Webb et al., 2006). This final regime of transport begins at the second peak corresponding to the estimated parallel scattering time.

Table 4.1: Particle parameters for $B_0 = 5$ nT and $l_{\parallel} = 0.02$ AU, and simulated/calculated arrival time of the particles at the first peak (in units of l_{\parallel}/c)

	Energy (MeV)	$ \mathbf{v} $ (c)	r_L (l_{\parallel})	r_L (AU)	α	Time to first peak (simulated / calculated)		
						low B	medium B	high B
low E	0.02	0.0065	0.00136	2.73×10^{-5}	4.780	2000 / 1254	240 / 271	200 / 183
medium E	0.10	0.0146	0.00305	6.11×10^{-5}	4.779	600 / 560	98 / 121	62 / 82
high E	1.00	0.0461	0.00966	1.93×10^{-4}	4.775	200 / 177	38 / 38	20 / 26

Figure 4.5 includes reference curves of transport in pure slab turbulence for medium particle. For the pure slab case we can see only two transport regimes, free-streaming at early times, followed by time-asymptotic subdiffusive transport. At very early times, free streaming within a 2D flux tube can be more rapid than in the pure slab case, causing the mean square displacement for the flux tube cases to sometimes lie above the slab case. However the temporary trapping or confinement within the flux tubes has no analog for the pure slab case, and, in this regime of time scales, particles confined by 2D flux tubes have systematically lower values of mean square perpendicular displacement.

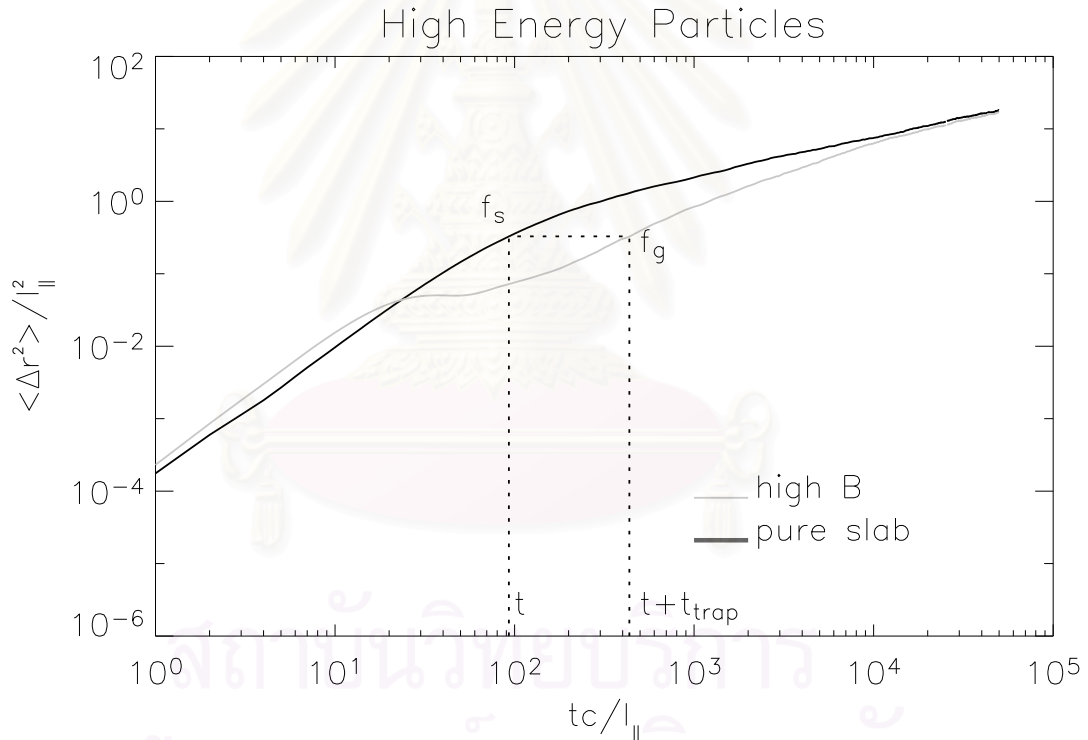


Figure 4.6: Example of high energy particle transport with slab and high magnetic fields to show $f_g(t + t_{trap})$ and $f_s(t)$.

Temporarily confined particles require a longer time to reach a specified mean square displacement than do the corresponding pure slab experiments. We define a trapping time as the difference in time required to attain a specified

perpendicular displacement.

Suppose that $f_g(t)$ and $f_s(t)$ are the mean square displacements for the Gaussian flux tube and pure slab cases respectively. It is clear that f_g must be evaluated at a later time $t + t_{trap}$ in order to attain a displacement equal to $f_s(t)$ (see f_s and f_g in Figure 4.6). We define the trapping time t_{trap} by $f_g(t+t_{trap}) = f_s(t)$, where t_{trap} is uniquely defined because both functions increase monotonically. We find a fairly stable value in most of our runs after the epoch of escape begins. Most of the delay in transport in the cases with Gaussian flux tubes is experienced during the period of trapping and suppressed diffusive escape. Here we choose the high B case to find t_{trap} , shown in Table 4.2.

Table 4.2: Trapping times

	low E	medium E	high E
Energy (MeV)	0.02	0.10	1.00
t_{trap} (units of l_{\parallel}/c)	5×10^4	9.5×10^3	3×10^3
t_{trap} (units of l_{\parallel}/v)	326	139	138

To demonstrate the temporary trapping of particles in another way, Figure 4.7 shows the spatial distribution of 5000 particles at $t = 1000l_{\parallel}/c$, where the particles started at random locations within $r = 0.1l_{\parallel}$ from the flux tube axis at $t = 0$. In the high B case, particles are clearly inhibited from leaving the flux rope (with $\sigma = 0.5$) in comparison with the pure slab case.

Thus the mechanism of field line trapping and confinement in small 2D flux tube structures, proposed as a basis for explaining dropouts (Ruffolo et al., 2003; Chuychai et al., 2005, 2007), is shown to also yield particle confinement and steep gradients.

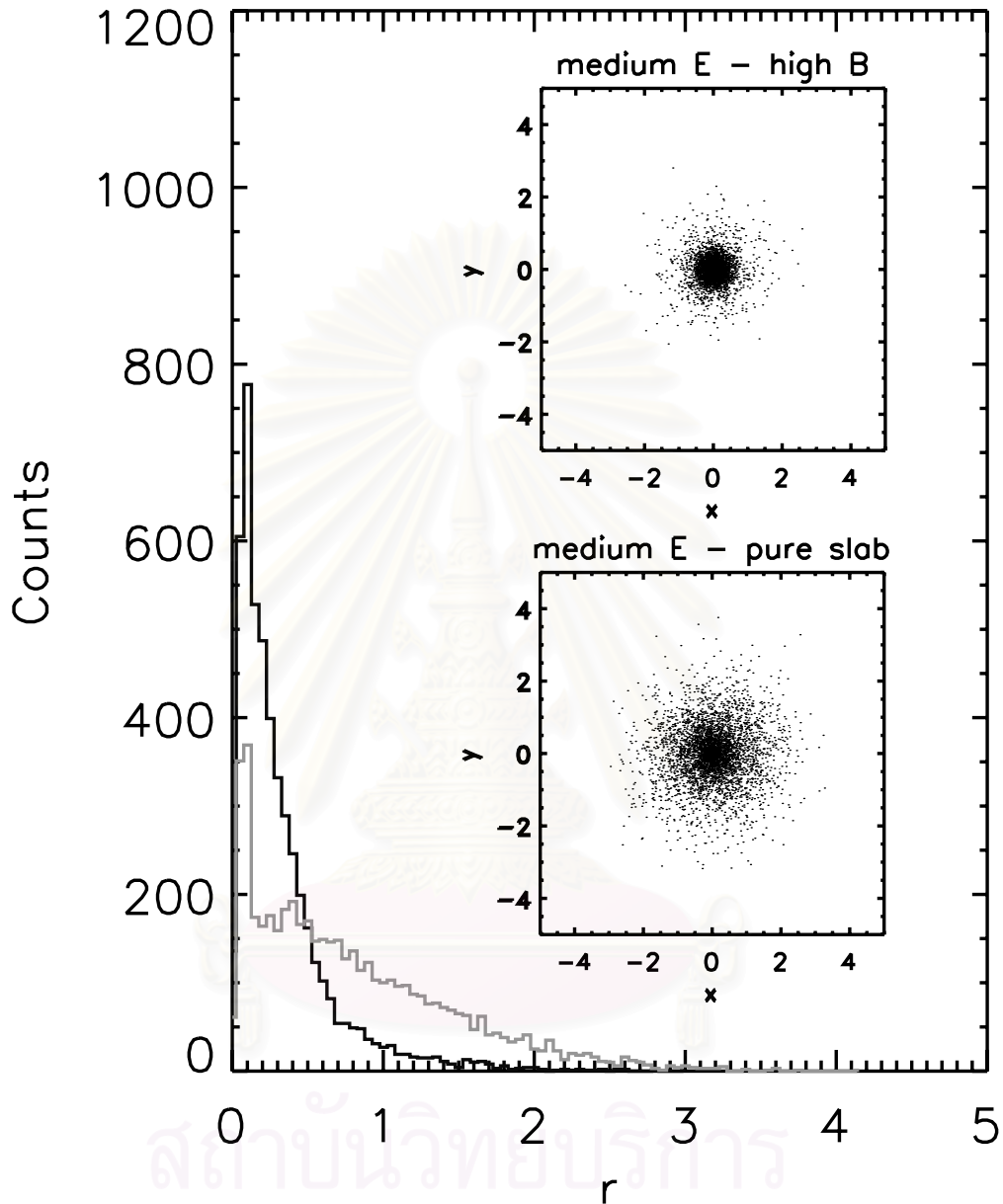


Figure 4.7: Example of how a 2D flux tube (the high B case) confines particles and leads to steep spatial gradients for an extended time (black histogram), in comparison with a case with no flux tube (pure slab; gray histogram). Distances are in units of l_{\parallel} , and r is the distance from the axis of the flux tube, which has a Gaussian potential function with $\sigma = 0.5l_{\parallel}$. Histograms show counts per $0.05 l_{\parallel}$ bin. The 5000 particles were started at $t = 0$ from random locations within $r = 0.1l_{\parallel}$ from the flux tube axis, and the histograms and scatter plots (insets) indicate their locations at $t = 1000l_{\parallel}/c$. The sharp gradients for the high B case correspond to dropout features in energetic ions and electrons from impulsive solar flares as observed near Earth.

Chapter V

Numerical Methods in Spherical Geometry

In this chapter, we will explain the numerical techniques that we used for the simulations. We have modified methods from the previous work summarized in the previous chapter (see also Ruffolo et al., 2004), and apply the methods to spherical coordinates (φ, λ, r) . We trace the paths of the particles (or field lines) in magnetic field turbulence in a spherical geometry. We simulate the 2D + slab turbulence using the Kolmogorov power spectrum (see Section 2.3). We generate the random slab field $b^{\text{slab}}(k'_z)$ in wavenumber space (k -space) and use the inverse fast Fourier transform (FFT) to convert to $b^{\text{slab}}(z')$ in real space. We then identify z' as the radius r . We generate the random potential functions $a(k'_x, k'_y)$ for 2D magnetic fluctuations, find $b^{2\text{D}}(k'_x, k'_y)$ in k' -space, and use the inverse FFT to convert to $b^{2\text{D}}(x', y')$ in real space (see Section 5.2). After that we map the slab and 2D magnetic fields to spherical geometry to obtain $\mathbf{b}(\varphi, \lambda, r)$ in terms of the longitude (φ), latitude ($\lambda = \pi/2 - \theta$), and radius r . We use these fields to trace the particle (or magnetic field line) trajectories (see Section 5.1). In the next sections, we will explain how to solve the equations of particle motion and magnetic field lines in spherical geometry and summarize the steps of the numerical simulation process (see Figure 5.7). The output of the simulations includes the positions of the particles as a function of time or perpendicular locations of magnetic field lines as a function of parallel distance. The code used here was modified from a code developed by the group of Prof. William H. Matthaeus at the Bartol Research Institute, University of Delaware.

5.1 Equations of Motion in Spherical Coordinates

We start from eqs. (3.10) and (3.11), the Newton-Lorentz equation for particle motion in a static magnetic field:

$$\frac{d}{dt}[\mathbf{v}(t)] = \frac{q}{\gamma m}[\mathbf{v}(t) \times \mathbf{B}(\mathbf{r})]. \quad (5.1)$$

The particle velocity in each component can be written in terms of (φ, λ, r) as

$$\left. \begin{aligned} v_r &= \dot{r}, \\ v_\lambda &= r \dot{\lambda}, \\ v_\varphi &= r \cos \lambda \dot{\varphi}. \end{aligned} \right\} \quad (5.2)$$

In this thesis we find the particle's equation of motion by using the Lagrangian,

$$\mathcal{L} = \frac{1}{2}m\dot{\mathbf{r}}^2 + q\dot{\mathbf{r}} \cdot \mathbf{A}(\mathbf{r}), \quad (5.3)$$

where

$$\mathbf{r} = r \hat{r}$$

$$\dot{\mathbf{r}} = \dot{r} \hat{r} + r \dot{\lambda} \hat{\lambda} + r \cos \lambda \dot{\varphi} \hat{\varphi}$$

$$(\dot{\mathbf{r}})^2 = \dot{\mathbf{r}} \cdot \dot{\mathbf{r}} = \dot{r}^2 + r^2 \dot{\lambda}^2 + r^2 \cos^2 \lambda \dot{\varphi}^2 \quad (5.4)$$

$$\mathbf{A}(\mathbf{r}) = A_r \hat{r} + A_\lambda \hat{\lambda} + A_\varphi \hat{\varphi}$$

$$\dot{\mathbf{r}} \cdot \mathbf{A}(\mathbf{r}) = \dot{r} A_r + r \dot{\lambda} A_\lambda + r \cos \lambda \dot{\varphi} A_\varphi \quad (5.5)$$

Then we get Lagrange's equations of motion:

$$\frac{\partial \mathcal{L}}{\partial q_i} - \frac{d}{dt} \frac{\partial \mathcal{L}}{\partial \dot{q}_i} = 0, \quad (5.6)$$

where $\{q_i\} = \{\varphi, \lambda, r\}$. From that, one can derive eq.(5.1) in the form (see

Appendix B)

$$\left. \begin{aligned} \frac{dv_r}{dt} = \dot{v}_r &= \frac{q}{\gamma m}(v_\varphi B_\lambda - v_\lambda B_\varphi) + \frac{v_\lambda^2}{r} + \frac{v_\varphi^2}{r}, \\ \frac{dv_\lambda}{dt} = \dot{v}_\lambda &= \frac{q}{\gamma m}(v_r B_\varphi - v_\varphi B_r) - \frac{v_\varphi^2 \tan \lambda}{r} - \frac{v_r v_\lambda}{r}, \\ \frac{dv_\varphi}{dt} = \dot{v}_\varphi &= \frac{q}{\gamma m}(v_\lambda B_r - v_r B_\lambda) - \frac{v_r v_\varphi}{r} + \frac{v_\lambda v_\varphi \tan \lambda}{r}, \end{aligned} \right\} \quad (5.7)$$

where we also need

$$\left. \begin{aligned} \dot{r} &= v_r \\ \dot{\lambda} &= \frac{v_\lambda}{r} \\ \dot{\varphi} &= \frac{v_\varphi}{r \cos \lambda} \end{aligned} \right\} \quad (5.8)$$

Next we normalized the previous equations using the speed of light (c) and parallel scale length (l_\parallel). Then we use (see Appendix A)

$$\begin{aligned} \mathbf{v}^* &= \frac{\mathbf{v}}{c} \\ t^* &= \frac{t}{\tau_c} \quad \text{and} \quad \tau_c = \frac{l_\parallel}{c} \\ \mathbf{r}^* &= \frac{\mathbf{r}}{l_\parallel} \\ \mathbf{B}^* &= \frac{\mathbf{B}}{B_0}, \end{aligned} \quad (5.9)$$

so we can rewrite eq. (5.1) as

$$\begin{aligned} \frac{d}{dt^*}[\mathbf{v}^*(t^*)] &= \frac{qB_0\tau_c}{\gamma m}[\mathbf{v}^*(t^*) \times \mathbf{B}^*(\mathbf{r}^*)] \\ &= \Omega_0\tau_c[\mathbf{v}^*(t^*) \times \mathbf{B}^*(\mathbf{r}^*)] \end{aligned} \quad (5.10)$$

$$\frac{d}{dt^*}[\mathbf{v}^*(t^*)] = \alpha_c[\mathbf{v}^*(t^*) \times \mathbf{B}^*(\mathbf{r}^*)]. \quad (5.11)$$

where $\Omega_0 = qB_0/(\gamma m)$ is the relativistic gyro-frequency at Earth and $\alpha_c = \Omega_0\tau_c$.

Then we can rewrite eq. (5.11), along with eq. (5.8), as

$$\left. \begin{aligned}
 \frac{dv_r^*}{dt^*} &= \alpha_c (v_\varphi^* B_\lambda^* - v_\lambda^* B_\varphi^*) + \frac{v_\lambda^{*2}}{r^*} + \frac{v_\varphi^{*2}}{r^*}, \\
 \frac{dv_\lambda^*}{dt^*} &= \alpha_c (v_r^* B_\varphi^* - v_\varphi^* B_r^*) - \frac{v_\varphi^{*2} \tan \lambda}{r^*} - \frac{v_r^* v_\lambda^*}{r^*}, \\
 \frac{dv_\varphi^*}{dt^*} &= \alpha_c (v_\lambda^* B_r^* - v_r^* B_\lambda^*) - \frac{v_r^* v_\varphi^*}{r^*} + \frac{v_\lambda^* v_\varphi^* \tan \lambda}{r^*}, \\
 \frac{dr^*}{dt^*} &= v_r, \\
 \frac{d\lambda}{dt^*} &= \frac{v_\lambda}{r}, \\
 \frac{d\varphi}{dt^*} &= \frac{v_\varphi}{r \cos \lambda}.
 \end{aligned} \right\} \quad (5.12)$$

For numerical simulations, we use eq. (5.12) as the equations of motion of particles. Here r^* , λ , and φ are the coordinates of the particles and v_r^* , v_λ^* , and v_φ^* are the velocity components of the particles.

We use a numerical method to solve this equation by using the fourth Runge-Kutta method with adaptive stepsize control. In Figures 5.1 - 5.4, we test the accuracy of our program by finding the gyro-frequency at about 1 AU for 1 MeV, 10 MeV, 100 MeV, and 1 GeV particles in a radial magnetic field, $B_r \propto 1/r^2$, for which the particle trajectory follows the surface of a cone. The field is set to 5 nT at 1 AU. The theory defines the gyro-frequency as $\omega = qB/(\gamma m)$, and the gyro-frequency will be constant if the magnetic field is constant. For this case, over a small region near 1 AU the particles should have gyro-frequencies of about 0.478, 0.474, 0.433, and 0.232 radians per second at 1 AU, and from the simulations, we get 0.476, 0.470, 0.431, and 0.226 radians per second, respectively, for the 4 energy values.

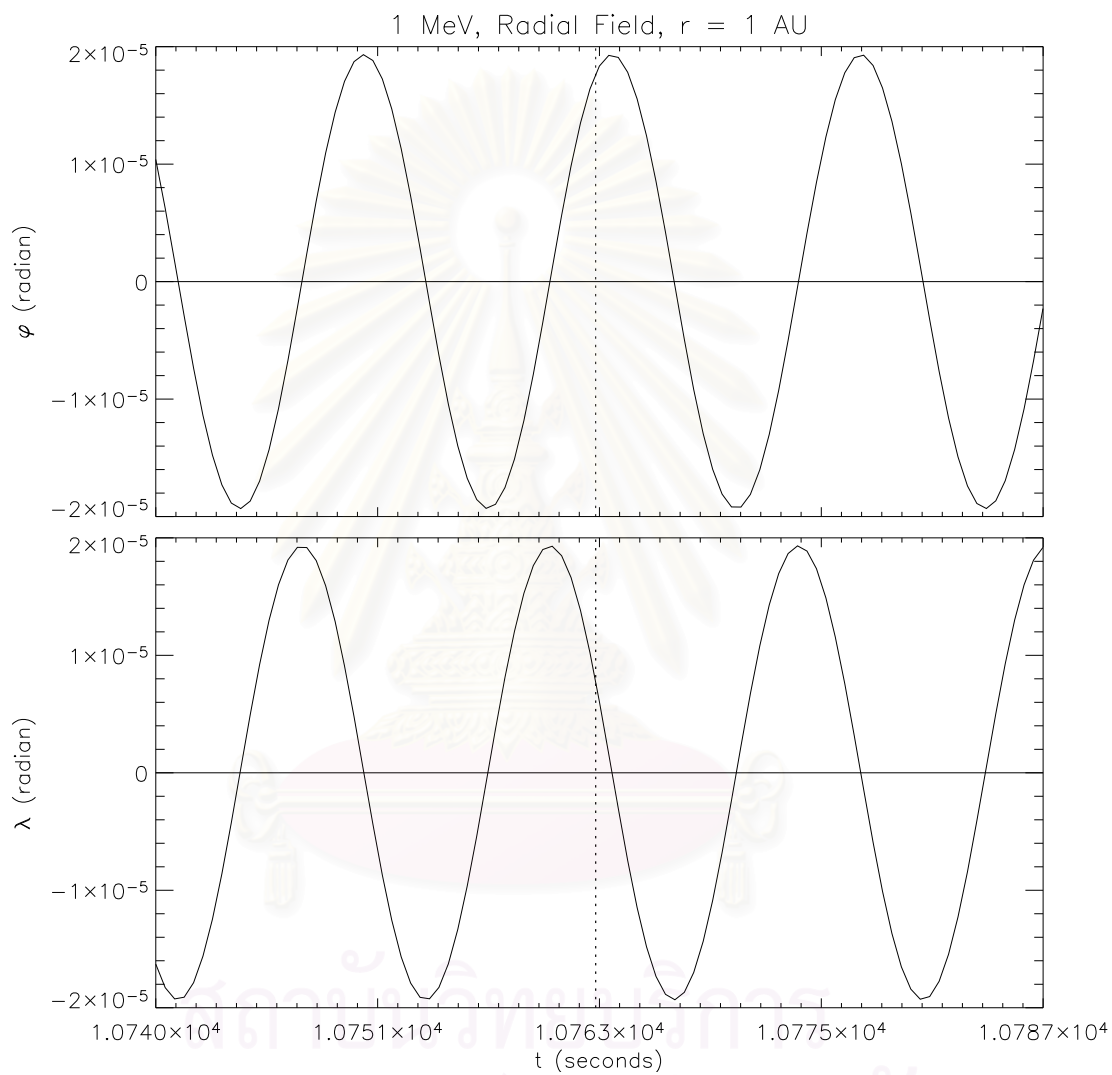


Figure 5.1: Upper panel: φ vs. time. Lower panel: λ vs. time. The magnetic field is a radial field. The simulations successfully follow the correct gyro-frequency for a 1 MeV particle.

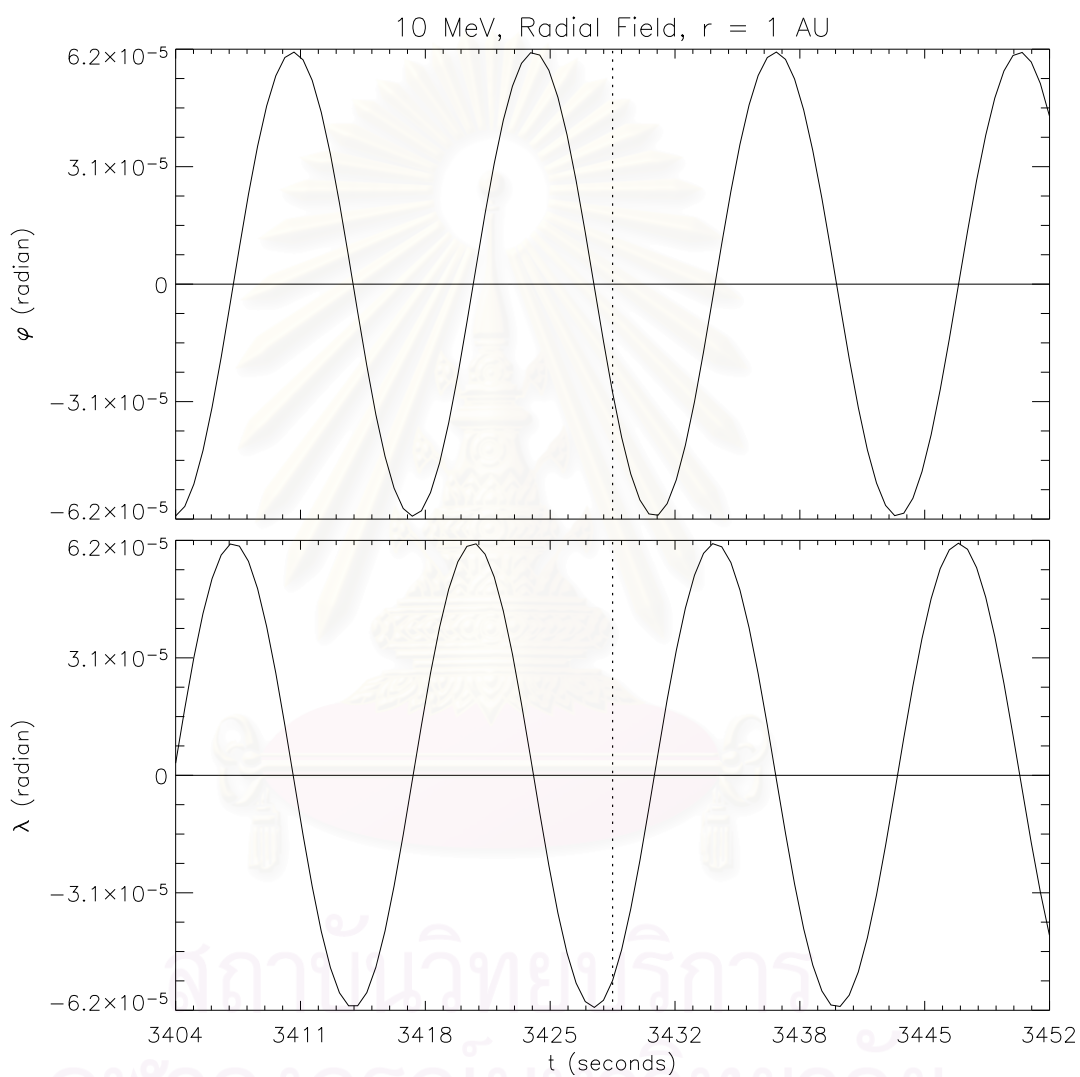


Figure 5.2: Like Figure 5.1, for a 10 MeV particle.

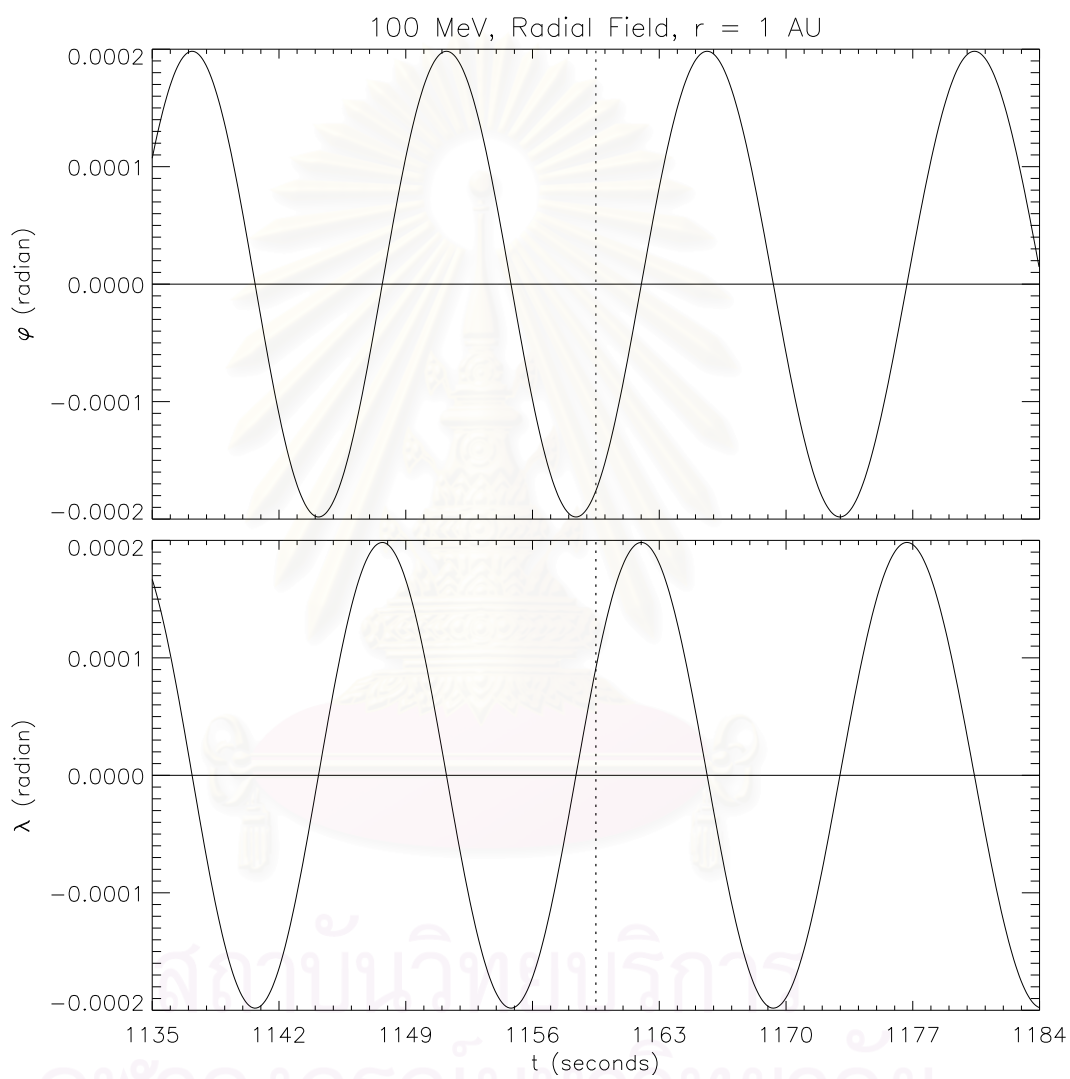


Figure 5.3: Like Figure 5.1, for a 100 MeV particle.

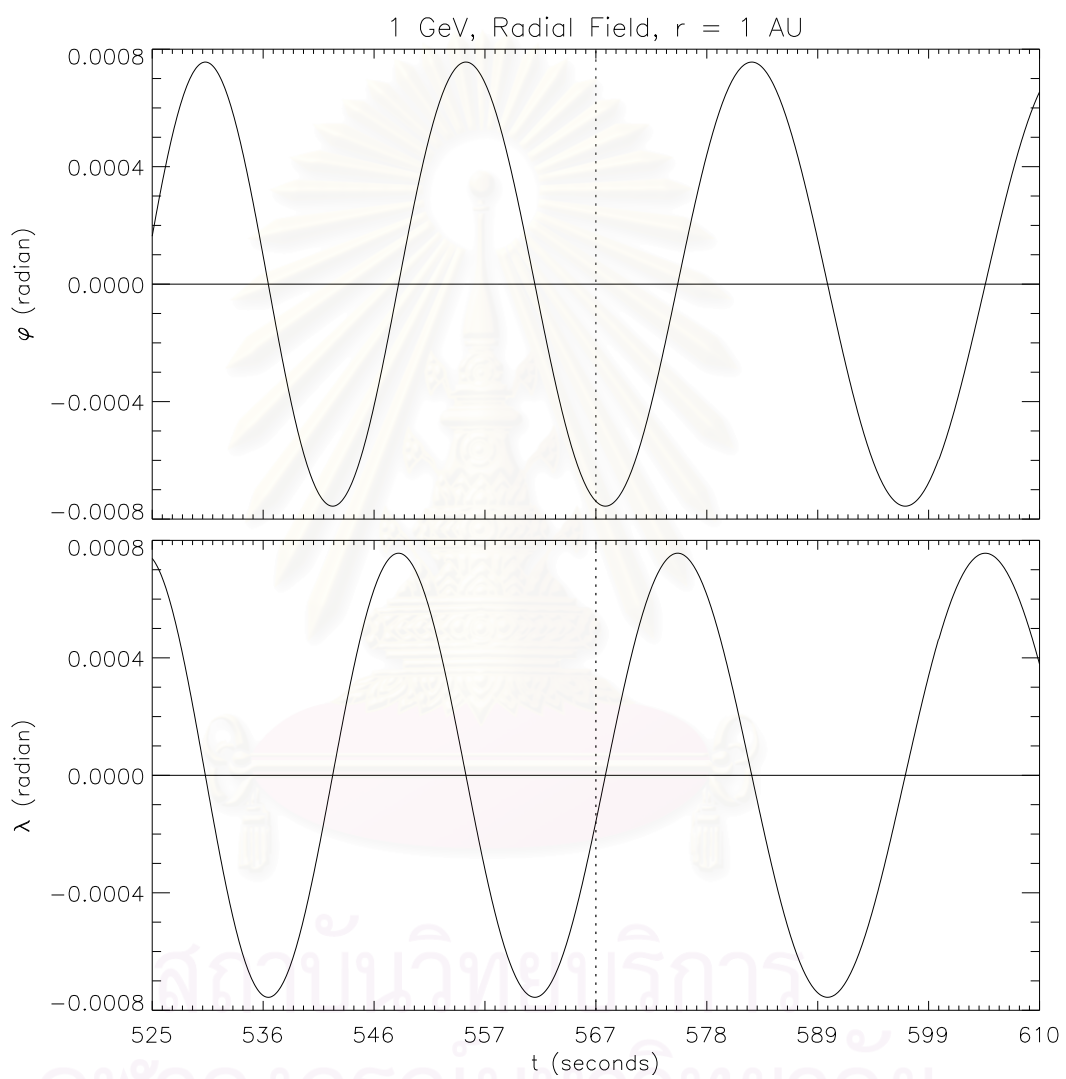


Figure 5.4: Like Figure 5.1, for a 1 GeV particle.

5.2 Generating 2D + Slab Magnetic Fields in a Spherical Geometry

For this work, we generated the turbulent magnetic field in two physically distinct geometries, Cartesian geometry (where we set $\mathbf{B}_0 = B_0\hat{z}$) and spherical geometry (where we set $\mathbf{B}_0 = B_0\hat{r}$). For Cartesian geometry, we generated the 2D field as a Gaussian function which show the results in Chapter IV. For spherical geometry, we generated the 2D + slab magnetic field more realistically by using the magnetic field as

$$\mathbf{B} = \mathbf{B}_1(r) + \mathbf{b}(\varphi, \lambda, r), \quad (5.13)$$

where $\mathbf{B}_1 = \frac{r_1^2 B_0}{r^2} \hat{r}$, \mathbf{B}_1 is the magnetic field in the r direction at 1 AU, and r_1 is the reference radius of the simulation. The transverse fluctuation $\mathbf{b}(\varphi, \lambda, r)$ is separated into two components:

$$\mathbf{b}(\varphi, \lambda, r) = \mathbf{b}^{\text{slab}}(r) + \mathbf{b}^{2\text{D}}(\varphi, \lambda, r) = \frac{r_1^2}{r^2} \mathbf{b}_1^{\text{slab}}(r) + \frac{r_1^2}{r^2} \mathbf{b}_1^{2\text{D}}(\varphi, \lambda), \quad (5.14)$$

where the fluctuation $\mathbf{b}_1^{\text{slab}}$ depends only on r , the radial distance from the Sun, and $\mathbf{b}_1^{2\text{D}}$ for the 2D turbulence depends only on the perpendicular coordinates for longitude, φ , and latitude, λ . For the 2D component, we can write

$$\mathbf{b}^{2\text{D}}(\varphi, \lambda, r) = \nabla \times [a(\varphi, \lambda, r)\hat{r}] \quad (5.15)$$

$$\mathbf{b}_1^{2\text{D}}(\varphi, \lambda) = \nabla \times [a_1(\varphi, \lambda)\hat{r}] \quad \text{at} \quad r = r_1 \quad (5.16)$$

$$a(\varphi, \lambda, r) = \frac{r_1}{r} a_1(\varphi, \lambda), \quad (5.17)$$

where $a(\varphi, \lambda, r)\hat{r}$ is a vector potential for the 2D component, and $a_1(\varphi, \lambda)$ can be called the potential function.

To generate the fluctuating parts, we start from the Kolmogorov power spectrum of turbulence in k -space. For the slab case we use eq. (2.7) in Section

2.3 (Ruffolo et al., 2003), but we use primed coordinates to distinguish these from the Cartesian coordinates:

$$P_{xx}^{slab}(k'_z) = P_{yy}^{slab}(k'_z) = \frac{C^{slab}}{\left[1 + (k'_z l_{\parallel})^2\right]^{5/6}},$$

where C^{slab} is a normalization constant and l_{\parallel} is a parallel coherence length. Then we use an inverse fast Fourier transform to obtain the fluctuating magnetic fields in real space, where we map z' onto the radius r .

For the 2D magnetic field model, we want to generate $a(k'_x, k'_y)$ and find the magnetic field $b^{2D}(k'_x, k'_y) = -i\mathbf{k}' \times [a(k'_x, k'_y)\hat{z}]$. Then the 2D potential function is $a(x', y')$, and we have (Ruffolo et al., 2004)

$$P_{xx}^{2D}(k'_x, k'_y) = k_y'^2 A(k'_{\perp}) \quad \text{and} \quad P_{yy}^{2D}(k'_x, k'_y) = k_x'^2 A(k'_{\perp}), \quad (5.18)$$

where $A(k'_{\perp})$ is the axisymmetric power spectrum of $a(x', y')$, defined as the Fourier transform of the correlation function $\langle a(0, 0)a(x', y') \rangle$, and k'_{\perp} is the 2D wavenumber magnitude defined as $k'_{\perp} \equiv \sqrt{k_x'^2 + k_y'^2}$. The eddies in the Kolmogorov theory (see Section 2.2) will include motion in all directions, so we must consider the energy density as a function of k'_{\perp} in each direction. We sum $P_{xx}(k'_x, k'_y)$ and $P_{yy}(k'_x, k'_y)$, at a magnitude of k'_{\perp} by integrating over a circle of radius k'_{\perp} and width dk'_{\perp} in the radial direction. Then the energy density will depend only on the magnitude of k'_{\perp} , then called the ‘‘omnidirectional power spectrum’’ (OPS). The OPS is proportional to $k'_{\perp}(P_{xx}^{2D} + P_{yy}^{2D}) = k'_{\perp}{}^3 A(k'_{\perp})$. Thus we use a Kolmogorov law for the inertial range of turbulence with the OPS varying as $k^{-5/3}$. Then

$$k'_{\perp}{}^3 A(k'_{\perp}) \propto k'_{\perp}{}^3 |a(k'_{\perp})|^2 \propto k'_{\perp}{}^{-5/3}, \quad (5.19)$$

and we get

$$A(k'_{\perp}) \propto k'_{\perp}{}^{-14/3}. \quad (5.20)$$

To match eq. (5.20) in the inertial range with $A \sim \text{constant}$ for low k'_\perp , we can generate a 2D power spectrum as

$$A(k'_\perp) = \frac{C^{2D}}{[1 + (k'_\perp l_\perp)^2]^{7/3}}, \quad (5.21)$$

where C^{2D} is a normalization constant, and l_\perp is a characteristic length scale. After that we use a two-dimensional inverse Fourier transform to find $a(x', y')$. We then map the potential function a_1 of two Cartesian coordinates, x' , and y' , onto the longitude, $\varphi = x'/r_1$, and latitude, $\lambda = y'/r_1$, respectively.

5.3 Tracing Magnetic Field Lines in Spherical Geometry

The field line trajectories are found by solving the same equation as in Cartesian geometry,

$$d\mathbf{l} \times \mathbf{B} = 0,$$

but we now solve this in spherical geometry by using

$$d\mathbf{l} = r \cos \lambda d\varphi \hat{\varphi} + r d\lambda \hat{\lambda} + r \hat{r},$$

and

$$\mathbf{B} = b_\varphi \hat{\varphi} + b_\lambda \hat{\lambda} + B_r \hat{r}.$$

Then we get

$$\begin{aligned} 0 &= \begin{vmatrix} \hat{\varphi} & \hat{\lambda} & \hat{r} \\ r \cos \lambda d\varphi & r d\lambda & dr \\ B_\varphi & B_\lambda & B_r \end{vmatrix} \\ 0 &= (r d\lambda B_r - b_\lambda dr) \hat{\varphi} + (b_\varphi dr - r \cos \lambda d\varphi B_r) \hat{\lambda} \\ &\quad + (r \cos \lambda d\varphi b_\lambda - b_\varphi r d\lambda) \hat{r}. \end{aligned}$$

The solution of this equation is

$$\frac{dr}{B_r} = \frac{r \cos \lambda d\varphi}{B_\varphi} = \frac{r d\lambda}{B_\lambda}, \quad (5.22)$$

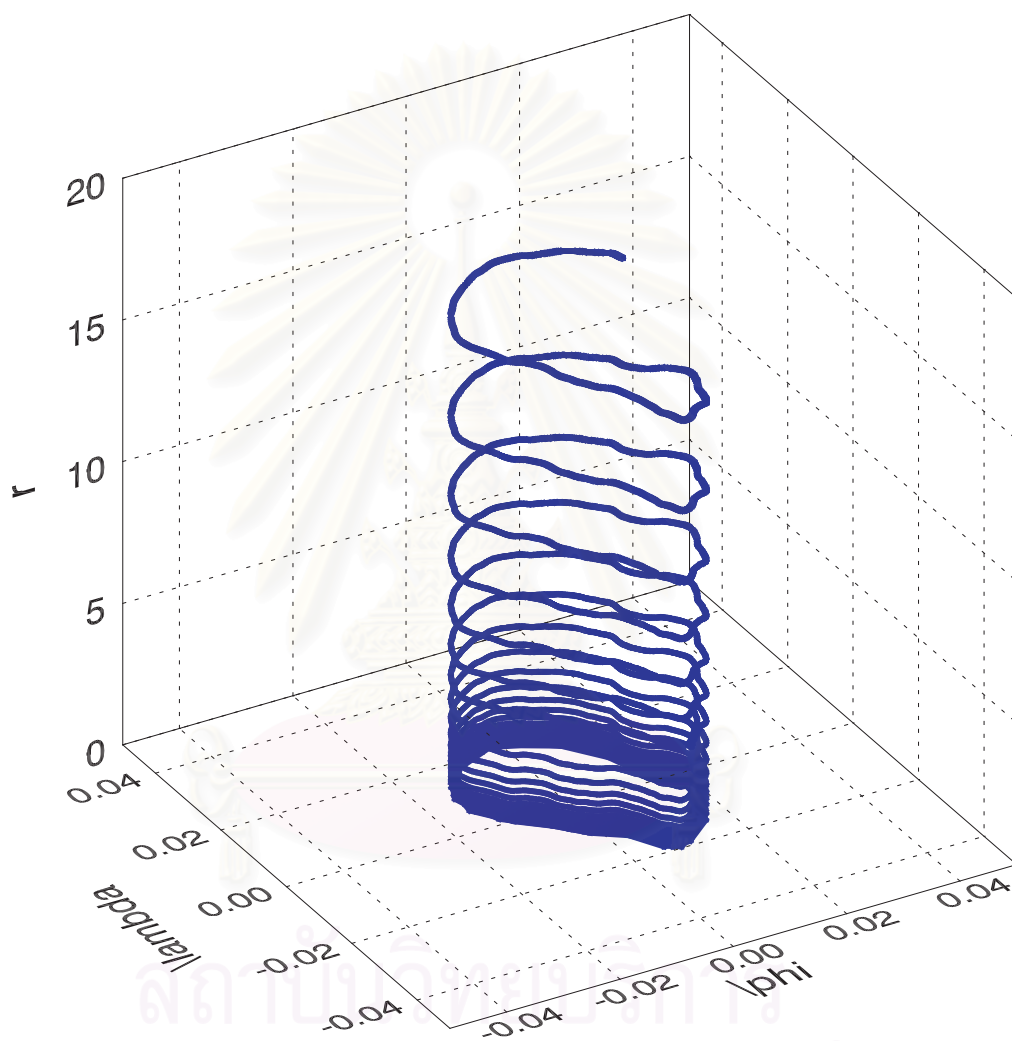


Figure 5.5: Example of the trajectory of a magnetic field line in spherical coordinates.

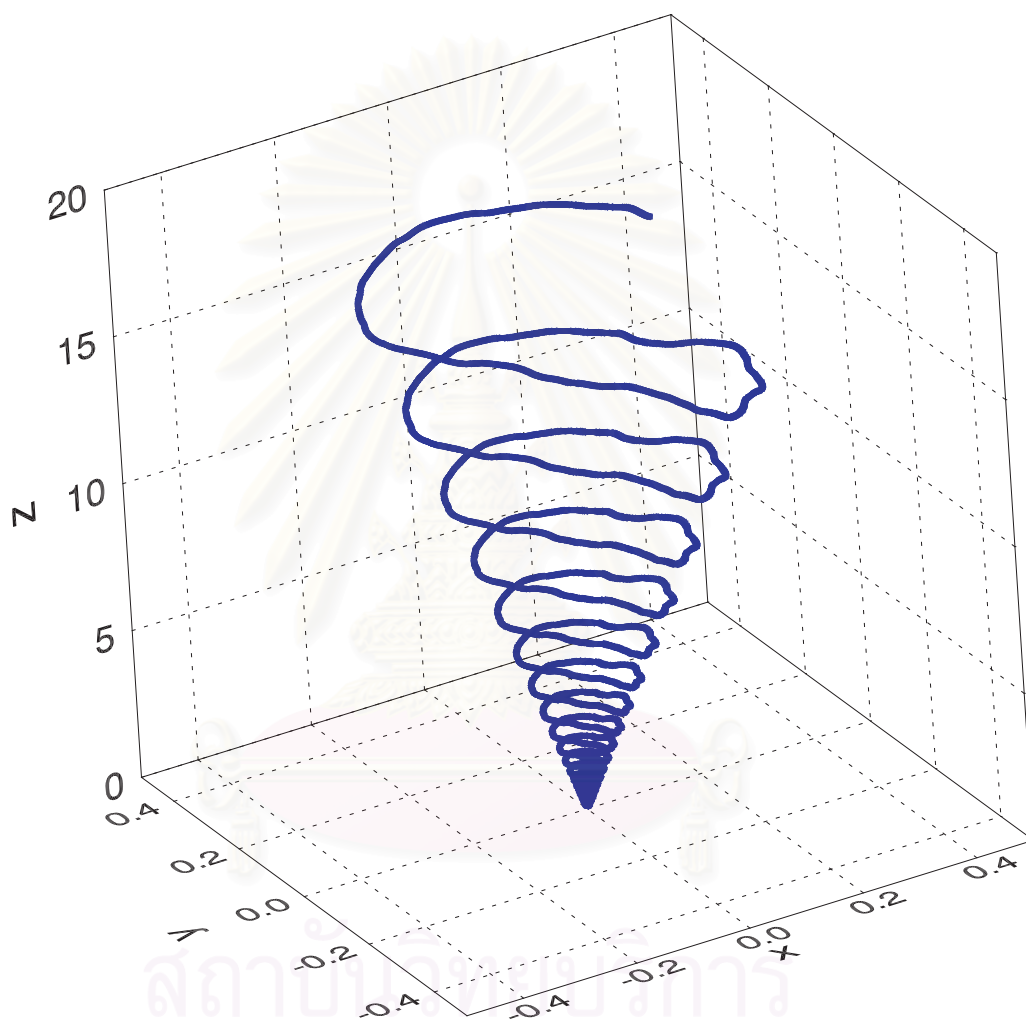


Figure 5.6: Example of the trajectory of the same magnetic field line as in Figure 5.5, transformed to Cartesian coordinates in units of AU.

where B_φ , B_λ , and B_r are the magnetic field components in the (φ, λ, r) directions.

Figures 5.5 - 5.6 are examples of the same magnetic field line trajectory in spherical and Cartesian coordinates.

5.4 Summary of Our Simulations

From the previous sections, we use the fourth order Runge-Kutta method with adaptive stepsize control to solve eqs. (5.12) or (5.22). We are programming in Fortran 77 and run MPI codes for parallel programming on clusters of computers. We can summarize the steps in our simulations as shown in Figure 5.7.



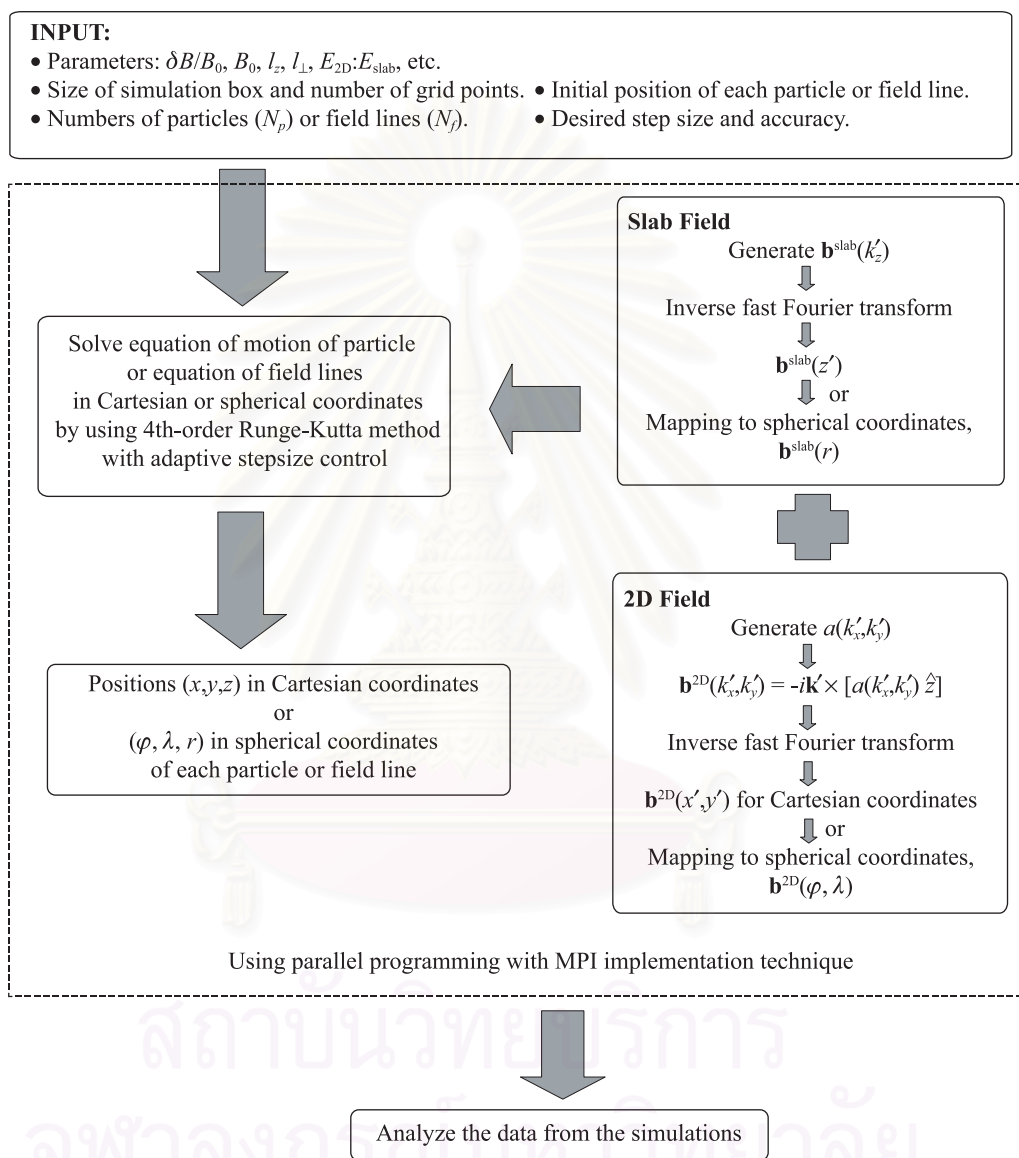


Figure 5.7: Diagram of steps in the field line or particle simulations.

Chapter VI

Results of Simulations of Turbulent Magnetic Fields and Particle Transport in Spherical Geometry

Here we are interested to simulate the magnetic field line and particle trajectories in spherical geometry. In nature, the interplanetary magnetic field between the Earth and the Sun has a Parker spiral shape (Parker, 1958) as shown in Figure 2.4. We can neglect the spiral curvature between the Sun and Earth and assume a radial field, $B = (B_0/r^2)\hat{r}$, for reasons explained below. The spiral curvature would be more important outward from the Earth. We simulate the turbulent magnetic fields and particle motions in a spherical geometry, which is more realistic than Cartesian geometry but less realistic than a spiral field.

We know that the magnetic field will basically decrease as a function of r^2 from the Sun. The magnitude of the magnetic field near the source is strong and reduces with distance, which we can call a “focusing magnetic field”. Focusing is the process where the pitch angle (θ), the angle between the particle motion direction and the magnetic field, changes with time, so the particle pitch angle tends to zero (moving directly along the magnetic field). The rate of change of the cosine of the pitch angle (μ) due to focusing is

$$\frac{d\mu}{dt} = \frac{v}{2L(z)}(1 - \mu^2), \quad (6.1)$$

where $\mu = \cos \theta$, v is the particle velocity, and L is the focusing length defined by

$$\frac{dB}{dz} = -\frac{B}{L}. \quad (6.2)$$

Here we map z onto r , so

$$\frac{1}{L} = -\frac{1}{B} \frac{dB}{dz} = -\frac{1}{B} \frac{dB}{dr} = \frac{2}{r}. \quad (6.3)$$

For the interplanetary transport of solar energetic particles, there is very strong focusing that makes the particles reach a pitch-angle equilibrium very quickly (within ~ 0.01 AU) to form a coherent pulse with nearly maximal anisotropy and highly collimated motion along the magnetic field (Ruffolo and Khumlumert, 1995). Since the focusing is most important near the Sun where the spiral field is much like a radial field, we can safely assume a spherical geometry. However, we cannot see this focusing effect in a Cartesian geometry. This is our key motivation for using a more realistic spherical geometry.

In this section, we use the 2D + slab turbulence model as defined in Sections 2.5 and 3.2:

$$\begin{aligned} \mathbf{B}(\varphi, \lambda, r) &= \mathbf{b}^{\text{slab}}(r) + \mathbf{b}^{2\text{D}}(\varphi, \lambda, r) + B_0(r)\hat{r}, \\ &= \mathbf{b}^{\text{slab}}(r) + \mathbf{b}^{2\text{D}}(\varphi, \lambda, r) + \frac{r_1^2 B_1}{r^2} \hat{r}, \end{aligned} \quad (6.4)$$

where r_1 is the reference radius, which we set to 1 AU.

For the slab fluctuation model, we start from the Kolmogorov power spectrum of turbulence in k' -space. We can write

$$P_{xx}^{\text{slab}}(k'_z) = P_{yy}^{\text{slab}}(k'_z) \propto \frac{1}{[1 + (k'_z l_{\parallel})^2]^{5/6}},$$

where l_{\parallel} is a parallel coherence length. Then we use the inverse fast Fourier transform (FFT) to obtain the fluctuating magnetic fields in real space, and map the magnetic field from the z' -direction to the r -direction.

For the 2D model, we generate the potential function $a_1(k'_x, k'_y)$ in k -space with a random phase at each point in discrete Fourier transform for the power spectrum $|a_1^2| = A(k'_\perp)$, where $k'_\perp \equiv \sqrt{k'^2_x + k'^2_y}$, and then use the inverse FFT to real space as for the slab model. After that we map $a_1(x', y')$ to the longitude, $\varphi = x'/r_1$, and latitude $\lambda = \pi/2 - \theta = y'/r_1$, to get $a_1(\varphi, \lambda)$ (see Figure 6.1). The fluctuation amplitude is normalized to yield the desired value of $\langle b^2 \rangle$ for the simulated field.

For the numerical simulations, we set the box length in the r direction as 10,000 in units of the parallel coherence scale. The lengths in the φ and λ directions are angles of 50 degrees \times 50 degrees. The number of grid points is a power of 2 for the Fourier transform, with $N_r = 4,194,304$, $N_\varphi = 2,048$, and $N_\lambda = 2,048$. We set $B_1 = 1$, the ratio of the root-mean-squared fluctuating field is $\delta b/B_0 = 0.5$, and the ratio of 2D energy to slab energy is $E_{2D}:E_{\text{slab}} = 80 : 20$. We start 10,000 magnetic field lines and particles in a circle with a radius of 10 degrees.

Figure 6.2 shows scatter plots of the magnetic field line locations in (φ, λ) , integrated over all arrival times. At $r = 0.1$ AU (upper left corner), the initial positions were at random locations in a circle of 10 degree radius corresponding to the injection region of solar energetic particles. The true radius of the injection region is not well known; the magnetic connection at Earth orbit extends to $\sim 25^\circ$ (Reames, 1992) but that may be largely due to the field line random walk. We start at $r = 0.1$ to avoid the numerical problem of division by zero and the step size and grid must be low enough for plotting or analysis. We trace the field lines from these initial locations as a function of r .

The other panels are the cross-sectional scatter plots at longer distance along the mean magnetic field, again integrating over the arrival time, which show the field line structures in the distribution of the charged test particles.

The scatter plots of the field lines show that the field lines near O-points were still trapped by the small-scale topology, with a high density, while the field lines outside the 2D island move to other regions to spread quickly to large angular distances with low density. This explains that the filamentary distribution of field lines is trapped corresponding to Figure 2.10 (Ruffolo et al., 2003), as indicated by the dropout features. Some field lines move to another O-point and are trapped inside as part of the random walk of field lines.

In the last panel, for $r = 2$ AU, many magnetic field lines are still trapped in 2D structures (islands). However, overall much lateral spreading has occurred. This spreading is starting to wash out the dropout features. Our results qualitatively correspond with the results of McKibben et al. (2001), who observed the SEPs from the Ulysses spacecraft while coming inwards from ~ 2.8 to ~ 1.9 AU on the opposite side of the Sun from Earth. By comparing with data from the IMP-8 spacecraft near Earth, they determined that the SEPs spread over $\sim 90^\circ$ in angular distance after a few days.

Figures 6.3 - 6.7 show scatter plots of the particle locations for energies of 1 MeV, 10 MeV, 100 MeV, 1 GeV, and 10 GeV, respectively, for the same magnetic profile. The properties of the particles are shown in Table 6.1. For these simulations, each particle begins at the same point as a magnetic field line, and we inject the particles parallel to the magnetic field direction at the initial radius of 0.1 AU. This represents the collimation that results from intense focusing within 0.1 AU of the Sun (Ruffolo and Khumlumlert, 1995). Then we can say that at a given radius, these plots are quite similar to the scatter plots of magnetic field lines in a Cartesian geometry (Ruffolo et al., 2003).

Compared with Figure 6.2, at 1 AU, the scatter plots of particles with various energies match quite closely with the scatter plots of magnetic field lines. That means the particles of < 1 GeV follow the field lines very closely,

so “dropout” patterns can be modeled by the field line tracing (in spherical geometry) as well as particle tracing. From the ACE observations, the size of the dropout structures is about 0.03 AU. Then we predict that if the Larmor radius of the particles is more than half of the size of dropout features, which occurs at an energy of about ~ 3 GeV, we should see the dropout features less clearly. Figure 6.7 shows scatter plots of 10 GeV particles, where we indeed see the dropouts less clearly at 1 AU.

Figures 6.8 - 6.12 and 6.13 - 6.17 show the scatter plots of the particles in φ vs. r and λ vs. r , respectively. Each panel shows the particle locations after traveling a distance $s = vt$, where v is the particle speed and t is the time over which the particle moved. Then s can replace the time. The upper left panels show the initial positions of the particle over a radius of 10 degrees. The panels at $s = 0.15, 0.25$, and 0.5 AU show that some particles moved up to these distances, implying motion with a pitch angle of nearly zero, and some particles were scattered or trapped and therefore were found at $r < s$. At $s > 0.5$, most of the particles were scattered in the magnetic field, making the particle distribution spread in the r direction. We also can see the angular spread increase with increasing distance r from the Sun. The scatter plots of λ vs. r in Figures 6.13 - 6.17 look denser than the scatter plots of φ vs. r in Figures 6.8 - 6.12 only in this realization of 2D turbulence. For other realizations, these scatter plots will have different spreading.

Contour and Scatter Plots of 2D+Slab Field for $\delta b/B_0 = 0.50$

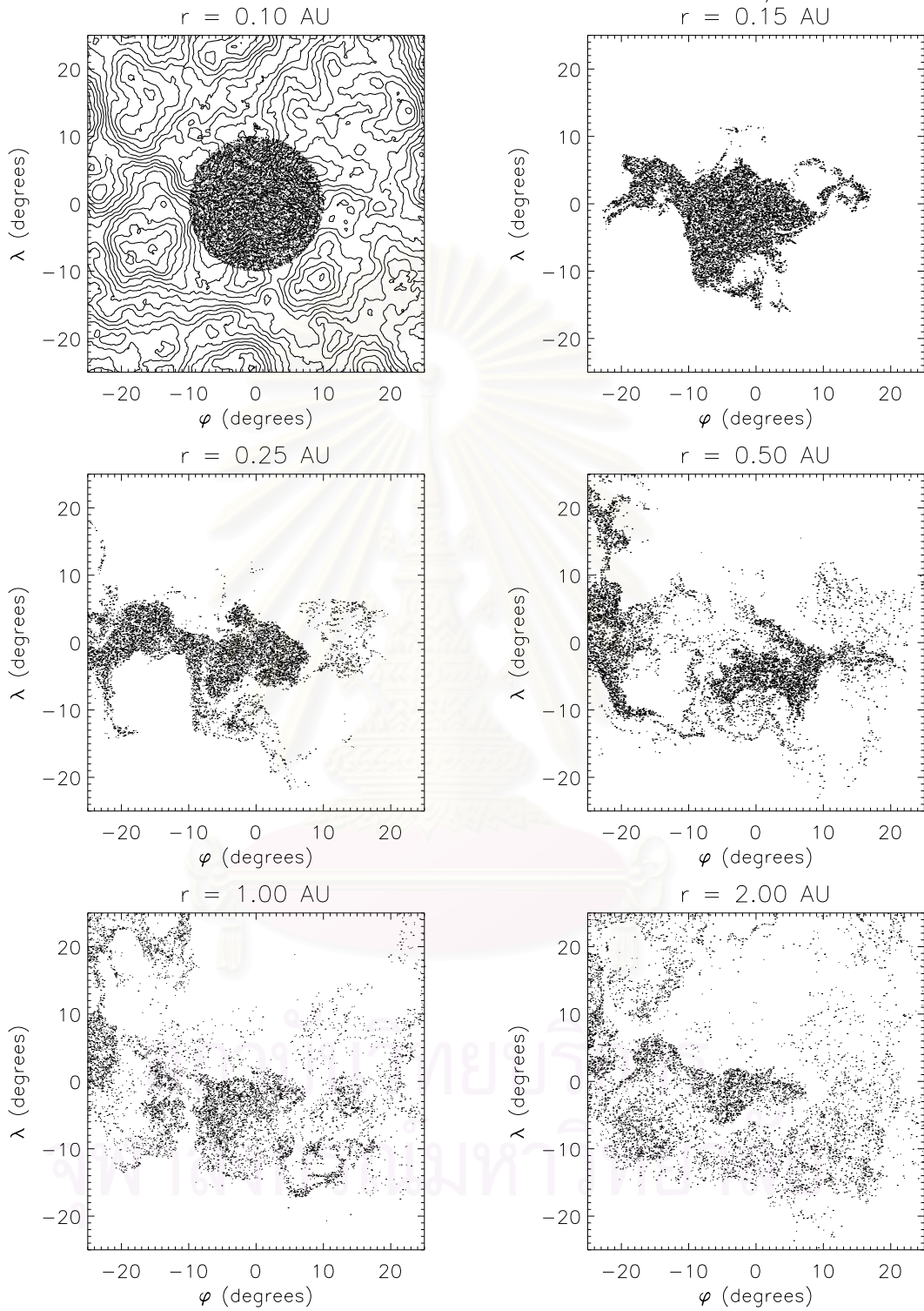


Figure 6.2: Scatter plots of magnetic field lines at $r = 0.1, 0.15, 0.25, 0.5, 1,$ and 2 AU. Lines are contours of constant $a(\varphi, \lambda)$.

Contour and Scatter Plots for $\delta b/B_0 = 0.50$, $E = 1.00$ MeV

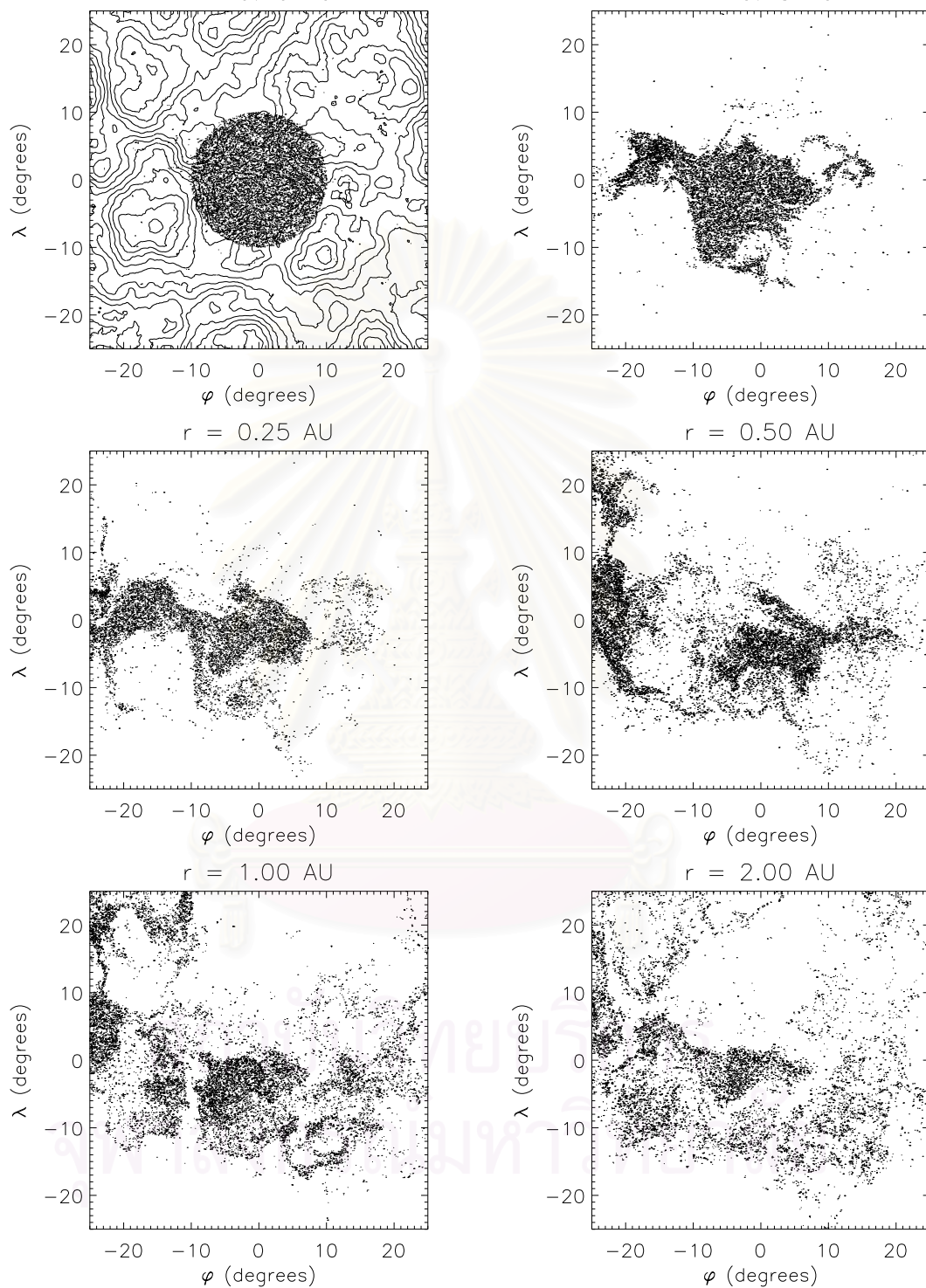


Figure 6.3: Scatter plots for a particle energy of 1 MeV at $r = 0.1, 0.15, 0.25, 0.5, 1,$ and 2 AU.

Contour and Scatter Plots for $\delta b/B_0 = 0.50$, $E = 10.00$ MeV

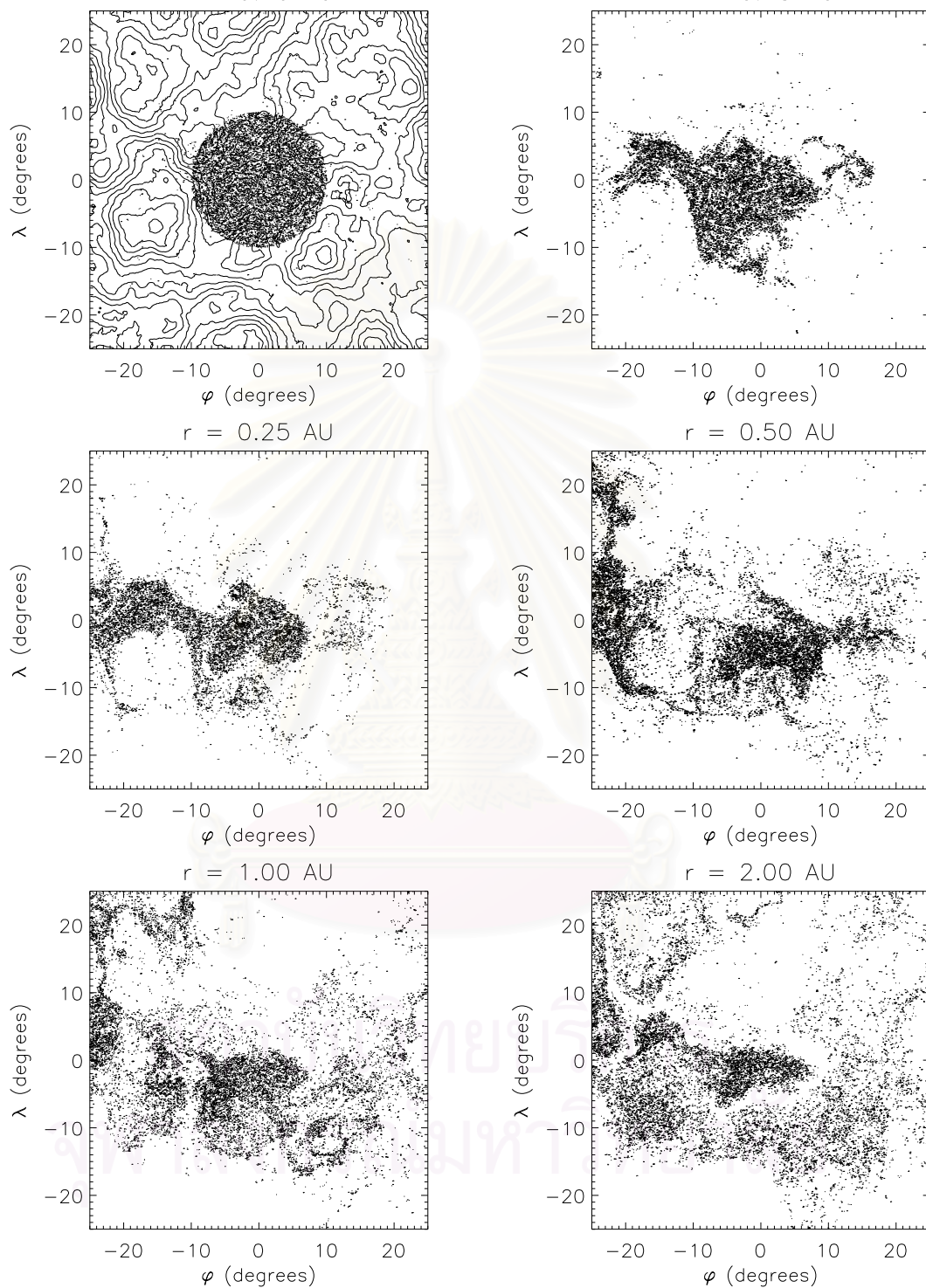


Figure 6.4: Scatter plots for a particle energy of 10 MeV at $r = 0.1, 0.15, 0.25, 0.5, 1,$ and 2 AU.

Contour and Scatter Plots for $\delta b/B_0 = 0.50$, $E = 100.00$ MeV

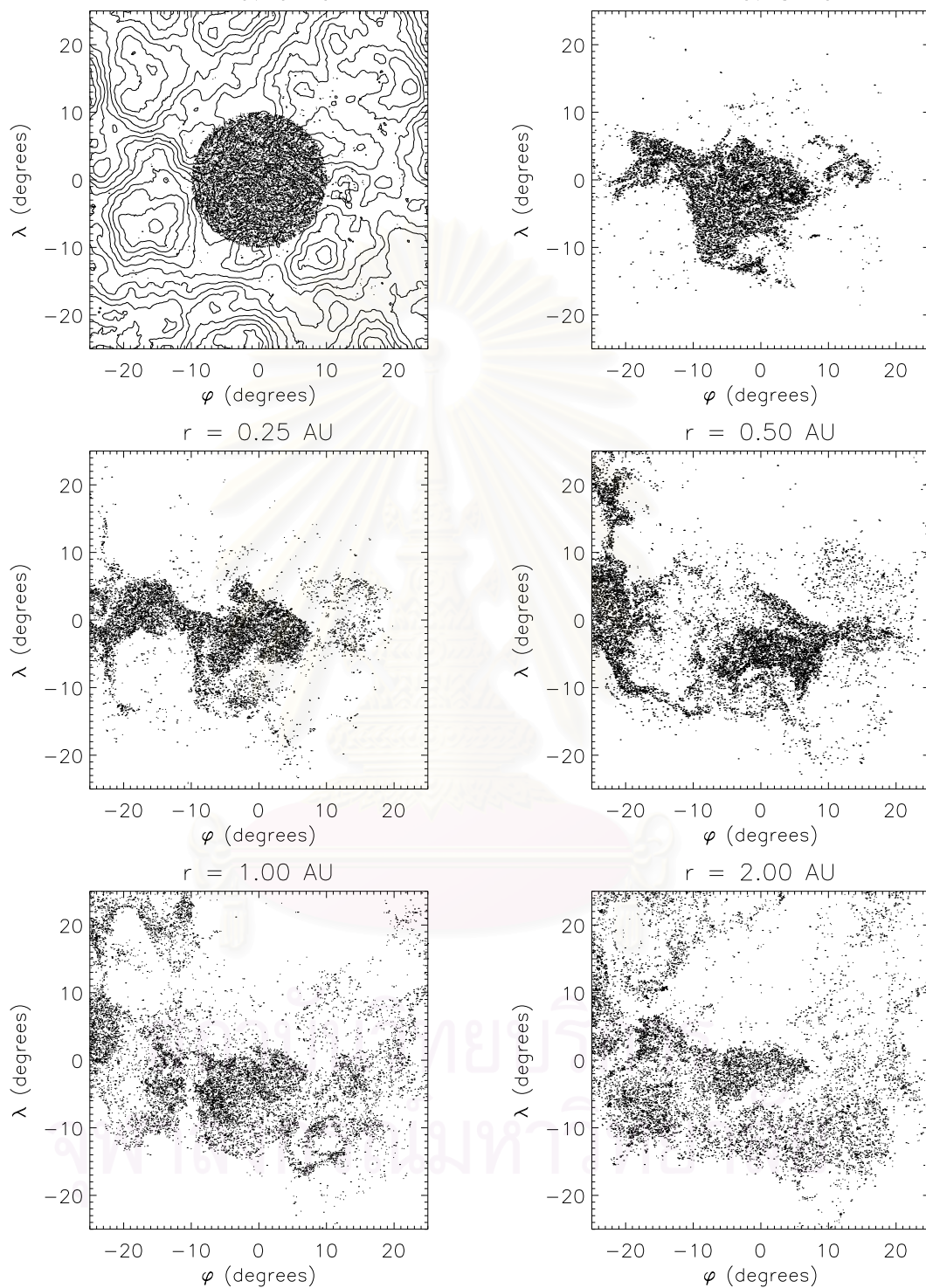


Figure 6.5: Scatter plots for a particle energy of 100 MeV at $r = 0.1, 0.15, 0.25, 0.5, 1,$ and 2 AU.

Contour and Scatter Plots for $\delta b/B_0 = 0.50$, $E = 1.00$ GeV

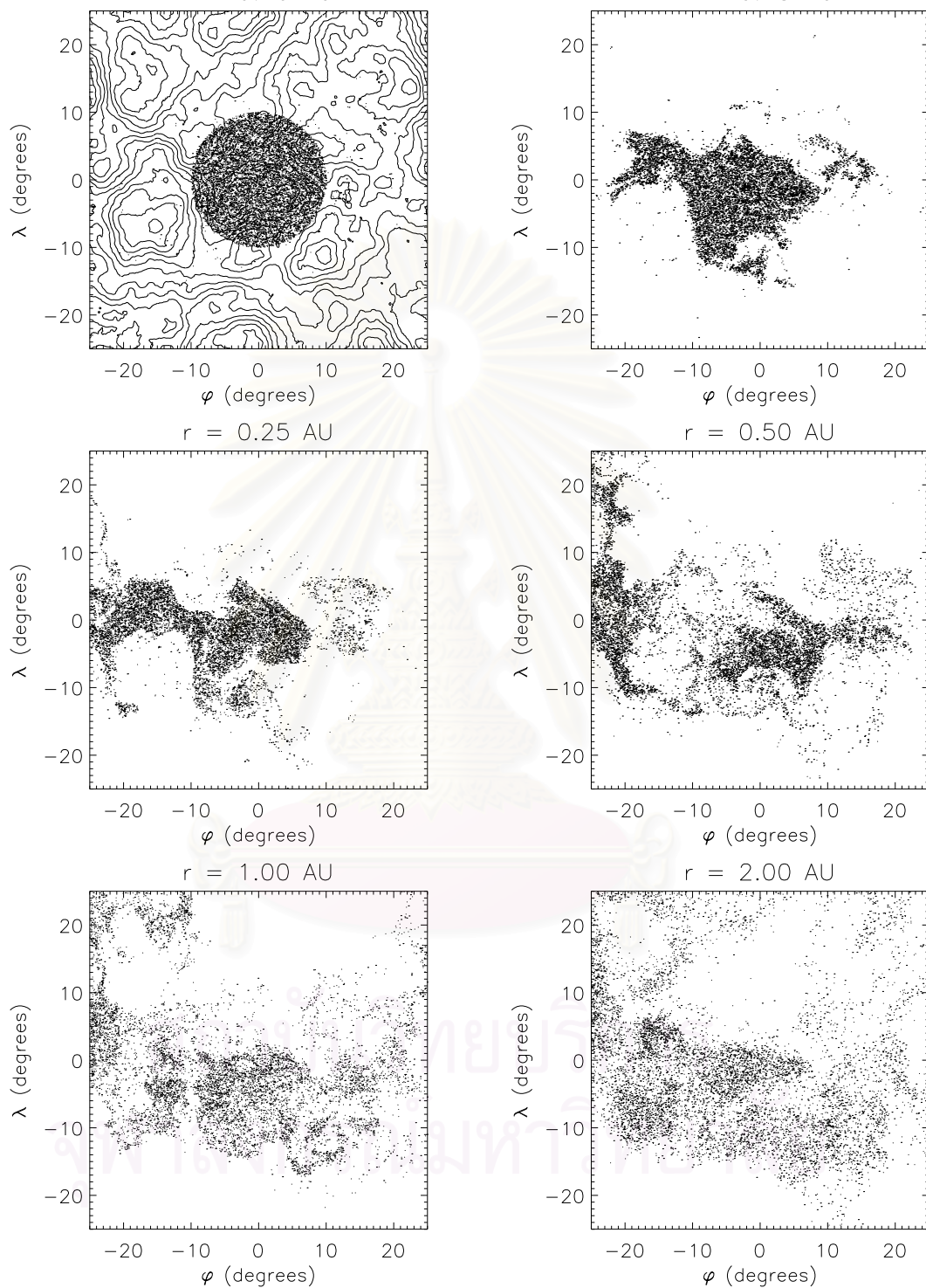


Figure 6.6: Scatter plots for a particle energy of 1 GeV at $r = 0.1, 0.15, 0.25, 0.5, 1, \text{ and } 2$ AU.

Contour and Scatter Plots for $\delta b/B_0 = 0.50$, $E = 10.00$ GeV

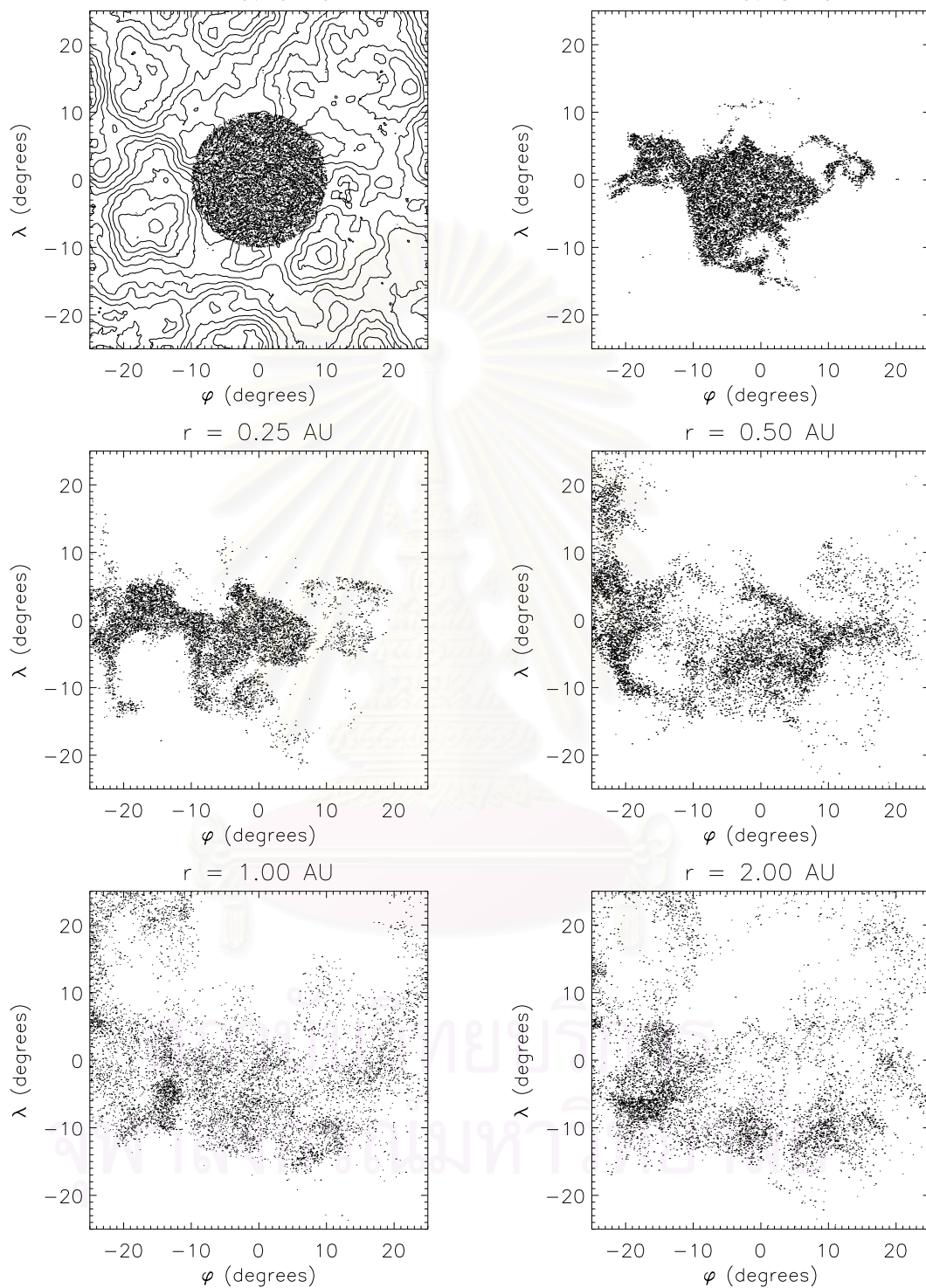


Figure 6.7: Scatter plots for a particle energy of 10 GeV at $r = 0.1, 0.15, 0.25, 0.5, 1,$ and 2 AU.

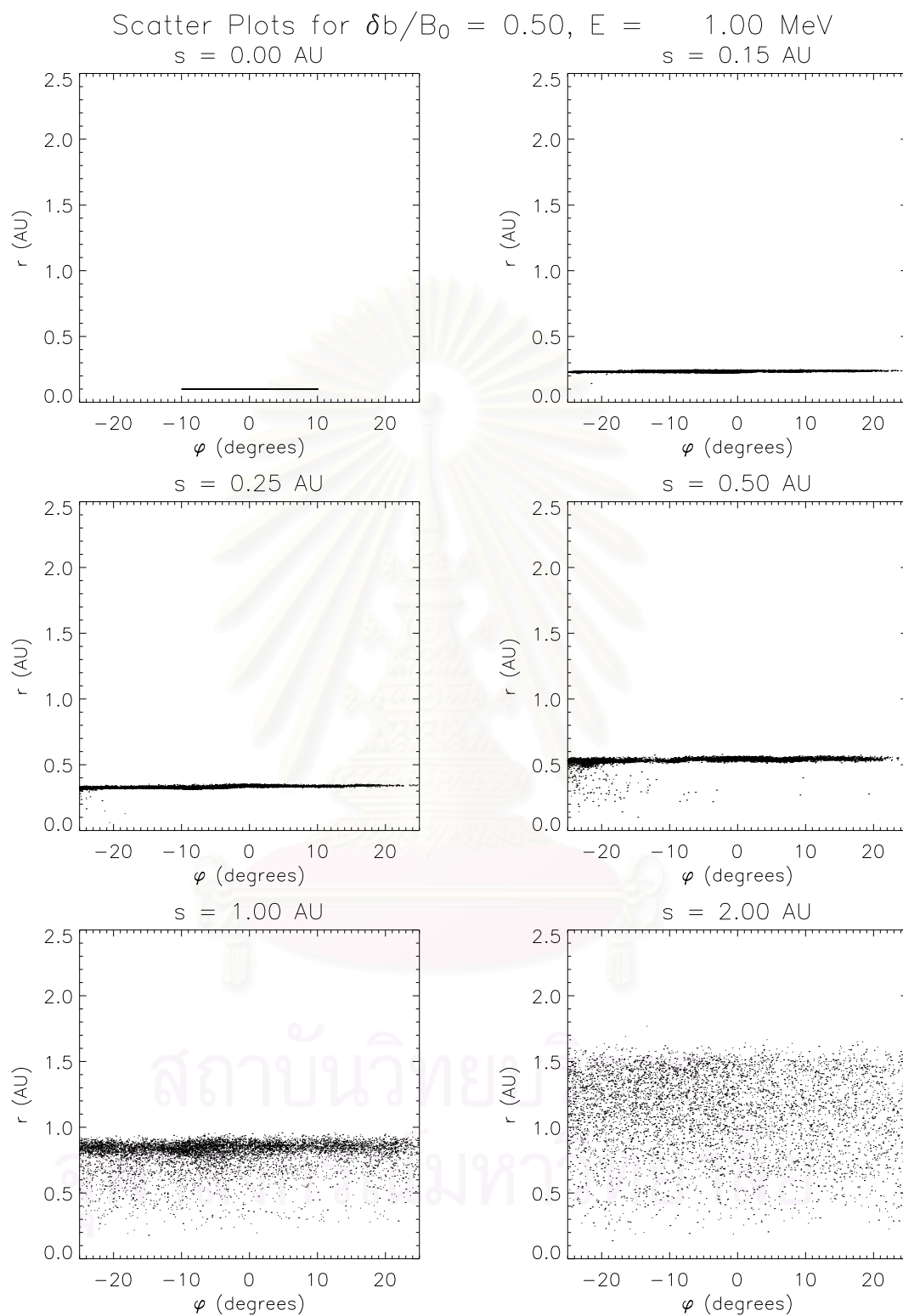


Figure 6.8: Scatter plots of φ vs. r for a particle energy of 1 MeV at $s = 0.0$, 0.15, 0.25, 0.5, 1, and 2 AU.

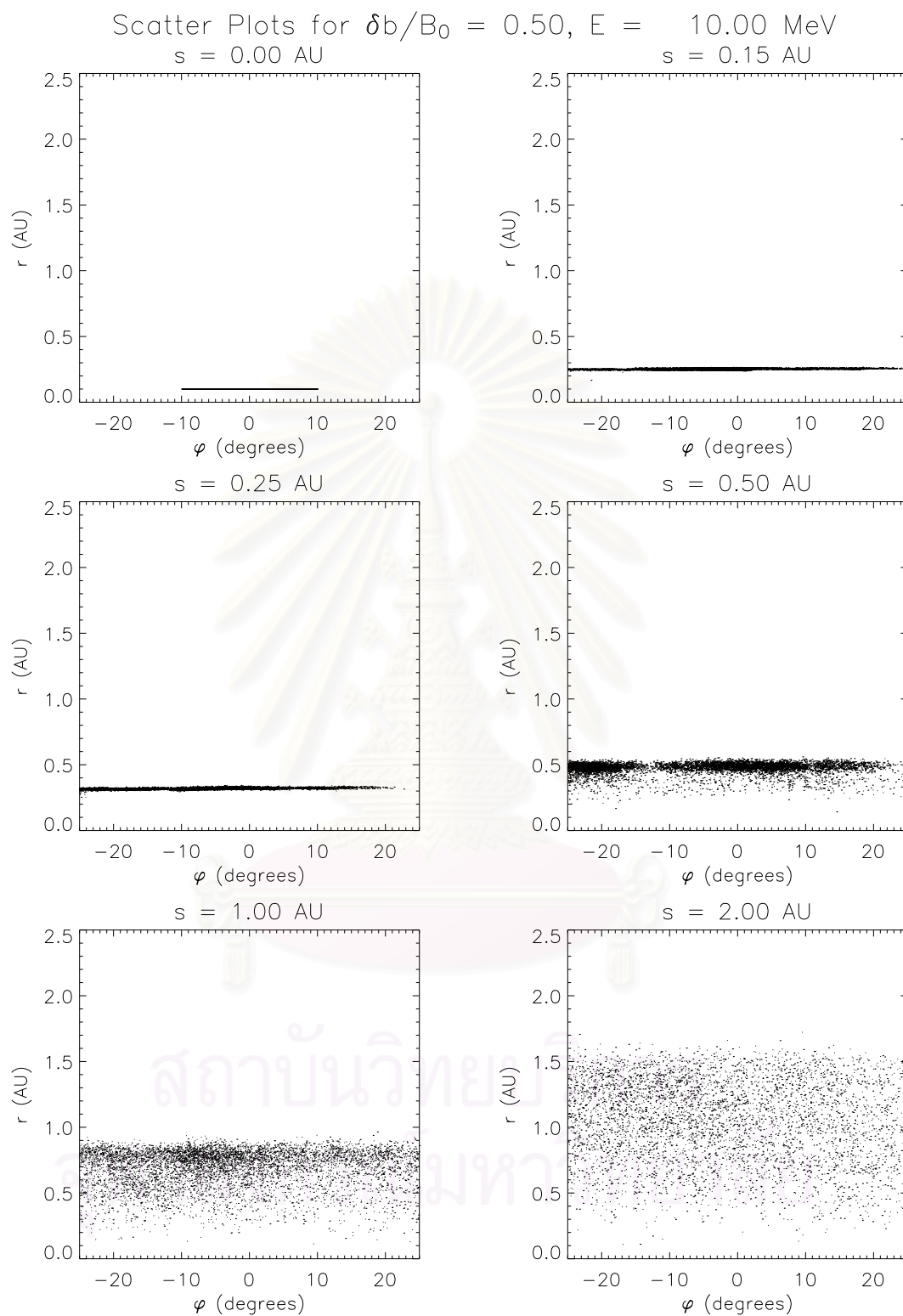


Figure 6.9: Scatter plots of φ vs. r for a particle energy of 10 MeV at $s = 0.0$, 0.15, 0.25, 0.5, 1, and 2 AU.

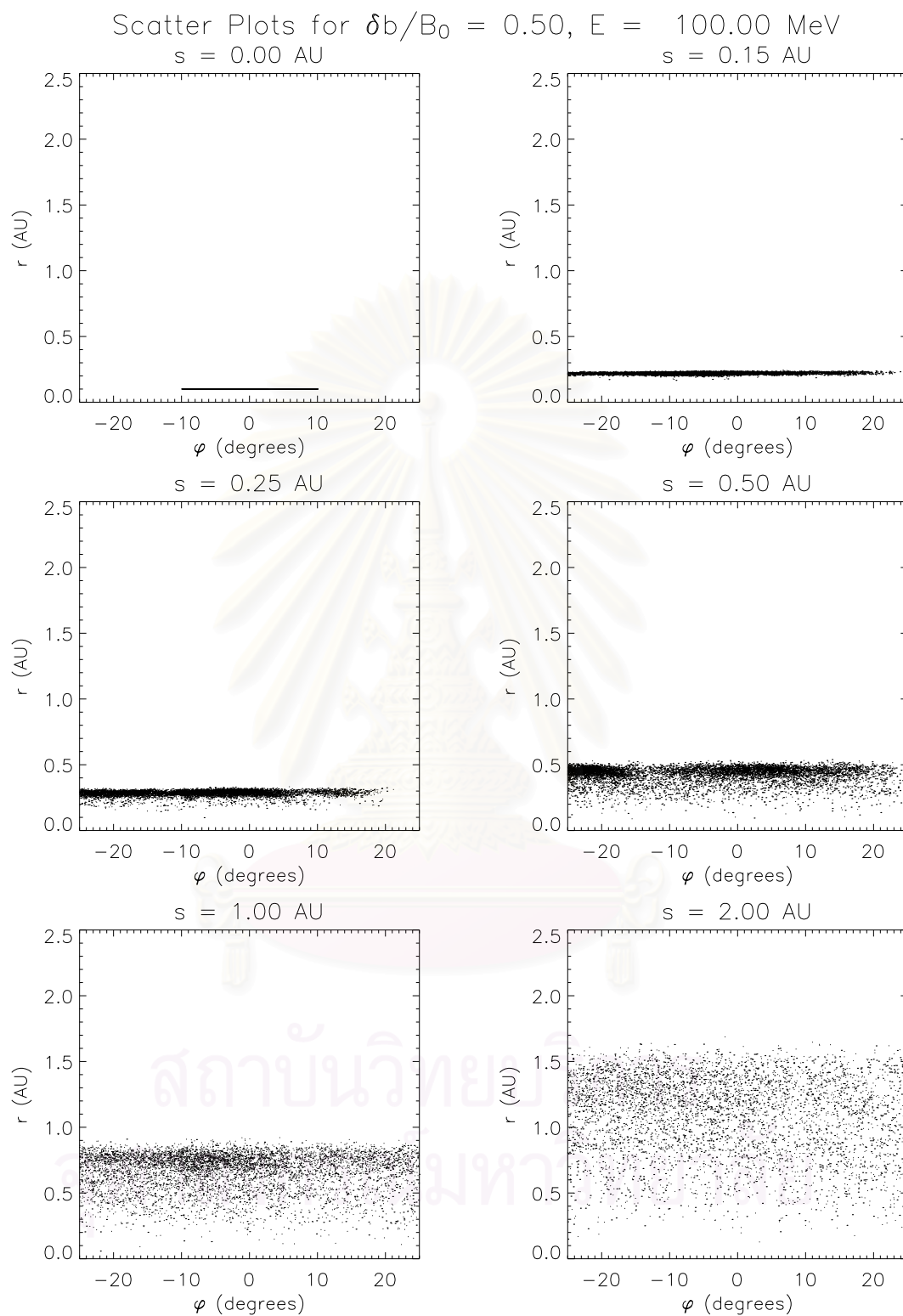


Figure 6.10: Scatter plots of φ vs. r for a particle energy of 100 MeV at $s = 0.0$, 0.15, 0.25, 0.5, 1, and 2 AU.

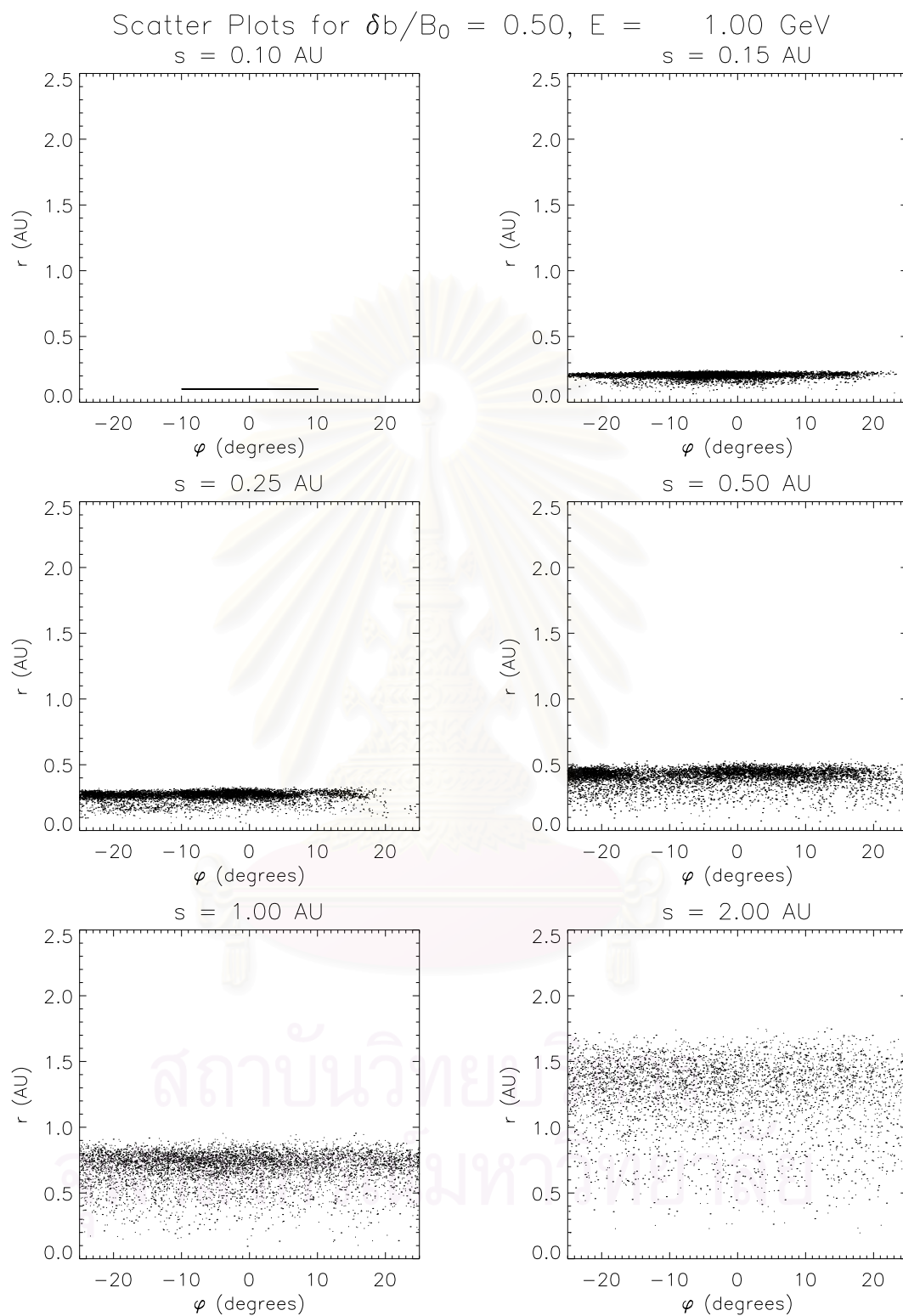


Figure 6.11: Scatter plots of φ vs. r for a particle energy of 1 GeV at $s = 0.0$, 0.15, 0.25, 0.5, 1, and 2 AU.

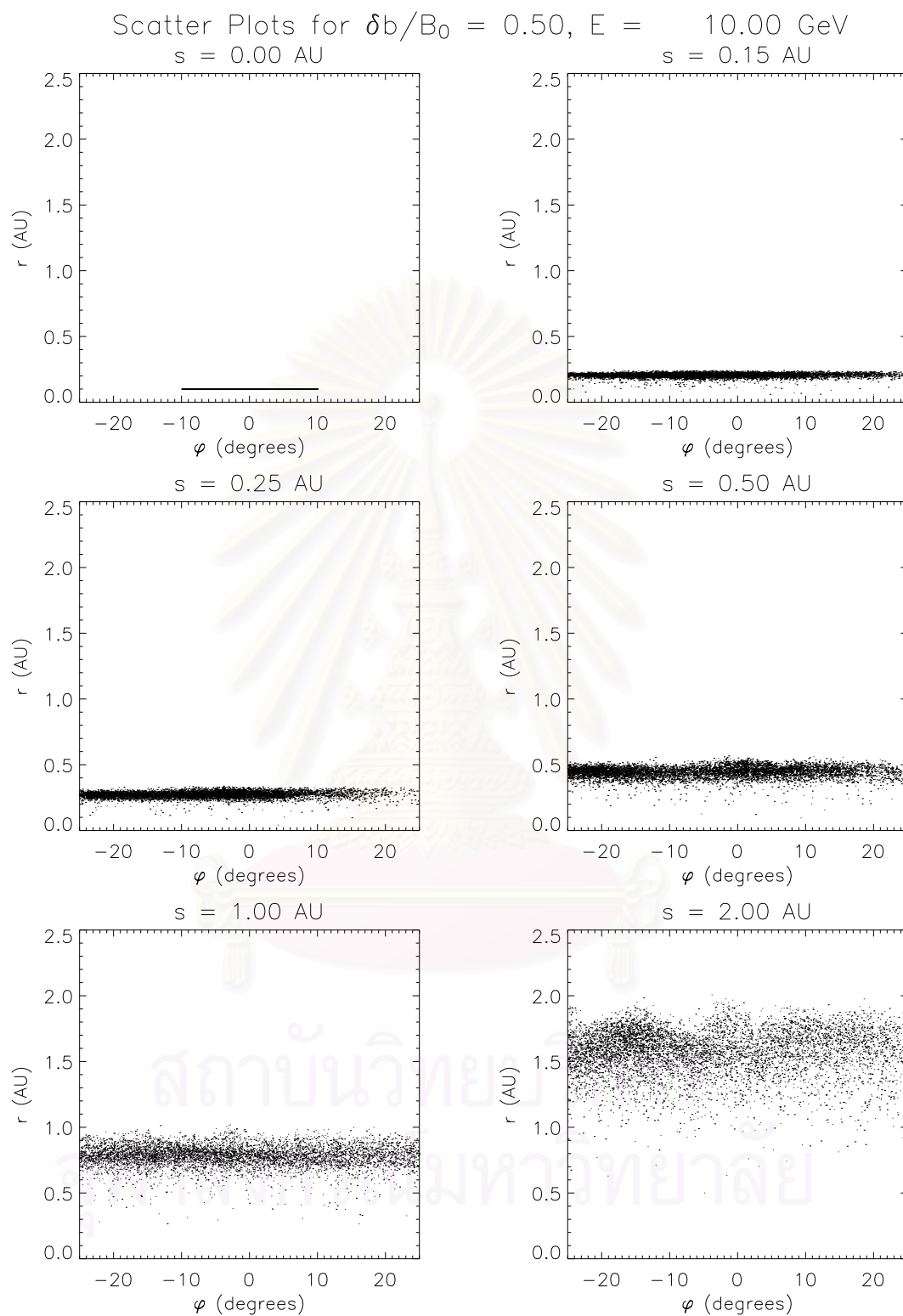


Figure 6.12: Scatter plots of φ vs. r for a particle energy of 10 GeV at $s = 0.0$, 0.15, 0.25, 0.5, 1, and 2 AU.

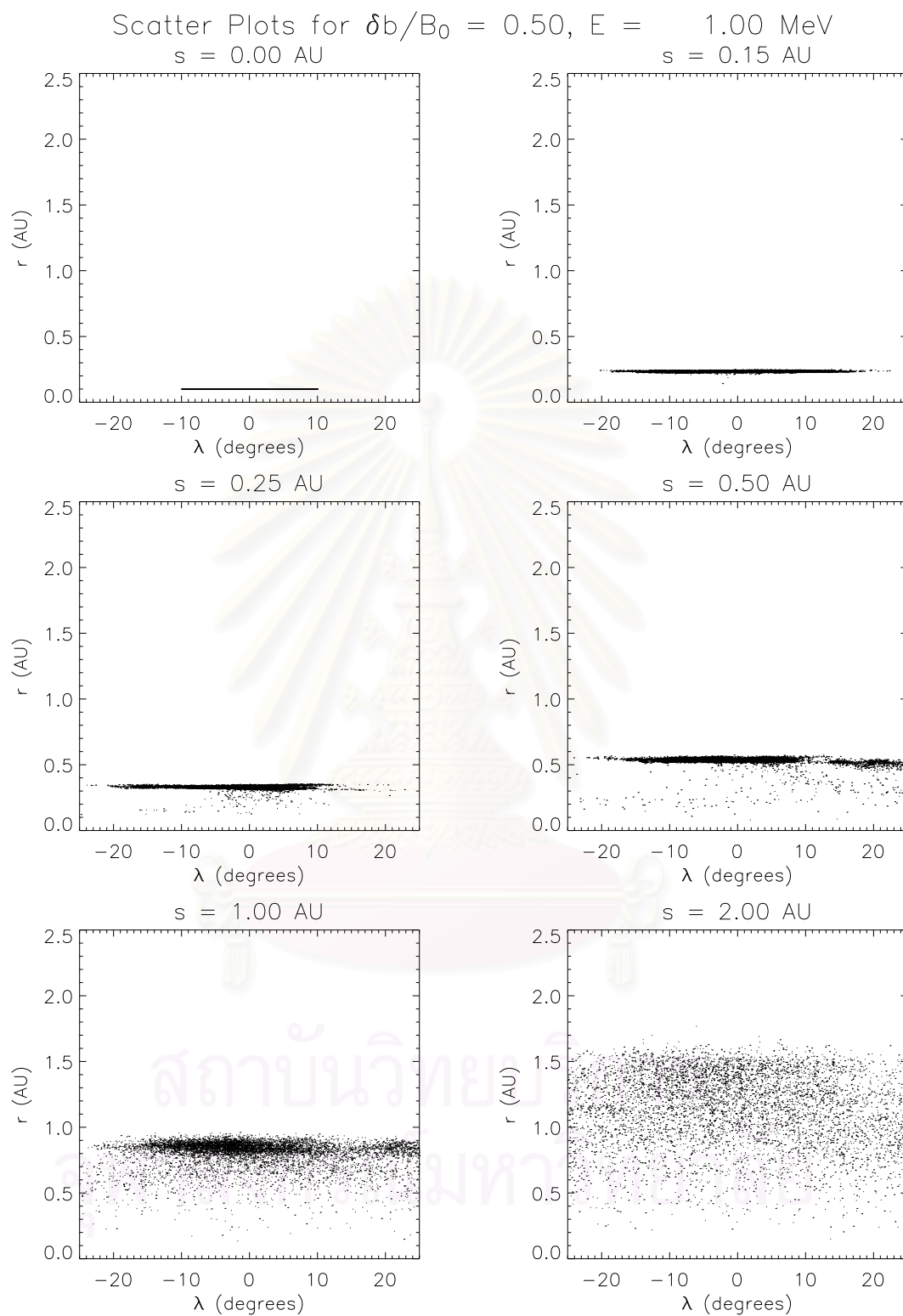


Figure 6.13: Scatter plots of λ vs. r for a particle energy of 1 MeV at $s = 0.0$, 0.15, 0.25, 0.5, 1, and 2 AU.

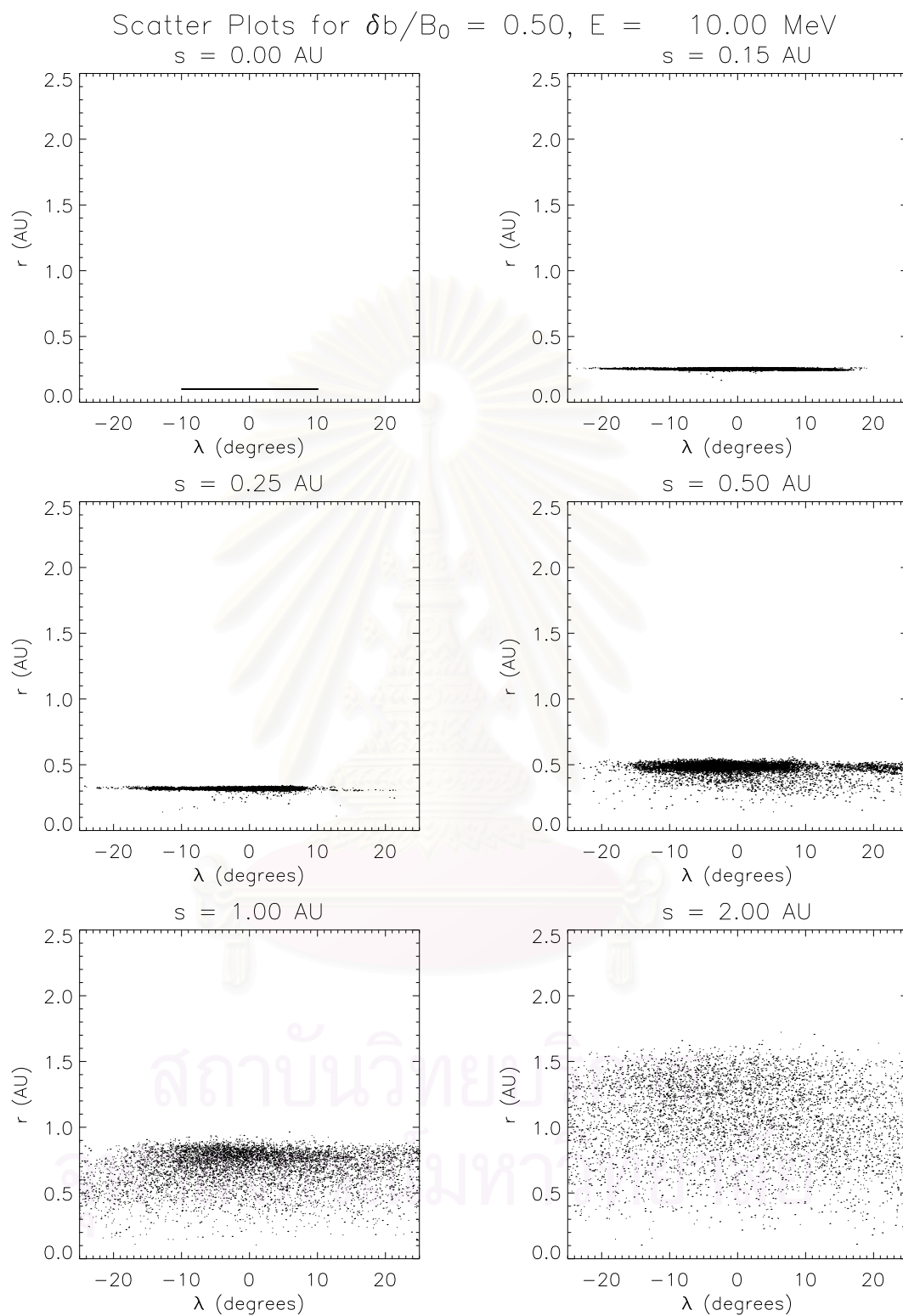


Figure 6.14: Scatter plots of λ vs. r for a particle energy of 10 MeV at $s = 0.0$, 0.15, 0.25, 0.5, 1, and 2 AU.

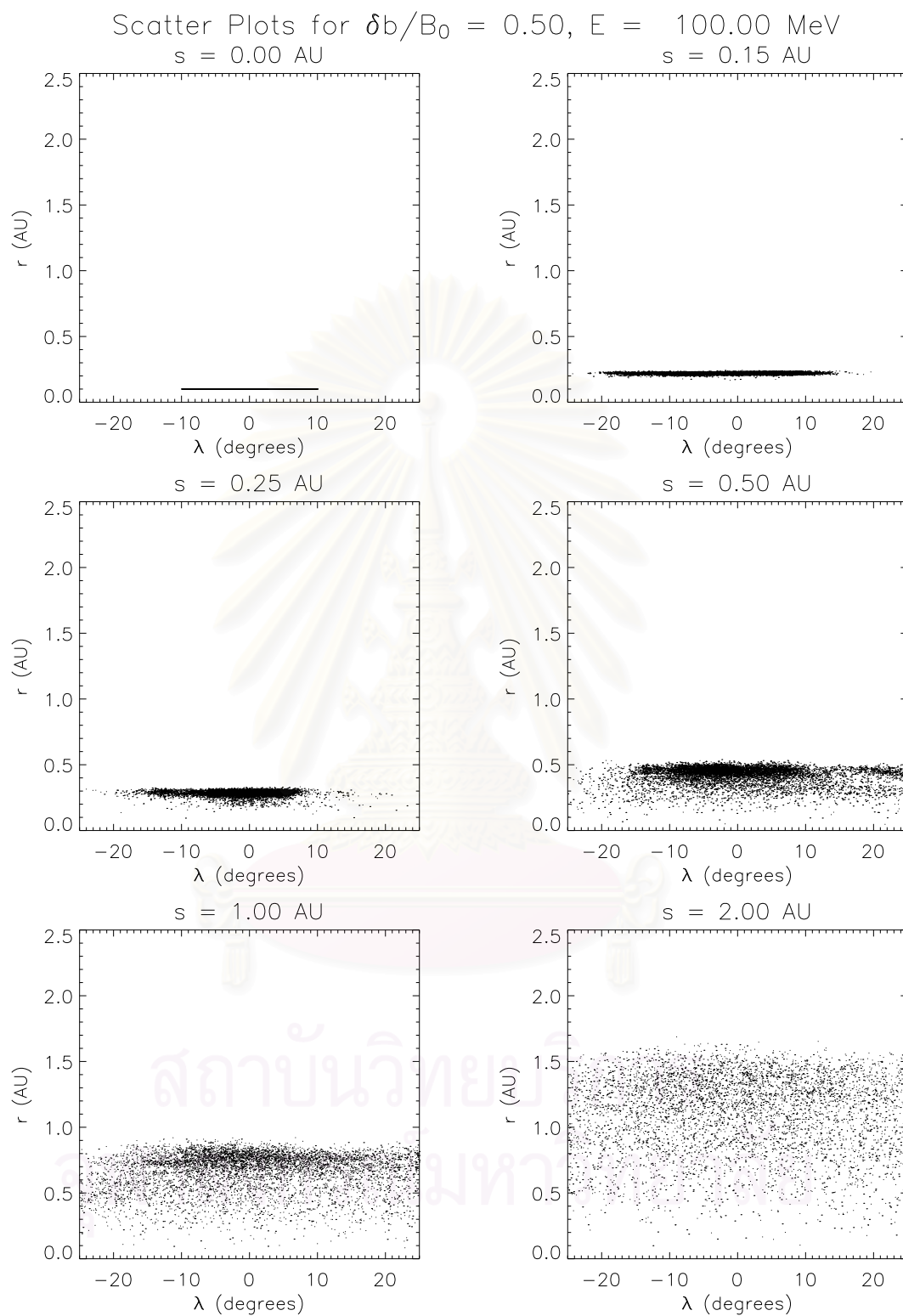


Figure 6.15: Scatter plots of λ vs. r for a particle energy of 100 MeV at $s = 0.0$, 0.15, 0.25, 0.5, 1, and 2 AU.

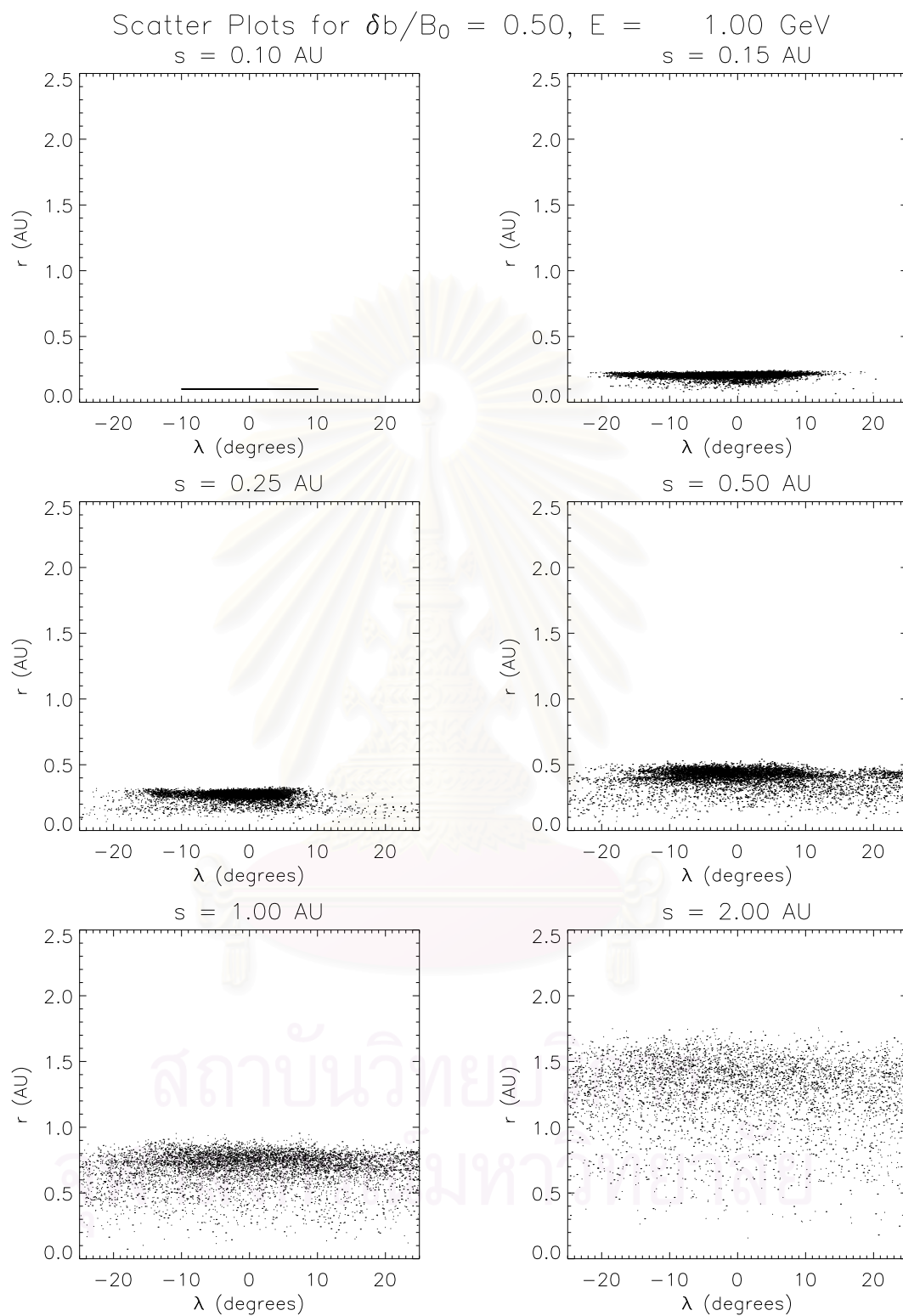


Figure 6.16: Scatter plots of λ vs. r for a particle energy of 1 GeV at $s = 0.0$, 0.15, 0.25, 0.5, 1, and 2 AU.

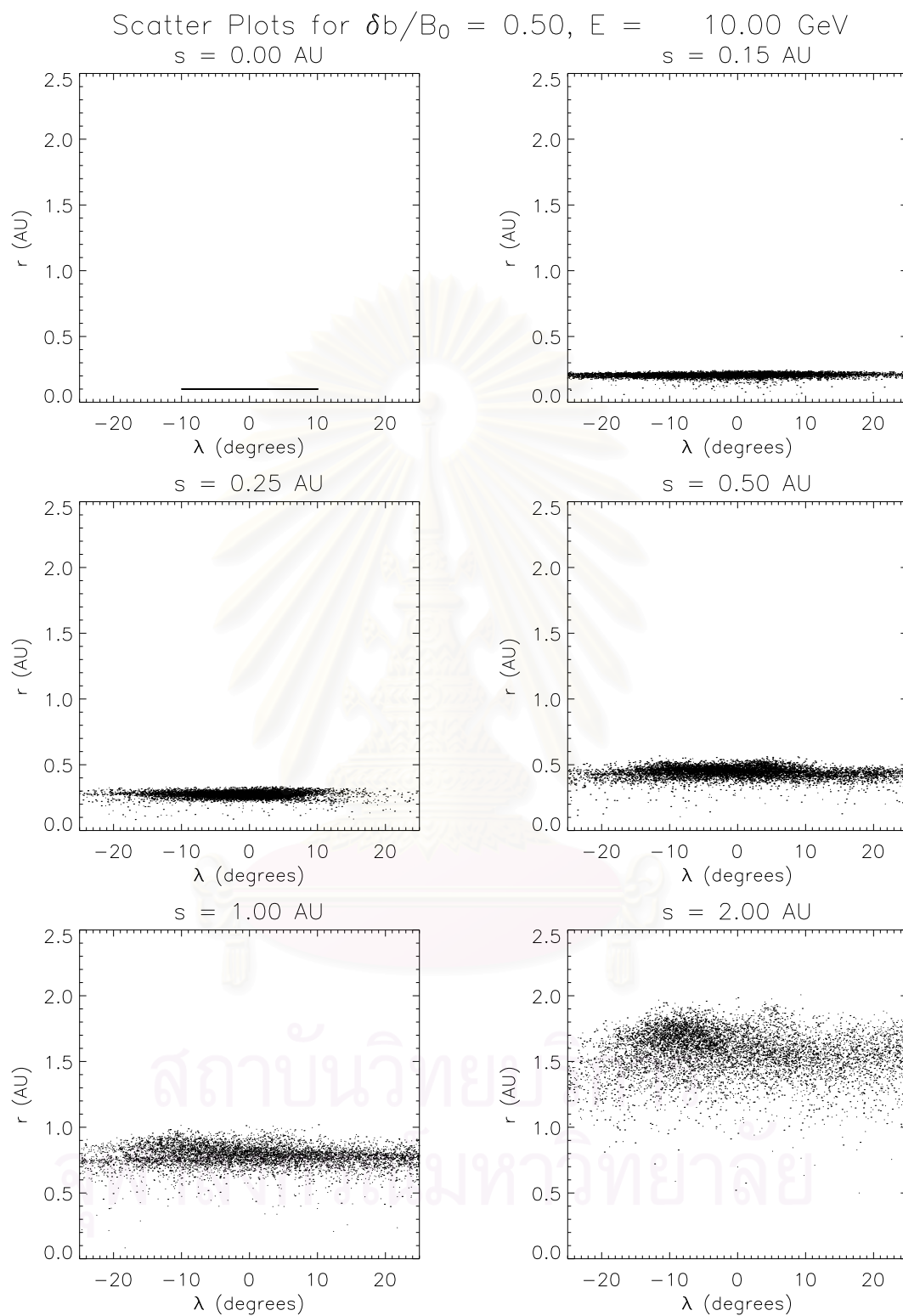


Figure 6.17: Scatter plots of λ vs. r for a particle energy of 10 GeV at $s = 0.0$, 0.15, 0.25, 0.5, 1, and 2 AU.

Chapter VII

Discussion and Conclusions

From Chapter IV, we can conclude that charged test particles moving in a uniform mean magnetic field with random perturbations will, after moving a few turbulence correlation lengths, experience spatial diffusion, or some other time-asymptotic transport (such as compound diffusion, or subdiffusion.) The present numerical results show that when additional, modest perturbations in the form of closed two-dimensional flux tubes are present, the time for some particles to attain the time-asymptotic regime of spatial transport can be greatly increased. This is due to temporary trapping in the transverse magnetic topology imposed by flux tubes. Particles of lower energy that are deeply embedded in stronger flux tubes of this type are expected to most prominently display trapping, suppressed escape, and the associated delays in perpendicular transport.

The effect described is the direct analog for particles of the topological trapping and suppressed diffusive escape of magnetic field lines from the vicinity of O-type neutral points in the transverse, 2D fluctuation fields (Ruffolo et al., 2003; Chuychai et al., 2005, 2007). The present ideas may be relevant to heliospheric phenomena such as dropouts that appear to require weaker or absent diffusion. Here we see that the trapping delays the onset of asymptotic transport, but does not prevent it, and that during this time, sharp gradients can persist, possibly appearing over a great span of heliocentric distance. To assess this idea more quantitatively in the context of dropouts, a more detailed model has also been developed, including a radially expanding field, i.e., a spherical geometry.

The interplanetary magnetic fields of the Sun actually have a spiral shape,

and at small r there is very strong focusing of the particles to move directly along the mean field. Such focusing can be modeled using a radial mean field, which also allows a generalization of the 2D + slab model of turbulence. Then we can neglect the spiral curvature, which is not very important between the Earth and the Sun. We simulated particle and magnetic field line trajectories for a slab + 2D random phase field in a spherical geometry. These simulations are more realistic than those in a Cartesian geometry.

The results from Chapter VI show that the scatter plots of the locations of magnetic field lines and charged particles of various energies at fixed radius are quite similar up to an energy of 1 GeV. The particles are trapped in small 2D islands with high density, but the particles outside the 2D island move to other regions and spread quickly to large angular distances with low density. This distribution of the trapped particles corresponds to the dropout features. At 10 GeV, the dropouts are less clear in scatter plots for 1 AU. This shows that if the gyroradius of particles is larger than the size of 2D islands, the dropouts will be less clear. Our results are consistent with the finding of McKibben et al. (2001) that the solar energetic particles spread over $\sim 90^\circ$ in angular distance after a few days. Then we can say that the particles of < 1 GeV follow the field lines very closely, so dropout patterns can be simulated by using field line tracing (in spherical geometry) as well as particle tracing.

To compare our results with Giacalone et al. (2000), who first modeled dropouts, their model of the magnetic fields has turbulence associated with the footpoint motion at a solar source surface, whereas our model takes interplanetary fluctuations to be generated by a turbulent cascade along the path from the Sun to the Earth. The results of Giacalone et al. (2006) show that two types of models, the model of fluctuations generated by random footpoint motion (Giacalone et al., 2000) and a model for generating interplanetary turbulent fluctuations (Ruffolo

et al., 2003; Chuychai et al., 2005) are closely related. Our line of work is different in that we explore mechanisms of dropouts, such as the trapping (Ruffolo et al., 2003) and suppressed diffusion (Chuychai et al., 2005, 2007) of the particles. This work first showed the scatter plots, which indicated spreading of the random walk of the particles at long distances, as inferred from the IMP-8 or Ulysses spacecraft (McKibben et al., 2001).

Mazur et al. (2000) found that the size of the dropout structures inferred from the ACE mission is about 0.03 AU or about 1.72 degrees. In our simulations the size of 2D islands is determined by the length scale of the 2D turbulence (l_{\perp}). We use $l_{\perp} \sim 0.1$ radians or about 0.1 AU or 5.73 degrees, based on fits to Ulysses data (Chuychai, 2004). The size of 2D islands in our simulations is larger than the size observed from the ACE spacecraft. Then, if we want the size of the 2D islands to be same as in the observations, we may need to use another power spectrum to get l_{\perp} less than 0.1 AU, while still fitting Ulysses data, which indicates that the 2D fluctuations may have another model or mechanism.

For future work, we will simulate the particle motion in 2D turbulence modeled by a spherical harmonic expansion, which is appropriate for a spherical geometry. We will also find the diffusion coefficient of particles in a spherical 2D Gaussian field and the statistics of diffusion.

สถาบันวิทยบริการ
จุฬาลงกรณ์มหาวิทยาลัย

References

- Bieber, J. W., Wanner, W., and Matthaeus, W. H. Dominant two-dimensional solar wind turbulence with implications for cosmic ray transport. J. Geophys. Res. **101** (1996): 2511-2522.
- Bieber, J. W., Matthaeus, W. H., Smith, C. W., Wanner, W., Kallenrode, M., and Wibberenz, G. Proton and electron mean free paths: The Palmer consensus revisited. Astrophys. J. **420** (1994): 294.
- Chuychai, P. Models of Random Magnetic Fields and Some Implications for Turbulence Structure and Particle Transport in the Heliosphere. Ph.D. Thesis, Department of Physics, Faculty of Science, Chulalongkorn University, 2004.
- Chuychai, P., Ruffolo, D., Matthaeus, W. H., and Meechai, J. Trapping and diffusive escape of field lines in two-component magnetic turbulence. Astrophys. J. **659** (2007): 1761.
- Chuychai, P., Ruffolo, D., Matthaeus, W. H., and Rowlands, G. Suppressed diffusive escape of topologically trapped magnetic field lines. Astrophys. J. Lett. **633** (2005): L49.
- Fisk, L. A. Motion of the footpoints of heliospheric magnetic field lines at the Sun: Implications for recurrent energetic particle events at high heliographic latitudes. J. Geophys. Res. **101** (1996): 15547.
- Giacalone, J., Jokipii, J. R., and Mazur, J. E. Small-scale gradients and large-scale diffusion of charged particles in the heliospheric magnetic field. Astrophys. J. Lett. **532** (2000): L75.
- Jokipii, J. R. Cosmic-ray propagation. I. Charged particles in a random magnetic field. Astrophys. J. **146** (1966): 480.
- Jokipii, J. R., Kóta, J., and Giacalone, J. Perpendicular transport in 1- and 2-dimensional shock simulations. Geophys. Res. Lett. **20** (1993): 1759.

- Jones, F. C., Jokipii, J. R., and Baring, M. G. Charged-particle motion in electromagnetic fields having at least one ignorable spatial coordinate. *Astrophys. J.* **509** (1998): 238.
- Kolmogorov, A. N. The local structure of turbulence in incompressible viscous fluid for very large Reynolds numbers. *C. R. Acad. Sci. URSS*, **30** (1941): 301.
- Matthaeus, W. H., Goldstein, M. L., and Roberts, D. A. Evidence for the presence of quasi-two-dimensional nearly incompressible fluctuations in the solar wind. *J. Geophys. Res.* **95** (1990): 20673.
- Matthaeus, W. H., Gray, P. C., Pontius, D. H., Jr., and Bieber, J. W. Spatial structure and field-line diffusion in transverse magnetic turbulence. *Phys. Rev. Lett.* **75** (1995): 2136.
- Mazur, J. E., Mason, G. M., Dwyer, J. R., Giacalone, J., Jokipii, J. R., and Stone, E. C. Interplanetary magnetic field line mixing deduced from impulsive solar flare particles. *Astrophys. J.* **532** (2000): L79.
- McKibben, R. B., Lopate, C., and Zhang, M. Simultaneous observations of solar energetic particle events by IMP 8 and the Ulysses COSPIN high energy telescope at high solar latitudes. *Space Sci. Rev.* **97** (2001): 257.
- Parker, E. N. Dynamics of the interplanetary gas and magnetic field, *Astrophys. J.* **128** (1958): 664-676.
- Parker, E. N. The passage of energetic charged particles through interplanetary space. *Planet. Space Sci.* **13** (1965): 949.
- Pope, S. B. *Turbulent Flows*: Cambridge University Press, 2000.
- Qin, G., Matthaeus, W. H., and Bieber, J. W. Subdiffusive transport of charged particles perpendicular to the large scale magnetic field. *Geophys. Res. Lett.* **29** (2002a): 7-1.
- Qin, G., Matthaeus, W. H., and Bieber, J. W. Perpendicular transport of charged particles in composite model turbulence: Recovery of diffusion. *Astrophys. J.* **578** (2002b): L117.

- Reames, D. V. Trapping and escape of the high energy particles responsible for major proton events. Eruptive Solar Flares. Proceedings of Colloquium #133 of the International Astronomical Union, held at Iguazú, Argentina, August 2-6, 1991, 180-185, New York: Springer-Verlag, 1992.
- Ruffolo, D., and Khumlumlert, T. Formation, Propagation, and Decay of Coherent Pulses of Solar Cosmic Rays. Geophys. Res. Lett. **22** (1995): 2073-2076.
- Ruffolo, D., Matthaeus, W. H., and Chuychai, P. Trapping of solar energetic particles by the small-scale topology of solar wind turbulence. Astrophys. J. **597** (2003): L169.
- Tennekes, H., and Lumley, J. L. A First Course in Turbulence: MIT Press, 1994.
- Tooprakai, P., Chuychai, P., Minnie, J., Ruffolo, D., Bieber, J. W., and Matthaeus, W. H. Temporary topological trapping and escape of charged particles in a flux tube as a cause of delay in time asymptotic transport. Geophys. Res. Lett. **34** (2007): L17105.
- Webb, G. M., Zank, G. P., Khashvili, E. Kh., and Le Roux, J. A. Compound and Perpendicular Diffusion of Cosmic Rays and Random Walk of the Field Lines. I. Parallel Particle Transport Models. Astrophys. J. **651** (2006): 211.



Appendices

สถาบันวิทยบริการ
จุฬาลงกรณ์มหาวิทยาลัย

Appendix A

Normalization of the Equation of Motion

The equation of motion of a charged particle in an electromagnetic field is given by the Newton-Lorentz equation:

$$\mathbf{F} = \frac{d}{dt}[\mathbf{p}(t)] = \frac{d}{dt}[\gamma m \mathbf{v}(t)] = q[\mathbf{E}(\mathbf{r}, t) + \mathbf{v}(t) \times \mathbf{B}(\mathbf{r}, t)], \quad (\text{A.1})$$

where \mathbf{p} is the relativistic particle momentum, \mathbf{v} is the particle velocity, q is the charge, m is the mass, \mathbf{E} is the electric field, \mathbf{B} is the magnetic field, t is the time, and γ is the Lorentz factor.

For this case, we consider only a static magnetic field \mathbf{B} , depending on only \mathbf{r} , so $\mathbf{B}(\mathbf{r}, t) \equiv \mathbf{B}(\mathbf{r})$. The electric field and the time variations of \mathbf{B} can be neglected because the velocity of particles in this case is greater than the Alfvén wave speed. In this case, there is conservation of the particle speed, $v = |\mathbf{v}| = \sqrt{v_x^2 + v_y^2 + v_z^2}$, and kinetic energy. We can explain this physically (following Ruffolo, 2002). The particle can change its kinetic energy or speed only if the force does work on the particle. The definition of work is

$$dW = \mathbf{F} \cdot d\mathbf{s}, \quad (\text{A.2})$$

so the rate of performing work on the particle is

$$\frac{dW}{dt} = \mathbf{F} \cdot \frac{d\mathbf{s}}{dt} = \mathbf{F} \cdot \mathbf{v}. \quad (\text{A.3})$$

For the magnetic force, we have

$$\frac{dW}{dt} = q(\mathbf{v} \times \mathbf{B}) \cdot \mathbf{v} = 0, \quad (\text{A.4})$$

since the cross product $\mathbf{v} \times \mathbf{B}$ is perpendicular to both \mathbf{v} and \mathbf{B} . That means the magnetic force is always perpendicular to the velocity, so it does no work on the particle, and can only change the direction of the particle velocity. For this reason, the kinetic energy and the speed of particle remain constant for any static magnetic field configuration. Since the magnitude of velocity $|\mathbf{v}|$ is constant, then γ is constant, too. Then the previous equation can be rewritten as

$$\frac{d}{dt}[\mathbf{v}(t)] = \frac{q}{\gamma m}[\mathbf{v}(t) \times \mathbf{B}(\mathbf{r})]. \quad (\text{A.5})$$

Now we can normalize this equation in terms of either the Alfvén speed or the speed of light.

A.1 Normalization by the Alfvén Speed

Let eq. (A.5) be rewritten to normalize \mathbf{v} to the Alfvén speed v_A , \mathbf{B} to the mean magnetic field B_0 in space near Earth, and \mathbf{r} to the correlation scale $l_{parallel}$ of the slab turbulence. The Alfvén speed is defined by

$$v_A = \frac{B_0}{\sqrt{\mu_0 \rho_0}} \quad (\text{A.6})$$

where ρ_0 is the density of particles near Earth and μ_0 is the magnetic permeability of free space.

For the normalization, we use

$$\left. \begin{aligned} t' &= \frac{t}{\tau_A}, & \text{and} & & \tau_A &= \frac{l_{\parallel}}{v_A}, \\ \mathbf{v}' &= \frac{\mathbf{v}}{v_A}, & \text{and} & & v_A &= \frac{B_0}{\sqrt{\mu_0 \rho_0}}, \\ \mathbf{B}' &= \frac{\mathbf{B}}{B_0}. \end{aligned} \right\} \quad (\text{A.7})$$

Dividing eq. (A.5) by v_A and using eq. (A.7),

$$\frac{d\mathbf{v}'}{dt} = \frac{qB_0}{\gamma m} [\mathbf{v}'(t') \times \mathbf{B}'(\mathbf{r}')] \quad (\text{A.8})$$

$$= \Omega_0 [\mathbf{v}'(t') \times \mathbf{B}'(\mathbf{r}')], \quad (\text{A.9})$$

where $\Omega_0 = (qB_0)/(\gamma m)$ is relativistic gyro-frequency of particles. Now multiplying by τ_A , we get

$$\frac{d}{dt'} [\mathbf{v}'(t')] = \Omega_0 \tau_A [\mathbf{v}'(t') \times \mathbf{v}'_A(\mathbf{r}')]. \quad (\text{A.10})$$

We set

$$\alpha_A = \Omega_0 \tau_A = \frac{qB_0 \tau_A}{\gamma m} = \frac{qB_0 l_{\parallel}}{\gamma m v_A} = \frac{qB_0}{\gamma m v} \frac{v}{v_A} l_{\parallel} = \frac{l_{\parallel}}{r_L} v', \quad (\text{A.11})$$

where $r_L = (\gamma m v)/(qB_0)$ is the Larmor radius of particles which have speed v at Earth, and $\alpha_A < 0$ for negatively charged particles and $\alpha_A > 0$ for positively charged particles. Then eq. (A.10) can be rewritten as

$$\frac{d}{dt'} [\mathbf{v}'(t')] = \alpha_A [\mathbf{v}'(t') \times \mathbf{B}'(\mathbf{r}')]. \quad (\text{A.12})$$

A.2 Normalization by the Speed of Light

Now we do the same thing as previously but change to normalize the variables using the speed of light (c). Then to normalize the equation we set

$$\left. \begin{aligned} t^* &= \frac{t}{\tau_c}, & \text{and} & & \tau_c &= \frac{l_{\parallel}}{c}, \\ \mathbf{v}^* &= \frac{\mathbf{v}}{c}, \\ \mathbf{r}^* &= \frac{\mathbf{r}}{l_{\parallel}}, \\ \mathbf{B}^* &= \frac{\mathbf{B}}{B_0}, \end{aligned} \right\} \quad (\text{A.13})$$

where B_0 is the mean magnetic field at Earth. Then eq. (A.5) can be changed to

$$\begin{aligned} \frac{d}{dt^*} [\mathbf{v}^*(t^*)] &= \frac{qB_0 \tau_c}{\gamma m} [\mathbf{v}^*(t^*) \times \mathbf{B}^*(\mathbf{r}^*)] \\ &= \Omega_0 \tau_c [\mathbf{v}^*(t^*) \times \mathbf{B}^*(\mathbf{r}^*)] \end{aligned} \quad (\text{A.14})$$

where $\Omega_0 = qB_0/(\gamma m)$ is the relativistic gyro-frequency at Earth. Now we obtain

$$\alpha_c = \Omega_0 \tau_c = \frac{qB_0 \tau_c}{\gamma m} = \frac{qB_0}{\gamma m} \frac{l_{\parallel}}{c} = \frac{qB_0}{\gamma m v} \frac{v}{c} l_{\parallel} = \frac{l_{\parallel}}{r_L} v^*, \quad (\text{A.15})$$

and eq. (A.14) can be rewritten as

$$\frac{d}{dt^*}[\mathbf{v}^*(t^*)] = \alpha_c[\mathbf{v}^*(t^*) \times \mathbf{B}^*(\mathbf{r}^*)] \quad (\text{A.16})$$

(Tooprakai et al. 2007).

The units of $\mathbf{B}(\mathbf{r})$ depend on B_0 , \mathbf{v} is in units of the speed of light and \mathbf{r} is in units of the correlation scale (l_{\parallel}). Therefore, if we use B_0 in arbitrary units, $\mathbf{B}(\mathbf{r})$ will be arbitrary units, too.

Example: If we use $B_0 = 5.0 \times 10^{-9}$ Tesla, but in α_c and the program we use $b_0 = 1.0$, this means that $b_0 = 1.0B_0$ or b_0 is in units of 5.0×10^{-9} Tesla.

For this work, we choose to normalize the equation of motion with the speed of light because the speed of light is constant in every position and reference frame in space, but the Alfvén speed in real space will vary with the distance and time. For normalization with the Alfvén speed, one would use the average Alfvén speed at Earth as the reference. These normalizations can be used in either Cartesian or spherical geometry.

สถาบันวิทยบริการ
จุฬาลงกรณ์มหาวิทยาลัย

Appendix B

Solving Equations of Motion in Spherical Coordinates

In this Appendix, we will show how we solve the equations of motion used in our program. We begin with Lagrange's equations of motion:

$$\frac{\partial \mathcal{L}}{\partial q_i} - \frac{d}{dt} \frac{\partial \mathcal{L}}{\partial \dot{q}_i} = 0, \quad (\text{B.1})$$

and the Lagrangian

$$\mathcal{L} = \frac{1}{2}m(\dot{\mathbf{r}})^2 + q\dot{\mathbf{r}} \cdot \mathbf{A}(\mathbf{r}, t), \quad (\text{B.2})$$

where

$$\mathbf{r} = r\hat{r}, \quad (\text{B.3})$$

and

$$\begin{aligned} \dot{\mathbf{r}} &= \dot{r}\hat{r} + r\dot{\lambda}\hat{\lambda} + r\cos\lambda\dot{\phi}\hat{\phi}, \\ (\dot{\mathbf{r}})^2 &= \dot{\mathbf{r}} \cdot \dot{\mathbf{r}} = \dot{r}^2 + r^2\dot{\lambda}^2 + r^2\cos^2\lambda\dot{\phi}^2. \end{aligned} \quad (\text{B.4})$$

We also have

$$\begin{aligned} \mathbf{A}(\mathbf{r}) &= A_r\hat{r} + A_\lambda\hat{\lambda} + A_\phi\hat{\phi} \\ \dot{\mathbf{r}} \cdot \mathbf{A}(\mathbf{r}) &= \left(\dot{r}\hat{r} + r\dot{\lambda}\hat{\lambda} + r\cos\lambda\dot{\phi}\hat{\phi}\right) \cdot \left(A_r\hat{r} + A_\lambda\hat{\lambda} + A_\phi\hat{\phi}\right) \\ &= \dot{r}A_r + r\dot{\lambda}A_\lambda + r\cos\lambda\dot{\phi}A_\phi. \end{aligned} \quad (\text{B.5})$$

From eqs. (B.3) - (B.5), we get

$$\mathcal{L} = \frac{1}{2}m\left(\dot{r}^2 + r^2\dot{\lambda}^2 + r^2\cos^2\lambda\dot{\phi}^2\right) + q\left(\dot{r}A_r + r\dot{\lambda}A_\lambda + r\cos\lambda\dot{\phi}A_\phi\right). \quad (\text{B.6})$$

First, we consider the Lagrange's equation of motion in the \hat{r} direction.

From eq. (B.1), we get

$$\frac{\partial \mathcal{L}}{\partial r} - \frac{d}{dt} \frac{\partial \mathcal{L}}{\partial \dot{r}} = 0. \quad (\text{B.7})$$

Then from eq. (B.6) and eq. (B.7), we get

$$\begin{aligned}\frac{\partial \mathcal{L}}{\partial r} &= \frac{1}{2}m \left(2r\dot{\lambda}^2 + 2r \cos^2 \lambda \dot{\phi}^2 \right) \\ &+ q \left(\dot{r} \frac{\partial A_r}{\partial r} + \dot{\lambda} A_\lambda + r \dot{\lambda} \frac{\partial A_\lambda}{\partial r} + \cos \lambda \dot{\phi} A_\varphi + r \cos \lambda \dot{\phi} \frac{\partial A_\varphi}{\partial r} \right) \\ &= mr\dot{\lambda}^2 + mr \cos^2 \lambda \dot{\phi}^2 + q\dot{r} \frac{\partial A_r}{\partial r} + q\dot{\lambda} A_\lambda + qr \dot{\lambda} \frac{\partial A_\lambda}{\partial r} \\ &+ q \cos \lambda \dot{\phi} A_\varphi + qr \cos \lambda \dot{\phi} \frac{\partial A_\varphi}{\partial r},\end{aligned}\quad (\text{B.8})$$

$$\frac{\partial \mathcal{L}}{\partial \dot{r}} = \frac{1}{2}m(2\dot{r}) + qA_r = m\dot{r} + qA_r, \quad (\text{B.9})$$

$$\frac{d}{dt} \frac{\partial \mathcal{L}}{\partial \dot{r}} = m\ddot{r} + q \frac{dA_r}{dt}. \quad (\text{B.10})$$

Substituting eq. (B.8) and eq. (B.10) in eq. (B.7),

$$\begin{aligned}mr\dot{\lambda}^2 + mr \cos^2 \lambda \dot{\phi}^2 + q\dot{r} \frac{\partial A_r}{\partial r} + q\dot{\lambda} A_\lambda + qr \dot{\lambda} \frac{\partial A_\lambda}{\partial r} + q \cos \lambda \dot{\phi} A_\varphi \\ + qr \cos \lambda \dot{\phi} \frac{\partial A_\varphi}{\partial r} - m\ddot{r} - q \frac{dA_r}{dt} = 0,\end{aligned}$$

$$\begin{aligned}\ddot{r} &= r\dot{\lambda}^2 + r \cos^2 \lambda \dot{\phi}^2 + \frac{q}{m}\dot{r} \frac{\partial A_r}{\partial r} + \frac{q}{m}\dot{\lambda} A_\lambda + \frac{q}{m}r \dot{\lambda} \frac{\partial A_\lambda}{\partial r} + \frac{q}{m} \cos \lambda \dot{\phi} A_\varphi \\ &+ \frac{q}{m}r \cos \lambda \dot{\phi} \frac{\partial A_\varphi}{\partial r} - \frac{q}{m} \frac{dA_r}{dt}.\end{aligned}\quad (\text{B.11})$$

Next we consider the $\hat{\lambda}$ direction and we get

$$\frac{\partial \mathcal{L}}{\partial \lambda} - \frac{d}{dt} \frac{\partial \mathcal{L}}{\partial \dot{\lambda}} = 0. \quad (\text{B.12})$$

Then

$$\begin{aligned}\frac{\partial \mathcal{L}}{\partial \lambda} &= \frac{1}{2}m \left(2r^2 \cos \lambda (-\sin \lambda) \dot{\phi}^2 \right) \\ &+ q \left(\dot{r} \frac{\partial A_r}{\partial \lambda} + r \dot{\lambda} \frac{\partial A_\lambda}{\partial \lambda} + r \cos \lambda \dot{\phi} \frac{\partial A_\varphi}{\partial \lambda} - r \sin \lambda \dot{\phi} A_\varphi \right) \\ &= -mr^2 \cos \lambda \sin \lambda \dot{\phi}^2 + q\dot{r} \frac{\partial A_r}{\partial \lambda} + qr \dot{\lambda} \frac{\partial A_\lambda}{\partial \lambda} + qr \cos \lambda \dot{\phi} \frac{\partial A_\varphi}{\partial \lambda} \\ &- qr \sin \lambda \dot{\phi} A_\varphi,\end{aligned}\quad (\text{B.13})$$

$$\frac{\partial \mathcal{L}}{\partial \dot{\lambda}} = \frac{1}{2}m(2r^2\dot{\lambda}) + qrA_\lambda = mr^2\dot{\lambda} + qrA_\lambda, \quad (\text{B.14})$$

$$\frac{d}{dt} \frac{\partial \mathcal{L}}{\partial \dot{\lambda}} = mr^2\ddot{\lambda} + 2mr\dot{\lambda}\dot{r} + q\dot{r}A_r + qr\frac{dA_\lambda}{dt}. \quad (\text{B.15})$$

Substituting eq. (B.14) and eq. (B.15) in eq. (B.12), we get

$$\begin{aligned} & -mr^2 \cos \lambda \sin \lambda \dot{\varphi}^2 + q\dot{r} \frac{\partial A_r}{\partial \lambda} + qr\dot{\lambda} \frac{\partial A_\lambda}{\partial \lambda} + qr \cos \lambda \dot{\varphi} \frac{\partial A_\varphi}{\partial \lambda} \\ & -qr \sin \lambda \dot{\varphi} A_\varphi - mr^2 \ddot{\lambda} - 2mr\dot{\lambda}\dot{r} - q\dot{r}A_r - qr\frac{dA_\lambda}{dt} = 0, \end{aligned}$$

$$\begin{aligned} \ddot{\lambda} = & -\cos \lambda \sin \lambda \dot{\varphi}^2 + \frac{q\dot{r}}{mr^2} \frac{\partial A_r}{\partial \lambda} + \frac{q\dot{\lambda}}{mr} \frac{\partial A_\lambda}{\partial \lambda} + \frac{q \cos \lambda \dot{\varphi}}{mr} \frac{\partial A_\varphi}{\partial \lambda} - \frac{q \sin \lambda \dot{\varphi} A_\varphi}{mr} \\ & - \frac{2\dot{\lambda}\dot{r}}{r} - \frac{q\dot{r}A_r}{mr^2} - \frac{q}{mr} \frac{dA_\lambda}{dt}. \end{aligned} \quad (\text{B.16})$$

Considering the $\hat{\varphi}$ direction, we get

$$\frac{\partial \mathcal{L}}{\partial \varphi} - \frac{d}{dt} \frac{\partial \mathcal{L}}{\partial \dot{\varphi}}. \quad (\text{B.17})$$

Then

$$\begin{aligned} \frac{\partial \mathcal{L}}{\partial \varphi} &= q \left(\dot{r} \frac{\partial A_r}{\partial \varphi} + r\dot{\lambda} \frac{\partial A_\lambda}{\partial \varphi} + r \cos \lambda \dot{\varphi} \frac{\partial A_\varphi}{\partial \varphi} \right) \\ &= q\dot{r} \frac{\partial A_r}{\partial \varphi} + qr\dot{\lambda} \frac{\partial A_\lambda}{\partial \varphi} + qr \cos \lambda \dot{\varphi} \frac{\partial A_\varphi}{\partial \varphi} \end{aligned} \quad (\text{B.18})$$

$$\begin{aligned} \frac{\partial \mathcal{L}}{\partial \dot{\varphi}} &= \frac{1}{2}mr^2 \cos^2 \lambda (2\dot{\varphi}) + q(r \cos \lambda A_\varphi) \\ &= mr^2 \cos^2 \lambda \dot{\varphi} + qr \cos \lambda A_\varphi \end{aligned} \quad (\text{B.19})$$

$$\begin{aligned} \frac{d}{dt} \frac{\partial \mathcal{L}}{\partial \dot{\varphi}} &= 2mr \cos^2 \lambda \dot{r}\dot{\varphi} - 2mr^2 \cos \lambda \sin \lambda \dot{\lambda}\dot{\varphi} + mr^2 \cos^2 \lambda \ddot{\varphi} + q \cos \lambda A_\varphi \dot{r} \\ & \quad - qr \sin \lambda A_\varphi \dot{\lambda} + qr \cos \lambda \frac{dA_\varphi}{dt}. \end{aligned} \quad (\text{B.20})$$

Substituting eq. (B.19) and eq. (B.20) in eq. (B.17), we get

$$\begin{aligned} & q\dot{r} \frac{\partial A_r}{\partial \varphi} + qr\dot{\lambda} \frac{\partial A_\lambda}{\partial \varphi} + qr \cos \lambda \dot{\varphi} \frac{\partial A_\varphi}{\partial \varphi} - 2mr \cos^2 \lambda \dot{r}\dot{\varphi} + 2mr^2 \cos \lambda \sin \lambda \dot{\lambda}\dot{\varphi} \\ & \quad - mr^2 \cos^2 \lambda \ddot{\varphi} - q \cos \lambda A_\varphi \dot{r} + qr \sin \lambda A_\varphi \dot{\lambda} - qr \cos \lambda \frac{dA_\varphi}{dt} = 0 \end{aligned}$$

$$\ddot{\varphi} = \frac{q\dot{r}}{mr^2 \cos^2 \lambda} \frac{\partial A_r}{\partial \varphi} + \frac{q\dot{\lambda}}{mr \cos^2 \lambda} \frac{\partial A_\lambda}{\partial \varphi} + \frac{q\dot{\varphi}}{mr \cos \lambda} \frac{\partial A_\varphi}{\partial \varphi} - \frac{2\dot{r}\dot{\varphi}}{r} + \frac{2 \sin \lambda \dot{\lambda} \dot{\varphi}}{\cos \lambda} - \frac{qA_\varphi \dot{r}}{mr^2 \cos \lambda} + \frac{q \sin \lambda A_\varphi \dot{\lambda}}{mr \cos^2 \lambda} - \frac{q}{mr \cos \lambda} \frac{dA_\varphi}{dt}. \quad (\text{B.21})$$

We can find the magnetic field from

$$\mathbf{B} = \nabla \times \mathbf{A}, \quad (\text{B.22})$$

and then we get

$$\mathbf{B} = \frac{1}{r \cos \lambda} \left[\frac{\partial A_\lambda}{\partial \varphi} - \frac{\partial(\cos \lambda A_\varphi)}{\partial \lambda} \right] \hat{r} + \frac{1}{r \cos \lambda} \left[\cos \lambda \frac{\partial(rA_\varphi)}{\partial r} - \frac{\partial A_r}{\partial \varphi} \right] \hat{\lambda} + \frac{1}{r} \left[\frac{\partial A_r}{\partial \lambda} - \frac{\partial(rA_r)}{\partial r} \right] \hat{\varphi}. \quad (\text{B.23})$$

We can rewrite eq. (B.23) for each component as

$$B_\varphi = \frac{1}{r} \frac{\partial A_r}{\partial \lambda} - \frac{\partial A_\lambda}{\partial r} - \frac{A_\lambda}{r}, \quad (\text{B.24})$$

$$B_\lambda = \frac{\partial A_\varphi}{\partial r} + \frac{A_\varphi}{r} - \frac{1}{r \cos \lambda} \frac{\partial A_r}{\partial \varphi}, \quad (\text{B.25})$$

$$B_r = \frac{1}{r \cos \lambda} \frac{\partial A_\lambda}{\partial \varphi} - \frac{1}{r} \frac{\partial A_\varphi}{\partial \lambda} + \frac{\sin \lambda A_\varphi}{r \cos \lambda}. \quad (\text{B.26})$$

From the velocity and the acceleration equation, we get

$$\left. \begin{aligned} v_r &= \dot{r} \\ v_\lambda &= r\dot{\lambda} \\ v_\varphi &= r \cos \lambda \dot{\varphi}, \end{aligned} \right\} \quad (\text{B.27})$$

or

$$\left. \begin{aligned} \dot{r} &= v_r \\ \dot{\lambda} &= \frac{v_\lambda}{r} \\ \dot{\varphi} &= \frac{v_\varphi}{r \cos \lambda}, \end{aligned} \right\} \quad (\text{B.28})$$

and

$$\left. \begin{aligned} \dot{v}_\varphi &= \cos \lambda \dot{r} \dot{\varphi} + r \cos \lambda \ddot{\varphi} - r \sin \lambda \dot{\lambda} \dot{\varphi} \\ \dot{v}_\lambda &= \dot{r} \dot{\lambda} + r \ddot{\lambda} \\ \dot{v}_r &= \ddot{r} \end{aligned} \right\} \quad (\text{B.29})$$

or

$$\left. \begin{aligned}
 \ddot{\varphi} &= \frac{1}{r \cos \lambda} \left[\dot{v}_\varphi - \cos \lambda \dot{r} \dot{\varphi} + r \sin \lambda \dot{\lambda} \dot{\varphi} \right] \\
 &= \frac{1}{r \cos \lambda} \left[\dot{v}_\varphi - \frac{v_r v_\varphi}{r} + \frac{\tan \lambda v_\lambda v_\varphi}{r} \right] \\
 \ddot{\lambda} &= \frac{1}{r} (\dot{v}_\lambda - \dot{r} \dot{\lambda}) = \frac{\dot{v}_\lambda}{r} - \frac{v_r v_\lambda}{r^2} \\
 \ddot{r} &= \dot{v}_r.
 \end{aligned} \right\} \quad (\text{B.30})$$

Using eqs. (B.24) - (B.30), the eqs. (B.11), (B.16), and (B.21) can be rewritten as

$$\frac{dv_r}{dt} = \dot{v}_r = \frac{q}{m} (v_\varphi B_\lambda - v_\lambda B_\varphi) + \frac{v_\lambda^2}{r} + \frac{v_\varphi^2}{r} \quad (\text{B.31})$$

$$\frac{dv_\lambda}{dt} = \dot{v}_\lambda = \frac{q}{m} (v_r B_\varphi - v_\varphi B_r) - \frac{v_\varphi^2 \tan \lambda}{r} - \frac{v_\lambda v_r}{r} \quad (\text{B.32})$$

$$\frac{dv_\varphi}{dt} = \dot{v}_\varphi = \frac{q}{m} (v_\lambda B_r - v_r B_\lambda) + \frac{v_\lambda v_\varphi \tan \lambda}{r} - \frac{v_r v_\varphi}{r}. \quad (\text{B.33})$$

The last two terms in eqs. (B.31) - (B.33) refer to the centrifugal and Coriolis forces in each direction. Eqs. (B.31) - (B.33) were used in our programs to trace the particles.

สถาบันวิทยบริการ
จุฬาลงกรณ์มหาวิทยาลัย

Appendix C

Gaussian Magnetic Flux Tube in Cartesian Geometry

For the Gaussian function in Cartesian geometry (Chuychai, 2004), we can write

$$\mathbf{A} = a(x, y)\hat{z}, \quad (\text{C.1})$$

where $a(x, y)$ is the potential function defined by

$$a(x, y) = A_0 \exp\left[-\frac{x^2 + y^2}{2\sigma^2}\right], \quad (\text{C.2})$$

or in polar coordinates, we can rewrite eq. (C.2) as

$$a(r) = A_0 \exp\left[-\frac{r^2}{2\sigma^2}\right], \quad (\text{C.3})$$

where A_0 is the central maximum value, σ determines the width of the Gaussian, and r is measured from the axis of the flux tube. Then eq. (C.1) can be rewritten as

$$\mathbf{A} = A_0 \exp\left[-\frac{r^2}{2\sigma^2}\right] \hat{z}. \quad (\text{C.4})$$

Now we find the magnetic field \mathbf{b} from $\mathbf{b}(r, \theta, z)$ in cylindrical coordinates, so the magnetic field is

$$\begin{aligned} \mathbf{b} &= \nabla \times \mathbf{A} \\ &= \left(\frac{1}{r} \frac{\partial A_z}{\partial \theta} - \frac{\partial A_\theta}{\partial z}\right) \hat{r} + \left(\frac{\partial A_r}{\partial z} - \frac{\partial A_z}{\partial r}\right) \hat{\theta} + \frac{1}{r} \left(\frac{\partial(rA_\theta)}{\partial r} - \frac{\partial A_r}{\partial \theta}\right). \end{aligned} \quad (\text{C.5})$$

In eq. (C.4), \mathbf{A} is in only the z direction. Then $A_r = A_\theta = 0$, and we get

$$b_r^{2D} = 0, \quad (\text{C.6})$$

$$b_\theta^{2D} = -\frac{\partial A_z}{\partial r} = \frac{ra(r)}{\sigma^2}, \quad (\text{C.7})$$

so

$$\mathbf{b}^{2D} = \frac{ra(r)}{\sigma^2} \hat{\theta} \quad (\text{C.8})$$

We normalize to specify b_{max}^{2D} in terms of the total turbulent magnetic field. Given

$$\begin{aligned} (b^{2D})^2 &= (b_r^{2D})^2 + (b_\theta^{2D})^2 = 0 + \frac{r^2 a^2(r)}{\sigma^4} \\ &= \left(\frac{A_0 r}{\sigma^2} \exp \left[-\frac{r^2}{2\sigma^2} \right] \right)^2, \end{aligned} \quad (\text{C.9})$$

then

$$b^{2D} = \frac{r A_0}{\sigma^2} \exp \left[-\frac{r^2}{2\sigma^2} \right]. \quad (\text{C.10})$$

Eq. (C.10) depends only on r , then we can find b_{max}^{2D} from

$$\frac{db^{2D}}{dr} = 0. \quad (\text{C.11})$$

Then we get

$$\frac{A_0}{\sigma^2} \exp \left[-\frac{r^2}{2\sigma^2} \right] - \frac{r^2 A_0}{\sigma^4} \exp \left[-\frac{r^2}{2\sigma^2} \right] = 0,$$

and

$$r_{max} = \sigma. \quad (\text{C.12})$$

From eqs. (C.7) and (C.12), we get

$$b_{max}^{2D} = \frac{A_0}{\sigma \sqrt{e}}, \quad (\text{C.13})$$

or

$$A_0 = \sigma \sqrt{e} b_{max}^{2D}. \quad (\text{C.14})$$

Then eq. (C.10) can be written as

$$b^{2D} = \frac{r b_{max}^{2D}}{\sigma} \exp \left[\frac{1}{2} - \frac{r^2}{2\sigma^2} \right]. \quad (\text{C.15})$$

The total mean field plus 2D magnetic field is

$$\mathbf{B} = B_0 \hat{z} + \mathbf{b}^{2D} = b_0 \hat{r} + \frac{ra(r)}{\sigma^2} \hat{\theta}. \quad (\text{C.16})$$

The equations of the field line in cylindrical coordinates are

$$\frac{dr}{B_r} = \frac{rd\theta}{B_\theta} = \frac{dz}{B_z}. \quad (\text{C.17})$$

Then from eq. (C.17), we get the equation of the field lines as

$$\frac{dr}{dz} = \frac{B_r}{B_z} = 0 \quad (\text{C.18})$$

$$\frac{d\theta}{dz} = \frac{B_\theta}{rB_z} = \frac{a(r)}{B_0\sigma^2}. \quad (\text{C.19})$$

If the total magnetic field has no slab field, the trajectory of the field line will be constant because the radial coordinate is constant, and the angular velocity of the field line ($K \equiv d\theta/dz$) is constant, too. Thus, given the initial point (r_0, θ_0, z_0) , the trajectory of the field line is

$$r = r_0, \quad (\text{C.20})$$

$$\theta = K(z - z_0) + \theta_0, \quad (\text{C.21})$$

where $K = a(r_0)/(B_0\sigma^2) = (b^{2D}(r_0)/B_0)/r_0$, and r is measured from the center of the Gaussian flux tube.

สถาบันวิทยบริการ
จุฬาลงกรณ์มหาวิทยาลัย

Appendix D

Pathlength of a Helical Trajectory

For a 2D Gaussian magnetic field in Cartesian geometry plus mean magnetic field (see Appendix C), we know that the trajectory of these field lines are helices. Then we can consider the pathlength along the field lines in cylindrical coordinates.

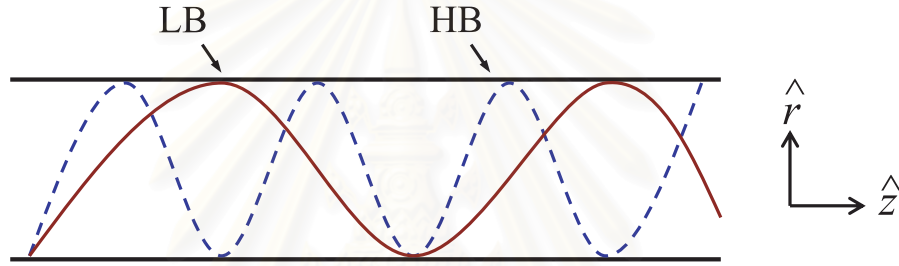


Figure D.1: Cylindrical magnetic field. LB = low B , HB = high B .

From the cylindrical coordinates, the increment in pathlength is the magnitude of

$$ds = dr\hat{r} + rd\theta\hat{\theta} + dz\hat{z}. \quad (\text{D.1})$$

The path along the field line for a half cycle for a Gaussian magnetic field plus mean field is defined by

$$r = r_0 \quad (\text{D.2})$$

$$\theta = K(z - z_0) + \theta_0, \quad (\text{D.3})$$

where $K = d\theta/dz$. We know from Appendix C that

$$K = \frac{a(r_0)}{B_0\sigma^2} = \frac{b^{2D}(r_0)}{r_0B_0}.$$

From eq. (D.1), we get

$$ds^2 = dr^2 + r^2 d\theta^2 + dz^2. \quad (\text{D.4})$$

When $dr = 0$,

$$\begin{aligned} ds^2 &= (rd\theta)^2 + dz^2 \\ ds &= \sqrt{(rd\theta)^2 + dz^2} \\ &= \sqrt{(rd\theta)^2 + \left(\frac{d\theta}{K}\right)^2} \\ &= \sqrt{r^2 + \frac{1}{K^2}} d\theta. \end{aligned}$$

Thus,

$$\begin{aligned} s &= \int_0^\pi \sqrt{\frac{r^2 K^2 + 1}{K^2}} d\theta \\ &= \pi \sqrt{\frac{r^2 K^2 + 1}{K^2}}. \end{aligned} \quad (\text{D.5})$$

At $r = r_0$,

$$\begin{aligned} s &= \pi \sqrt{\frac{r_0^2 K^2 + 1}{K^2}} \\ &= \pi \sqrt{r_0^2 + \frac{r_0^2 B_0^2}{(b_{2D}(r_0))^2}} \\ &= \pi r_0 \sqrt{\frac{b_{2D}^2 + B_0^2}{b_{2D}^2}} \\ &= \pi r_0 \sqrt{1 + \left(\frac{B_0}{b_{2D}(r_0)}\right)^2}. \end{aligned}$$

Then the half-cycle distance along the helix is

$$s = \pi \sqrt{\frac{r_0^2 K^2 + 1}{K^2}} = \pi r_0 \sqrt{1 + \left(\frac{B_0}{b_{2D}(r_0)}\right)^2}. \quad (\text{D.6})$$

Now we can find the half-cycle distance along the Gaussian 2D magnetic field + mean field for the low B case: $\sigma = 0.5l_{\parallel}$, $A_0 = 0.41218$ (for $b_{max}^{2D} =$

$A_0/(\sigma\sqrt{e}) = 0.5$, and $r_0 = 0.1l_{\parallel}$,

$$\begin{aligned} a(r_0) &= A_0 \exp\left(-\frac{r_0^2}{2\sigma^2}\right) \\ &= 0.41218 \times \exp\left(-\frac{0.1^2}{2(0.5)^2}\right) = 0.166528, \\ K_{\text{LB}} &= \frac{0.166528}{(1)(0.5)^2} = 0.6661, \\ s_{\text{LB}} &= \pi \sqrt{\frac{(0.1 \times 0.6661)^2 + 1}{(0.6661)^2}} = 4.7268. \end{aligned}$$

For medium B case: $\sigma = 0.5\lambda$, $A_0 = 0.82436$ (for $b_{\text{max}}^{2\text{D}} = 1$), and $r_0 = 0.1\lambda$,

$$\begin{aligned} a(r_0) &= 0.82436 \times \exp\left(-\frac{0.1^2}{2(0.5)^2}\right) = 0.8080, \\ K_{\text{MB}} &= \frac{0.8080}{(1)(0.5)^2} = 3.2321, \\ s_{\text{MB}} &= \pi \sqrt{\frac{(0.1 \times 3.2321)^2 + 1}{(3.2321)^2}} = 1.0215. \end{aligned}$$

For high B case: $\sigma = 0.5\lambda$, $A_0 = 1.3034$ (for $b_{\text{max}}^{2\text{D}} = 1.5811$), and $r_0 = 0.1\lambda$,

$$\begin{aligned} a(r_0) &= 1.3034 \times \exp\left(-\frac{0.1^2}{2(0.5)^2}\right) = 1.2776, \\ K_{\text{MB}} &= \frac{1.2776}{(1)(0.5)^2} = 5.1104, \\ s_{\text{MB}} &= \pi \sqrt{\frac{(0.1 \times 5.1104)^2 + 1}{(5.1104)^2}} = 0.6904. \end{aligned}$$

สถาบันวิทยบริการ
จุฬาลงกรณ์มหาวิทยาลัย

Vitae

Name: Mr. Paisan Tooprakai,

Born: April, 2nd 1974 in Lampang, Thailand.

Father: Nirat Tooprakai.

Mother: Nawarat Tooprakai.

Education:

1992-1996 Bachelor's Degree of Science (Physics),
Chiangmai University, Chiangmai, Thailand.

1996-2000 Master's Degree of Science (Physics),
Chulalongkorn University, Bangkok, Thailand.

Scholarship:

2001-2008 Received a Royal Golden Jubilee Fellowship from the Thailand Research Fund.

สถาบันวิทยบริการ
จุฬาลงกรณ์มหาวิทยาลัย